Hydrogen bond induced hetero-assembly in binary colloidal systems

Der Fakultät für Naturwissenschaften
der Universität Paderborn vorgelegte

DISSERTATION

zur Erlangung des akademischen Grades eines
Doktors der Naturwissenschaften
- Dr. rer. nat. –

von

Frank Markus Bayer, M.Sc. Chem.

(aus Berlin)

Paderborn 2011

Die vorliegende Arbeit entstand im Zeitraum Januar 2008 bis Oktober 2011 im Fachgebiet Physikalische Chemie (Arbeitskreis Prof. Dr. Klaus Huber) der Fakultät für Naturwissenschaften der Universität Paderborn.

1. Gutachter:	Prof. Dr. Klaus Huber
2. Gutachter:	Prof. Dr. Claudia Schmidt

Die Arbeit wurde eingereicht am:	16. September 2011
Tag der mündlichen Prüfung:	28. Oktober 2011

Danksagung

Mein besonderer Dank gilt Herrn Prof. Dr. Klaus Huber für die interessante Themenstellung und die vielfältige Förderung während der gesamten Promotionszeit und bereits davor. Ich bedanke mich außerdem für die hervorragenden Arbeitsbedingungen die grundlegend zu einem guten Gelingen dieser Arbeit beigetragen haben.

Bei Frau Prof. Dr. Schmidt bedanke ich mich für das bereitwillige Übernehmen des Korreferates. Desweiterem danke ich Ihr und Ihrem Mitarbeiter Mingxue Tang für die erfolgreiche Zusammenarbeit bei den Festkörper – NMR Analysen.

Der Deutschen Forschungsgemeinschaft danke ich für die Förderung durch ein Promotionsstipendium im Rahmen des Graduiertenkollegs 1464 „Mikro- und Nanostrukturen in Optoelektronik und Photonik".

Herrn Dr. Karl Hiltrop danke ich sehr für die angenehme Zeit am Rasterelektronenmikroskop. Ohne sein Interesse und das zur Verfügung stellen von Messzeit wäre diese Arbeit nur erschwert möglich gewesen. Unsere Diskussionen und Seine Gedankenanstöße fließen in diese Arbeit mit ein.

Allen Mitarbeiterinnen und Mitarbeitern der Physikalischen Chemie danke ich für das hervorragende Arbeitsklima und die angenehme Atmosphäre. Herausheben möchte ich an dieser Stelle Herrn Rolf Michels.

Besonderer, freundschaftlicher Dank gilt Herrn Dr. Sebastian Lages. Er war seit meinem Eintreten in den AK Huber stets da, um mich in die Tiefen der Streuung einzuweisen und mich, bei Verirrung, aus den „Untiefen" dieser Materie zu ziehen. Die Gespräche mit Ihm jeglicher Art sind/waren sehr wichtig.

In diesem Zusammenhang danke ich auch Herrn Stefan Birkenheuer und Herrn Dr. Alexander Lorenz. Danke für eine schöne Zeit in Paderborn!

Meiner Mutter gilt mein innigster Dank. Ohne ihre große Unterstützung während des Studiums und während der Promotion wäre dies alles nicht möglich gewesen.

Abstract

The present work pursues a new approach to the formation of binary colloidal crystals from their mixed colloid solution. Such crystals are expected to have very interesting optical. A characteristic feature of photonic crystals is a complete band gap under appropriate conditions. Light waves with energies within this distinct band gap can be completely reflected and cannot propagate in the crystal. Such a behavior is analogous to that of electrons in crystalline semiconductors solids, which have a band gap between valence and conduction band. However, photons would have great advantages over electrons in possible applications. In an appropriate medium they spread faster and undisturbed, and therefore they could transmit much more information per unit time. Early calculations showed that face-centred cubic structures of a low refractive index in a background medium with a higher refractive index, a so-called inverse face-centred cubic structure, should have a frequency gap between the bands 8 and 9 if the dielectric contrast exceeds ~ 7. At a given ratio of the refractive indices it is possible to enhance the photonic band gap by changing the arrangement of the monodisperse colloids or alternatively vary the arrangement by switching to binary systems. A realization of such binary crystals without defects is still very difficult and of great interest in research. Thus it seems to be helpful if both colloidal components are equipped with complementary capabilities to interact when combined in solution as binary colloidal mixture. Complementary functionalization means that they interact attractive exclusively with the opponent. In recent years many research groups concentrated on complementary charges as functionalization. The present work establishes a new pathway based on complementary hydrogen bonding functionalities on either colloid.

Colloids based on polystyrene were synthesized via surfactant-free emulsion polymerization and equipped with a three-dentate hydrogen bond moiety (acceptor-donor-acceptor = ADA). The polymerisation method is a good approach to quite monodisperse spherical particles. The progress of synthesis was successfully tracked by solid state NMR. Due to functionalization with 2,4-diaminotriazine residues homo-aggregation in solution was detected in the first place. Furthermore, selective coupling of the direct antagonist uracil on the colloidal surfaces was achieved. Thus, homo-aggregation among the colloids could be inhibited and at the same time the colloids proved to act as carriers for possible reagents functionalized with a complementary DAD H-bond pattern.

In order to avoid homo-aggregation from the very beginning, we developed a simplified system with single hydrogen donors and acceptors respectively on the surface of the two colloidal components. By means of surfactant free emulsion polymerisation we synthesized phenol functionalized crosslinked colloids as one component and vinyl pyridine functionalized crosslinked colloids as the second component. Similar to the previous system the colloids were analyzed by light scattering, and the aggregation kinetics was investigated with time-resolved light scattering and infrared spectroscopy. If highly concentrated solutions with added capping agents, e.g. phenol to cap the pyridine, were combined, the fast aggregation could be controlled or even inhibited. This offered a route to controlled crystallization experiments. Successively, the dependence of crystal formation and crystal structure on various parameters such as the colloid size ratio, the colloid number ratio, the overall colloid concentration and substrate properties was studied by means of scanning electron microscopy. At a colloid size ratio of 0.25 larger-scale binary colloidal crystals with up to three layers with mainly AlB_2-structure could be generated. At a colloid size ratio of 0.39 also small NaCl-like structures could be realized.

Due to exclusive hetero-aggregation the binary colloidal systems presented in this thesis give rise to hope that new and more efficient ways towards stable binary photonic crystals may be realized in the future.

Kurzfassung

Die vorliegende Arbeit behandelt und verfolgt ein neues Konzept zur direkten Bildung von binären Kolloidkristallen aus deren Lösung. Solche Kristalle können im Allgemeinen über höchst interessante optische Eigenschaften verfügen und werden oft als Analogon zu Halbleitern betrachtet. Charakteristisches Merkmal photonischer Kristalle ist, dass sie unter geeigneten Voraussetzungen eine vollständige Bandlücke besitzen. Lichtwellen mit Energien innerhalb der Bandlücke werden vollständig reflektiert bzw. können im Kristall nicht propagieren. Ein solches Verhalten entspricht dem von Elektronen in kristallinen Festkörpern, welche eine Bandlücke zwischen Valenz- und Leitungsband besitzen. Letzteres ist bekannt aus der Halbleiterelektronik. Im Hinblick auf mögliche Anwendungen besitzen Photonen jedoch große Vorteile gegenüber Elektronen, da sie sich in geeigneten Medien schneller und ungestörter ausbreiten und daher wesentlich mehr Information pro Zeiteinheit übertragen können. Schon allein aus diesem Grund besteht ein großes industrielles Interesse an photonischen Kristallen. Beim Übergang von einfachen photonischen Kolloidkristallen, aus einer Sorte monodisperser Kolloide, zu binären Kristallen, aus einem Gemisch aus zwei unterschiedlich großen Kolloiden, vergrößert sich eben diese Bandlücke nochmals. Theoretische Kalkulationen solcher Bandlücken ergaben eine Verdopplung des Frequenzbereichs beim Übergang vom einfachen hexagonalen kubisch flächenzentrierten Modell zum binären NaCl analogen Kristall. Solche binären Kristalle direkt und selektiv ohne Defekte zu generieren ist nach wie vor sehr schwierig und vom großen Interesse für die Forschung. Genau hier setzt diese Arbeit an. So scheint es hilfreich zu sein wenn beide Komponenten in einem binären Kolloidgemisch in Lösung mit komplementären Funktionalitäten ausgestattet sind. Komplementär heißt, dass diese ausschließlich attraktiv mit der jeweils anderen Kolloidsorte wechselwirken können. In den letzten Jahren wurde hier verstärkt auf komplementäre Ladungen gesetzt. Über komplementäre Wasserstoffbrückenbindungsfunktionalitäten auf den eingesetzten Kolloiden soll diese Arbeit einen neuen Weg aufzeigen.

In Anlehnung an biologische Systeme wurden Kolloide auf Basis von Polystyrol mittels Emulgator freien Emulsionspolymerisation synthetisiert und anschließend mit drei-zahnigen Wasserstoffbrückenbildner (Akzeptor-Donor-Akzeptor) ausgestattet. Der Synthesefortgang wurde erfolgreich mittels Festkörper-NMR begleitet. Auf Grund dieser 2,4-diaminotriazine Funktionalitäten konnte eine Kolloidaggregation nachgewiesen werden. Ebenfalls eine selektive Kopplung eines direkten Antagonisten, Uracil, an den Kolloiden wurde erreicht und somit die Homo-Aggregation, also das attraktive Wechselwirken unter den Kolloiden, inhibiert. Aber eben diese Homo-Aggregation stellt einen großen Nachteil für dieses System dar. Eine kontrollierte Aggregation, mit einem komplementär funktionalisierten Kolloid, zu einem binären Kristall scheint diese Homo-Aggregation nur erschwert möglich zu machen.

Anschließend folgte der Wechsel zu einem einfacheren System, mit einem Wasserstoffbrücken-Donor auf einer Sorte von Kolloiden und einem komplementären Wasserstoffbrücken-Akzeptor auf der anderen Sorte von Kolloiden. Eine Funktionalisierung mit Phenol auf der einen Seite und 4-Vinylpyridin auf der anderen brachte einen entscheidenden Vorteil: Exklusive Hetero-Aggregation. Wie bei dem anderen System wurden die Kolloide mit Lichtstreuung analysiert sowie die Aggregationskinetik mit zeitaufgelöster Lichtstreuung und infrarot Spektroskopie untersucht. Des Weiteren konnten durch Abschwächung der attraktiven Wechselwirkungen durch gezieltes Blocken von Funktionalitäten kontrollierte Kristallisationsexperimente durchgeführt werden. Die Abhängigkeit der Kristallbildung und -struktur von verschiedenen Parametern wie Kolloid-Größenverhältnis, Kolloid-Zahlenverhältnis aber auch Gesamtkonzentration und Substratbeschaffenheit, wurden mit rasterelektronenmikroskopischen Aufnahmen untersucht. Es konnten somit größer flächige binäre Kolloidkristalle mit bis zu drei Lagen generiert werden. Dabei trat hauptsächlich die hexagonale AlB_2- neben der NaCl-Kristallmodifikation auf.

Das hier Vorgestellte binäre Kolloidsystem gibt auf Grund der exklusiven Hetero-Aggregation Hoffnung zu neuen und effizienteren Wegen stabile binäre photonische Kristalle zu realisieren.

Why cannot we write the entire 24 volumes of the Encyclopaedia Britannica on the head of a pin?
Let's see what would be involved. The head of a pin is a sixteenth of an inch across. If you magnify it by 25000 diameters, the area of the head of the pin is then equal to the area of all the pages of the Encyclopaedia Britannica. Therefore, all it is necessary to do is to reduce in size all the writing in the Encyclopaedia by 25 000 times. Is that possible? The resolving power of the eye is about 1/120 of an inch—that is roughly the diameter of one of the little Encyclopaedia. This, when you demagnify it by 25 000 times, is still 80 angstroms in diameter—32 atoms across, in an ordinary metal. In other words, one of those dots still would contain in its area 1000 atoms. So, each dot can easily be adjusted in size as required by the photoengraving, and there is no question that there is enough room on the head of a pin to put all of the Encyclopaedia Britannica.

…

As we go down in size, there are a number of interesting problems that arise. All things do not simply scale down in proportion. There is the problem that materials stick together by the molecular (Van der Waals) attractions. It would be like this: After you have made a part and you unscrew the nut from a bolt, it isn't going to fall down because the gravity isn't appreciable; it would even be hard to get it off the bolt. It would be like those old movies of a man with his hands full of molasses, trying to get rid of a glass of water. There will be several problems of this nature that we will have to be ready to design for.

…

What could we do with layered structures with just the right layers? What would the properties of materials be if we could really arrange the atoms the way we want them? They would be very interesting to investigate theoretically.

I can't see exactly what would happen, but I can hardly doubt that when we have some *control* of the arrangement of things on a small scale we will get an enormously greater range of possible properties that substances can have, and of different things that we can do.

“*There's Plenty of Room at the Bottom*”
Feynman, R. *Journal of Microelectromechanical Systems* Vol. 1, No. 1. pp. 60-66 (1992)

Contents

1. Introduction

1.1 Nature's paint box

Nowadays inks for painting always contain organic dyes or inorganic pigments, which have characteristic absorption bands. In nature, not all of the colors originate from the absorption of light by a dye or pigment. [1-3] In some cases, nature has shown that she can build periodic structures established by the periodicity of the refractive index. When such periodicity is of the order of a few tens of nanometers or a few hundred nanometers the structure will interfere with electromagnetic waves in a characteristic way. It can modify, reflect, transmit, or even absorbed light. Often, one gets then so called bio-optical diffraction gratings. [4,5]

One dimensional multilayers are common in insects and also in certain types of leaves or minerals. Nacre of abalone mussels is one of the prominent examples.[6] Multilayers constitute interference mirrors or filters, creating the characteristic colors of reflected light. The periodicity is produced by alternating layers with different refractive indices, generally a high reflective index layer (e.g. chitin) and air or a physiological liquid as low reflective index material. When several reflecting filters are brought together, either in an ordered or a disordered way, they can produce a broad band reflector and generate a silver or gold luster, observed in certain beetles or fishes. In butterflies of the morpho species (Figure 1.1) the layers are arranged in the form of columns. [7]

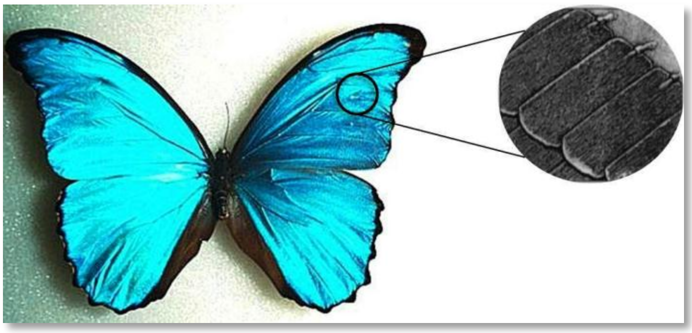

Figure 1.1: The butterfly *morpho didius* is a representative example of a diffracting biological microstructure. The SEM magnification shows the grating which results in the blue color. [5,7]

Two dimensional periodic structures are less common in biology than one-dimensional structures. They generally exist as ordered cylindrical nano-objects of chitin in low-index materials. Cat's eyes, some bird's feathers and certain butterfly wings have structures of that type.

However, it is the three dimensional (3D) periodic structure that exhibits an analogy to crystals made up of atoms or molecules. It has long been known that opal is a colloidal crystal, formed by closely packing colloidal beads of silica (Figure 1.2). Like the 2D structures, the 3D periodic structures also exist in negative form, with cavities in a solid matrix. They are then called inverse opa1s.

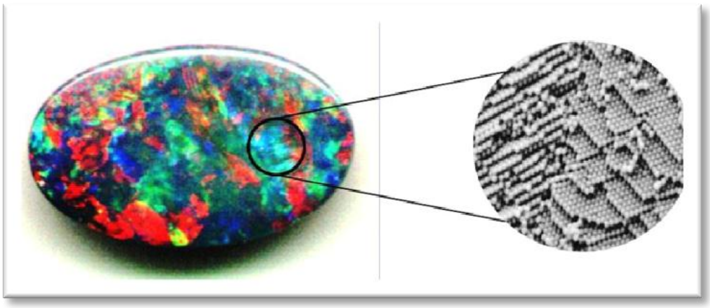

Figure 1.2: Natural opal and a SEM image showing its microstructure made of close-packed silica spheres.

The previously shown opal structures from nature for 3D optical diffraction gratings are based on dielectric lattices that are geometrically complementary. They exhibit a structure with periodically changing refractive index in all three dimensions and thus those structures for example reflect light in every three dimensions. This brings us to the question if we can copy those structures synthetically and what might they be good for?

1.2 Photonic crystals

The fascination for geological and biological diffraction lattices found a new height with the theoretical discovery of Yablonovitch [8] and John [9] in 1987. The use of high refractive index contrast and periodicity at the scale of light waves creates a remarkable class of materials, so called photonic crystals. When made with the proper constituents and designed in the adequate structure they can be considered to be the optical analogue of semiconductors [10,11], generating a band gap for photons. This qualifies them to be used as active materials in optical transistors, diodes, and other devices [l2,13]. A schematic drawing of one-, two- and three-dimensional gratings are given in Figure 1.3. To fabricate photonic crystals, top-down approaches and bottom-up self-assembly strategies can be used. See also chapter 1.4.

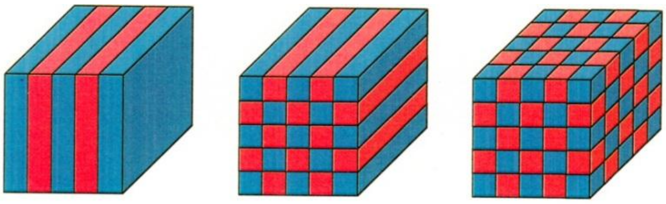

Figure 1.3: Scheme of one, two and three dimensional gratings.

The solution of Maxwell’s equations for the propagation of light in a dielectric lattice is showing discontinuities in the frequency $\omega(k)$ versus the wave vector k due to optical Bragg diffraction. Hence, the movement for a photon observed in vacuum breaks down in a crystal lattice. Those discontinuities are called stop bands and correspond to standing waves, which is the condition for Bragg diffraction of waves. The photonic band gap (PBG) is a frequency range ω(k) in wave vector space k, where the propagation of light is forbidden in all directions in the photonic crystal (Figure 1.4). In this frequency range, light shining on the photonic crystal is completely reflected and light within the crystal would be completely trapped.

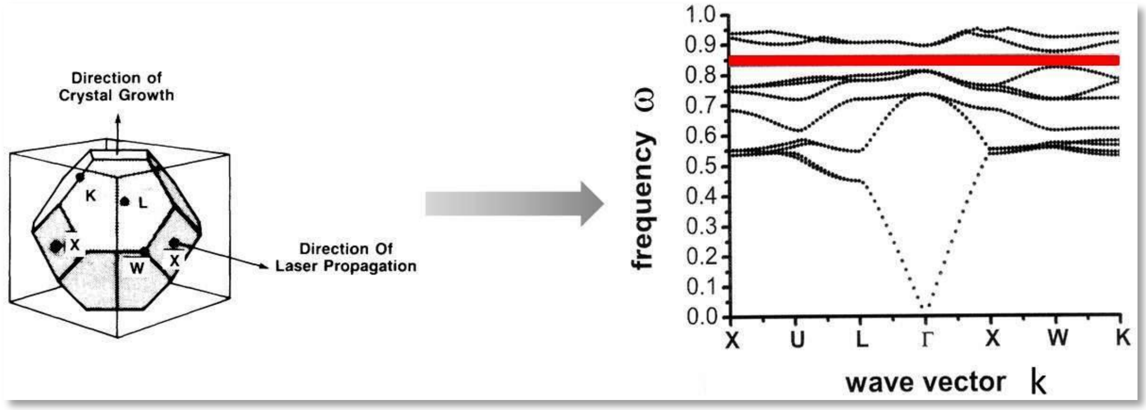

Figure 1.4: Brillouin zone for a simple face centered cubic (fcc) lattice in the reciprocal space with the direction of crystal growth and laser propagation. [8] Right picture shows the calculated band structure for an inverse air in silicon fcc lattice. [47] Because the reflective index difference is high enough there is a complete stopband resulting (red)

One of the first proposals for the fabrication of photonic crystals was provided by Yablonovite [16] and is presented in Figure 1.5. He could show that drilling cylindrical holes along specific directions in a block of solid material would create a connected network with a symmetry that resembles that of diamond [17,18].

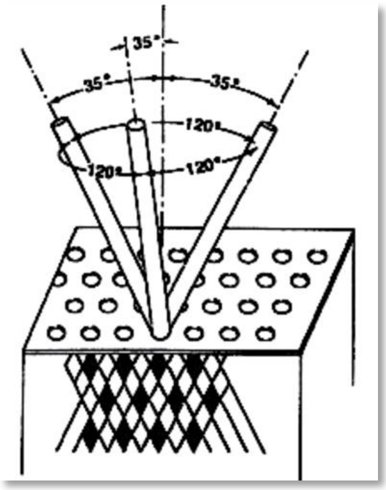

Figure 1.5: Fabrication of the Yablonovite-structure – the first photonic crystal structure with a complete photonic band gad (PBG). [16]

1.3 Optical properties of colloidal crystals

Most colloidal crystals are built with the {111} lattice planes parallel to the substrate surface. An example is shown in Figure 1.6. As a first approximation the first stop band can be described by the combination of Bragg's law:

$$\lambda = 2n_{eff}d_{(hkl)}\cos\theta_2 \qquad (1.1)$$

with Snell's law:

$$n_1\sin\theta_1 = n_2\sin\theta_2 \qquad (1.2)$$

to give the master equation for the wavelength of the first stop band:

$$\lambda_{(hkl)} = 2d_{(hkl)}\sqrt{\langle\varepsilon\rangle - sin^2\theta_2} \qquad (1.3)$$

where the effective dielectric constant $\langle\varepsilon\rangle$ of the colloidal crystal is calculated according to:

$$\langle\varepsilon\rangle = \sum_i f_i \varepsilon_i \tag{1.4}$$

In eq (1.4) the sum includes the weighted average volume fraction f_i of the host medium air and the spheres which are 26% and 74%, respectively, for a face centered cubic colloidal crystal (fcc). ε_i is the dielectric constant of the spheres and the host medium respectively. The dielectric constant corresponds to the refractive index squared.

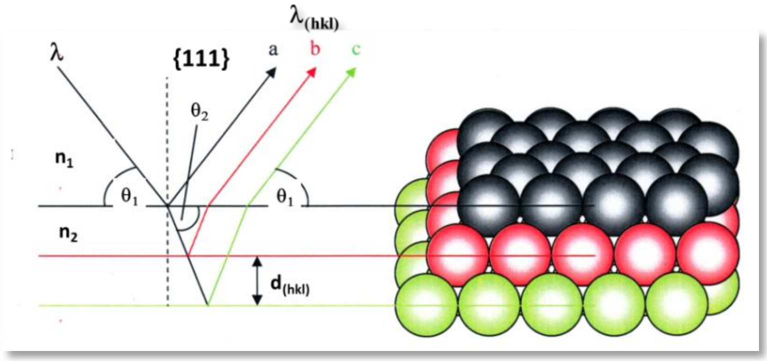

Figure 1.6: The diffraction of light from fcc close-packed { 111 } crystal planes in a colloidal photonic crystal.

The optical spectra respond to changes in microsphere diameter, refractive index, crystal orientation, and inversion of the structure to the so-called inverse colloidal crystal, according to what predicted by the Bragg-Snell equation.

Early calculations showed that face-centred cubic structures of a low refractive index (RI) in a background medium with a higher RI, a so-called inverse *fcc* structure, should have a gap between the bands 8 and 9 (Figure 1.7) if the dielectric contrast exceeds ~ 7.

At a given ratio of the RIs it is possible to enhance the PBG by changing the arrangement of the monodisperse colloids or alternatively by switching to binary systems. A simple binary crystal is a NaCl-like lattice. If interstitial lattice sites can be filled with silicon successively and the colloids can be removed, the resulting inverse air in silicon structure is expected to show a nearly doubled PBG compared to an *fcc* structure. [19] This would be a beneficial feature for modern telecommunication technics; since a broader frequency band of light could be guided/submitted and would make such crystal formation even more interesting for research and industry. General possibilities to guide light in crystals are given in the following.

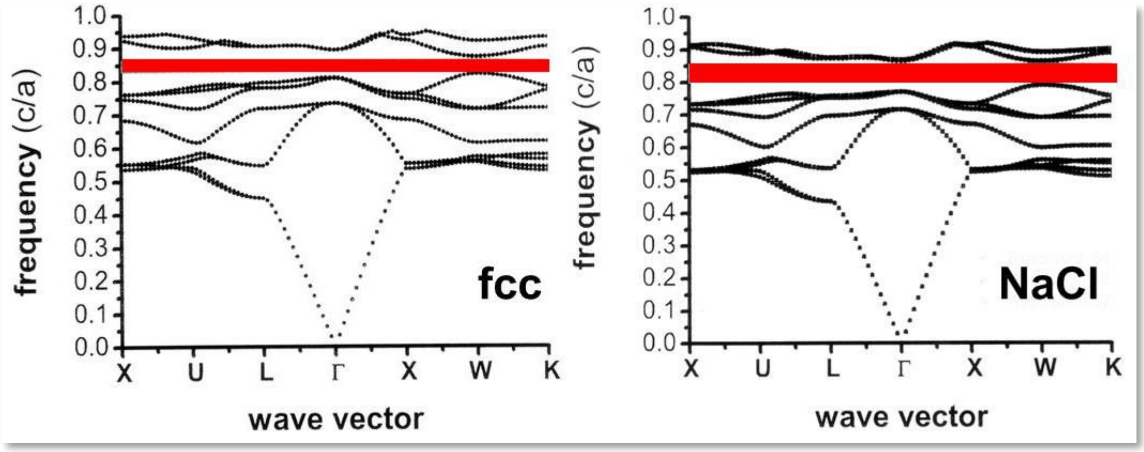

Figure 1.7: Right: Calculated band structure for an inverse air in silicon fcc lattice. Left: The resulting band gap can become nearly twice as broad by "simply" switching to a NaCl lattice in otherwise identical conditions. Stop bands are indicated as red bars. [19]

It is rather the imperfection of solid-state materials than their perfection, which offers interesting properties with respect to their function and efficiency. This is also true for photonic crystals. Theories show that by introducing line and/or bend defects (Figure 1.8) into a perfect photonic crystal, electromagnetic modes with the wavelength in the range of a certain PBG, can be localized. That means that light could be channeled and guided along tiny waveguides nearly without any energy losses. Micro-optical components made from photonic crystals on chips could form the basis of all-optical devices and circuits for next generation optical telecommunication technologies.

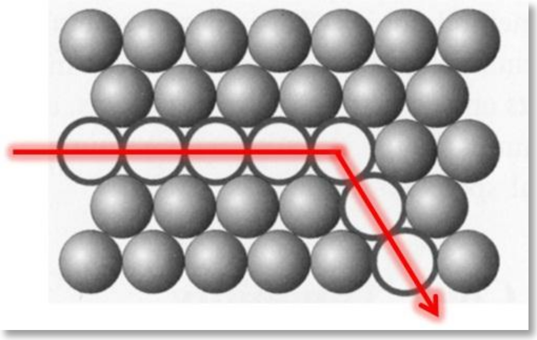

Figure 1.8: Red light beam guided in a photonic crystal line defect.

For example Joannopoulos' "Photonic Micropolis" [20] from 1997 is believed to represent the all-optical chip of the future (Figure 1.9).

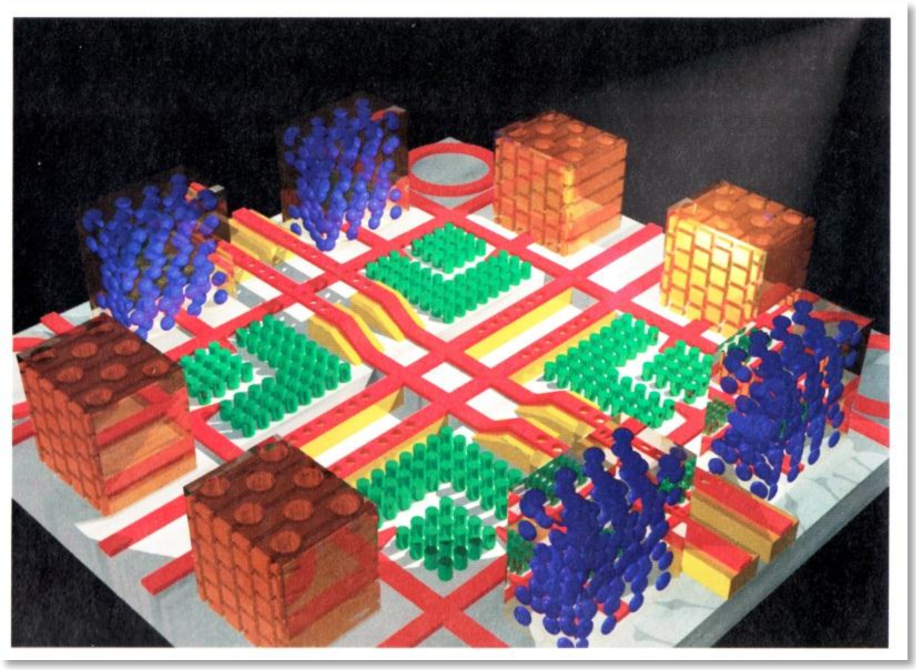

Figure 1.9: „Photonic Micropolis" from Joannopoulos [20]. In addition to colloidal crystals (blue) there are two-dimensional photonic crystals (green) and photonic wires (red) arranged to symbolize an all-over photonic chip.

This idea is inspiring material scientists to dream about the scientific and technological benefits from computing with light and chips constructed from new miniaturized optical components. The all-optical chip comprises integrated microphotonic crystals with lD, 2D, or 3D periodicity. Coupling of light from a waveguide to a photonic crystal may be accomplished with defects built into the photonic lattice. Though first photonic crystals have been prepared, the science and application of photonic crystals are still in their earliest stages of development, and there are many essential questions that still need to be addressed.

1.4 Fabrication of nano-structures: top-down versus bottom-up

Obviously there are two approaches to the preparation of nanomaterials and the fabrication of nanostructures: top-down and bottom-up. Both approaches play an important role in modern nanotechnology. Abrasion and milling are typical top-down methods in making nanoparticles, whereas colloidal dispersions are a good example for a bottom-up approach to the synthesis of nanoparticles. Lithography may be considered as a hybrid approach, since the growth of thin films is bottom-up whereas etching is top-down, while nanolithography and nanomanipulation are commonly a bottom-up approach. There are advantages and disadvantages in both approaches.

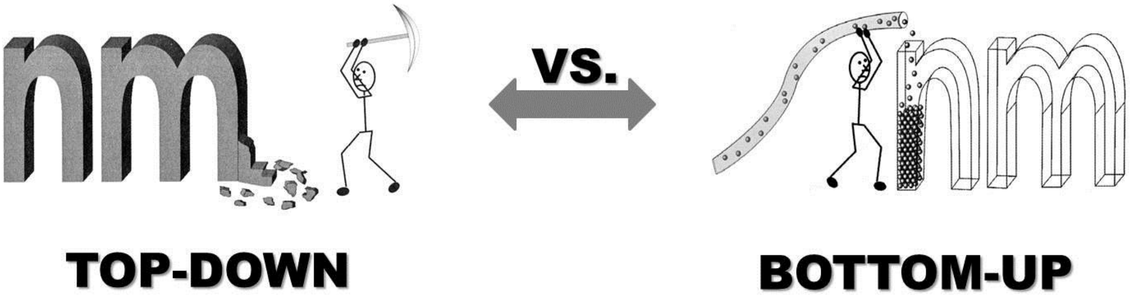

Figure 1.10: Scheme “*top-down versus bottom-up approach* “. Comics from [21].

Among others, the biggest problem with top-down approaches is the imperfection of the surface structure. It is well known that the conventional top-down techniques such as lithography can cause significant crystallographic damage to the processed patterns [22] and additional defects may be introduced even during the etching steps. [23] Such imperfections would have a significant impact on physical properties and surface chemistry of nanostructures and nanomaterials, since the surface over volume ratio in nanostructures and nanomaterials is very large. Regardless of the surface imperfections and other defects that top-down approaches may introduce, they keep on playing an important part in the synthesis and fabrication of nanostructures and nanomaterial’s.

The silicon woodpile was the first 3D photonic crystal made by lithographic micro fabrication techniques with a complete PBG.[24] It consists of a stacking of layers of silicon rods in which adjacent layers are arranged perpendicularly. The silicon woodpile (Figure 1.11) is made by a complex layer-by-layer procedure that involves lithographic patterning of silicon, infilling the surface relief pattern with a deposited layer of silica, planar machining of the patterned silica-silicon composite layer, and deposition of the next silicon layer. These steps are repeated to give the desired number of layers and selective etching of silica provides the desired silicon woodpile photonic crystal.

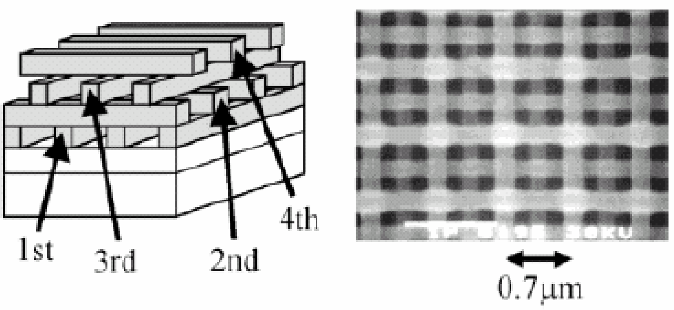

Figure 1.11: Scheme of the silicon-woodpile structure with four levels (left) and a TEM image (right). [24]

Like the name suggests, the bottom-up approach refers to the build-up of a material from the bottom: atom-by-atom, molecule-by-molecule, or colloid-by-colloid. In organic chemistry and/or polymer science, polymers are synthesized by connecting individual monomers. The bottom-up approach is often highlighted in nanotechnology literature, albeit it is not new in materials synthesis. In crystal growth, species, such as atoms, molecules or colloids assemble into crystal structure after encountering the growing surface one by one. A typical material synthesis is to build a large scale materials atom by atom or molecule by molecule. Examples include the growth of single crystals and deposition of films in electronic industry. Due to kinetic reasons, different synthesis and processing approaches often result in significant differences in chemical composition, crystallinity, and microstructure of the material. As a consequence the material shows different physical properties.

The bottom-up approach also plays an important role in the fabrication and processing of nanostructures and nanomaterials. There are several reasons for this. When structures fall into a nanometer scale, there is not much choice for a top-down approach. The tools are still too large to create such small objects.

The bottom-up approach also promises a better chance to obtain nanostructures with less defects, more homogeneous chemical composition, and better short and long range ordering in crystals. This is because the bottom-up approach is driven mainly by the reduction of Gibbs free energy, so that nanostructures and nanomaterials are closer to their thermodynamic equilibrium state. Contrary to this, top-down approaches most likely introduce more internal stress than bottom-up methods, in addition to surface defects and contaminations.

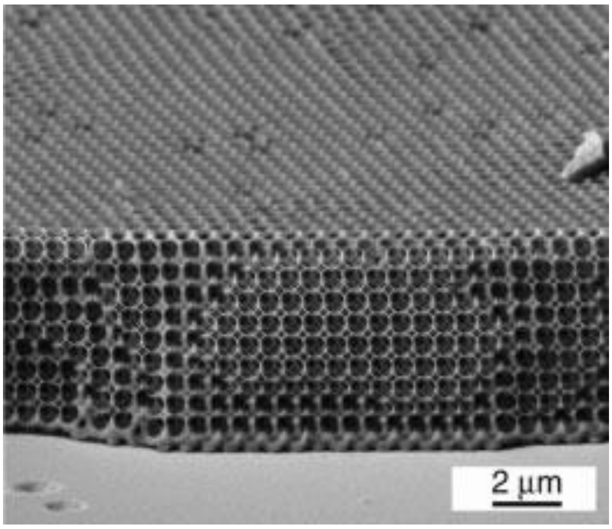

Figure 1.12: The first silicon inverse colloidal crystal confirmed theoretical predictions of a full PBG in these materials. [25]

The silicon inverse opal (Figure 1.12) was the first 3D silicon photonic crystal made by bottom-up self-assembly with a complete PBG.[25] It presents a face centered cubic photonic lattice of interconnected air spheres in a silicon matrix. The silicon inverse opal is made by the CVD of silicon by thermal decomposition of disilane within the interstitial voids of a silica colloidal crystal template. The silica is then selectively etched from the composite silicon-silica colloidal crystal to create the desired inverse silicon opal.

The driving forces for molecule and material organization are quite varied and can be ionic, covalent, non-covalent, metal-ligand and hydrogen bonding interactions, which may result in structures and properties not found in the individual components.

Self-assembly by spontaneously organizing building blocks with sizes that are beyond the sub-nanometer scale of most molecules, macromolecules or colloids is based on several important principles that need to be taken into account. For example there is the scale, shape and surface structure of the distinct building blocks, the attractive and repulsive interactions between the building blocks, the reversible association-dissociation and/or adaptable motion of building blocks during the assembly towards the lowest energy structure, the building block interactions with solvents, interfaces, templates and the dynamics at building-blocks like its mass-transport or agitation.

A challenge towards perfect structures brought along by self-assembly is to find ways of synthesizing (bottom-up) or fabricating (top-down) building blocks not only with the proper chemical composition but also having a uniform size and shape. However, no matter which way building blocks are made they are never completely monodisperse. There always exists a degree of polydispersity in their size and shape. Similarly challenging is the preparation of building blocks with a particular surface structure, charge and functionality. Surface properties can control the interactions between the building blocks as well as with their environment. This can determine the geometry and the distances at which building blocks come to equilibrium in a self-assembled system. Relative motion between building blocks causes collisions between them. Energetically allowed aggregation-disaggregation processes and movements within the self-assembled structure are mandatory in order to reach the most stable form. If the building blocks are not too strongly bound in the assembly it will be possible to adjust an ordered structure. If on the other hand the building blocks in the assembly are too strongly interacting, they will be unable to adjust their relative positions within the assembly and a less ordered structure will result.

Building blocks can be made out of most known organic, inorganic, hybrid and polymeric materials. [26-28] In the following we will concentrate on polymeric microspheres and their assembly into colloidal crystals.

1.5 Colloidal interactions

Microspheres interact via attracting van der Waals forces in the first place. These colloidal interactions are open to a wide range of modifications because of the possibility to control the surface properties of the microspheres by tuning surface charge and surface functional groups. [29-31] To understand the process of microsphere self-assembly it is useful to take a look on the basics of the colloidal interactions responsible for crystallization.

1.5.1 Van der Waals attraction potential

When colloids are small (micrometers or less) and dispersed in a solvent, van der Waals attraction forces and Brownian motion play important roles, whereas the influence of gravity becomes negligible. The van der Waals force is a weak force and becomes significant only at a short distance. Brownian motion ensures that the nanoparticles are persistently colliding with each other. The combination of van der Waals attraction forces and Brownian motion would result in the formation of agglomeration of the nanoparticles. Van der Waals interactions between two colloids are the sum of the molecular interactions for all pairs of molecules incorporated in the respective particle, including the molecules in the surrounding medium such as the solvent.

Integration of all the van der Waals interactions over two spherical particles of radius *r*, separated by a distance, *S* (Figure 1.13) gives the total interaction energy or attraction potential [32]:

$$\phi_A = -\frac{A}{6}\left\{\frac{2r^2}{S^2+4rS} + \frac{2r^2}{S^2+4rS+4r^2} + ln\left(\frac{S^2+4rS}{S^2+4rS+4r^2}\right)\right\} \qquad (1.5)$$

where the negative sign represents the attractive nature of the interaction between two particles. In eq (1.5) A is a positive constant termed the Hamaker constant, which has a magnitude on the order of 10^{-19} J to 10^{-20} J [33], and depends on the polarization properties of the molecules in the two colloids and in the medium which separates them.

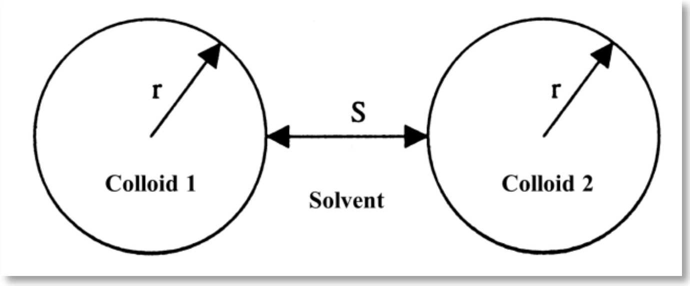

Figure 1.13: Pair of particles exerted to van der Waals interactions.

The Equation (1.5) can be simplified under various boundary conditions. For example, when the separation distance between two similar spherical particles is significantly smaller than the particle radius, e.g. *S / r << 1*, the simplest expression of the van der Waals attraction could be obtained. For colloids with equal radii it is:

$$\phi_A = \frac{-A\,r}{12\,S} \tag{1.6}$$

For binary colloidal systems the expression of the van der Waals forces between colloids with unequal radii is given as:

$$\phi_A = \frac{-A\,r_1 r_2}{6\,S\,(r_1+r_2)} \tag{1.7}$$

1.5.2 Interactions between two spherical particles: DLVO theory

Colloidal interactions between charged microspheres result from a hierarchy of different types of interaction. The total interaction between two particles, which are electrostatically stabilized, is the combination of van der Waals attraction and electrostatic repulsion.

The electrostatic stabilization of particles in a suspension is successfully described by the DLVO theory, named after Derjaguin, Landau, Verwey and Overbeek. [34] There are some important assumptions in the DLVO theory:

- Infinite flat solid surface
- Uniform surface charge density
- Constant surface electric potential due to invariable concentration profile
- Solvent exerts influences via dielectric constant only, e.g. no chemical reactions between the particles and solvent.

It becomes clear that some of the assumptions are far from being real. For example, the surface of particles is not infinitely flat, and the surface charge density will most likely change when two charged particles get very close to each other, since polarization forces will arise. However, the introduced simplifications compensate each other and the DLVO theory works very well in explaining the interactions between two approaching particles, which are electrically charged.

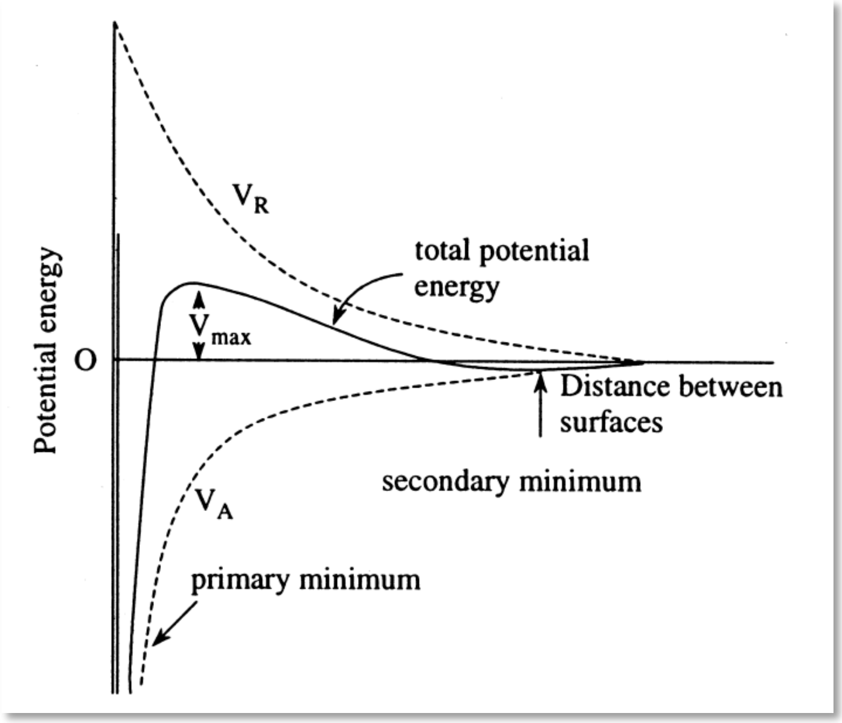

Figure 1.14: Scheme of the DLVO potential presented by the straight line. Dashed lines: attractive van der Waals potential V_A, repulsive electrostatic potential V_R. [34]

Figure 1.14 shows the van der Waals attraction potential, the electric repulsion potential, and the combination of the two potentials as a function of distance from the surface of a spherical particle. [34] At a distance far from the solid surface, both van der Waals attraction potential and electrostatic repulsion potential reduce to zero. Near the surface is a deep minimum in the potential energy produced by the van der Waals attraction. An intermediate maximum occurs once the electric repulsion potential dominates the van der Waals attraction potential. The maximum is also known as repulsive barrier. If the barrier is greater than ~10 kT, where k is the Boltzmann constant and T the temperature, the collisions of two particles produced by Brownian motion will not overcome the barrier and agglomeration will not occur. Since the electric potential depends on the concentration and valence state of counter ions while the van der Waals attraction potential is almost insensitive to these two parameters, the overall potential is strongly influenced by the concentration and valence state of the counter ions. An increase in concentration and valence state of counter ions results in a faster decay of the electric potential. [34] As a result, the repulsive barrier is reduced and its position is pushed towards the particle surface. A secondary minimum does exist if the concentration of counter ions is high enough. If a secondary minimum is established particles are likely to be associated with each other, which is known as flocculation.

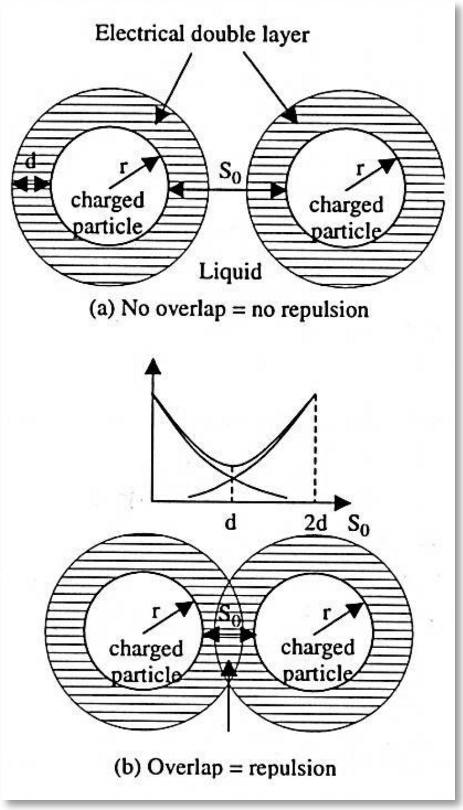

Figure 1.15: Schematic illustration of the conditions for the occurrence of electrostatic repulsion between two particles. [34]

If particles of one sign are part of one phase then the resulting electric field will attract ions of the opposite sign which will accumulate as another neighbouring layer. This second layer will still exhibit Brownian movement. The static charges on the particle and the attracted ion layer form the liquid phase constitute the electric double layer. In general the total charge of the double layer is zero. So, if two particles are far apart, i. e. the distance between the surfaces of two particles is larger than the combined thickness of two electrical double layers of two particles; no interaction between two particles does occur anymore (Figure 1.15(a)). However, when two particles move closer and the two electrical double layers overlap, a repulsion force is developed. As the distance reduces, the repulsion increases and reaches the maximum once the distance between two particle surfaces equals the distance between the repulsive barrier and the surface (Figure 1.15(b)). Such a repulsion force can be understood in two ways. One way is that the repulsion derives from the overlap of electric potentials of two particles. It should be noted that the repulsion is not directly due to the surface charge on solid particles but due to the interaction between the two double layers. The other way is the osmotic flow. When two particles approach one another, the concentration of ions between two particles where two double layers overlap, increases significantly, since each double layer would retain its original concentration profile. As a result, the original equilibrium concentration profiles of counter ions and surface charge determining ions are disturbed. In an attempt to restore the original equilibrium concentration profiles, more solvent had to flow into the region where the two double layers overlap. Such an osmotic flow of solvent effectively holds two particles apart. The osmotic force disappears only when the distance between the two particles increases beyond the sum of the thickness of their two double layers.

Although many important assumptions of the DLVO theory are not satisfied in real colloidal systems, where small particles are dispersed in a diffusive medium, the DLVO theory is still valid when the following conditions are met:

- Dispersion is very dilute, where the charge density and distribution on each particle surface and the electric potential in the proximity next to each particle surface are not interfered by other particles.
- No other force is present besides the van der Waals force and the electrostatic force, e. g. the gravity is negligible or the particle is small.
- Geometry of particles is relatively simple with homogeneous surface properties all over the entire particle surface, and thus with uniform surface charge density as well as with uniform electric potential in the surroundings.
- The double layer is purely diffusive, so that the distributions of counter ions and charge determining ions are determined by all three forces: electrostatic force, entropic force and hydrodynamics of Brownian motion.

1.5.3 Depletion forces

Depletion forces are the result of an osmotic pressure exerted by smaller particles in the presence of larger particles in a binary suspension. The smaller particles move more quickly under the thermal fluctuations in the system. These particles impinge on the larger particles from all sides. When larger particles get close enough and are separated by less than the radius of the small colloid, the small particles can no longer fit into the space between the facing surfaces of the larger colloids, but continue impinging the external surfaces. In effect, this results in an osmotic pressure pushing the two large colloids together. These entropic forces can lead to an interesting phase behavior including phase separation (Figure. 1.16). [35-39]

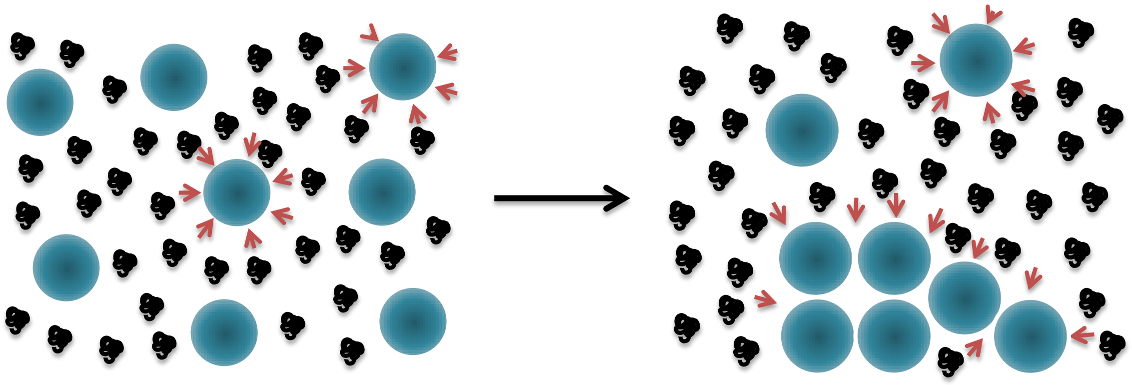

Figure 1.16: Schematic drawing of the entropically driven depletion effect in a mixture of polymer coils and hard sphere colloids. During solvent evaporation phase separation occurs. The polymer coils are smaller than the colloids.

Generally, the range of these depletion interactions corresponds to the size of the smaller particles and is shorter than electrostatic interactions in a colloidal suspension. However, depending on the concentration of the smaller particles they can be significant in a hard sphere colloidal system. Furthermore, these forces exist across a broad range of particle sizes, even beyond of what is typically considered a colloidal particle.

A nice example of a “real” depletion is shown in Chapter 3.4, Figure 3.16. There, a reference system of colloids, prepared from two fractions with different particle size but from the same material and functionalization (colloids 4OH-1 and 4OH-4), does not show any specific attractive interaction. Yet, this mixture shows strong depletion behavior during slow solvent evaporation.

1.6 Colloidal self-assembly in crystals and films

The atom-colloid analogy is an interesting key issue in colloidal systems. It basically means that colloidal systems exhibit analogous phase behavior as atoms and molecules.

For example, a dispersion of colloids with a hard-sphere interaction potential combined with a short range attractive potential, which means that colloids primarily interact when they physically collide, can form a liquid phase, a crystalline phase and even a glassy phase [40]. In other words, colloidal dispersions are a model system for atomic and molecular processes [41], including melting and crystallization.

The driving force behind crystallization of hard-sphere colloids is maximization of entropy. A system reaches thermodynamic equilibrium when it minimizes its free energy F [42].

$$F = U - T\,S \tag{1.8}$$

Here, U is the total (interaction) energy of the system, T is its temperature and S is the entropy of the system. In the case of simple hard spheres, the energy U does not influence minimization of the free energy F because the interaction energy of two spheres is either 0 (no overlap) or infinitely large (overlap). Thus, the hard-sphere interaction only reduces the volume that is available to the colloids. Entropy is a measure of the number of possible microscopic configurations, the system accepts at a given temperature and pressure. A single configuration is a set of values for all particle coordinates and momenta. The larger the volume available to a system gets, the more configurations can be realized by this system. Hence, entropy depends on the volume that is available to the system. Colloids in a crystal are trapped in the unit cells surrounding their lattice position.

Equilibrium configurations of colloidal assemblies are randomly close-packed, although slow sedimentation favors fcc packings (Figure 1.17) over hcp structures. Nonequilibrium hydrodynamic interactions on settling and colloidal particle interactions might favor the formation of fcc packings. Most experimental applications of colloidal crystals are based on colloidal assembly on substrates requiring a relatively short period of time. Various processes, including sedimentation, vertical dip-coating deposition, infiltration in the capillary, epitaxial growth on a patterned substrate, and spin-coating have been developed. [43-46]

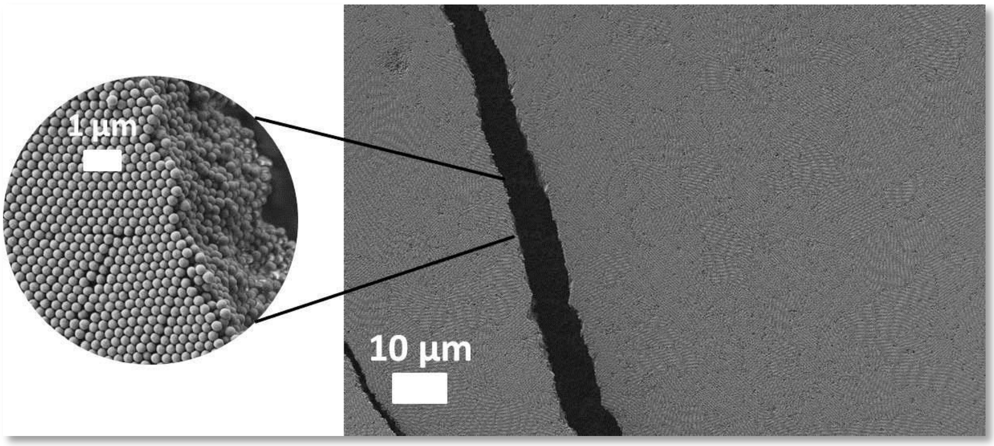

Figure 1.17: Large fcc colloidal crystal of monodisperse spherical particles (4OH-4) with a radius of 260nm. The fcc crystal shows different orientations of crystallites induced by some defects. The crystal was prepared by slow evaporation of the solvent from 70 wt% Toluene : 30 wt% $CHCl_3$ at 40°C and reduced pressure (500mbar).

One of the most frequently used ways to make colloidal crystal films is the evaporation driven self-assembly, shown in Figure 1.18, in which a substrate is placed tilted in a dispersion of colloids in a solvent.

As the solvent evaporates the colloids are guided by convective forces to the meniscus, where they are forced by capillary forces to self-assemble into a colloidal crystal film, with a layer thickness determined by the microsphere diameter, the volume fraction, and the wetting properties of the solvent on the respective substrate. To grow films of colloidal spheres with diameters larger than about 450 nm, an accelerated evaporation must be employed to oppose rapid sedimentation. Both heat [47,48] and vacuum [49] can be used for this purpose.

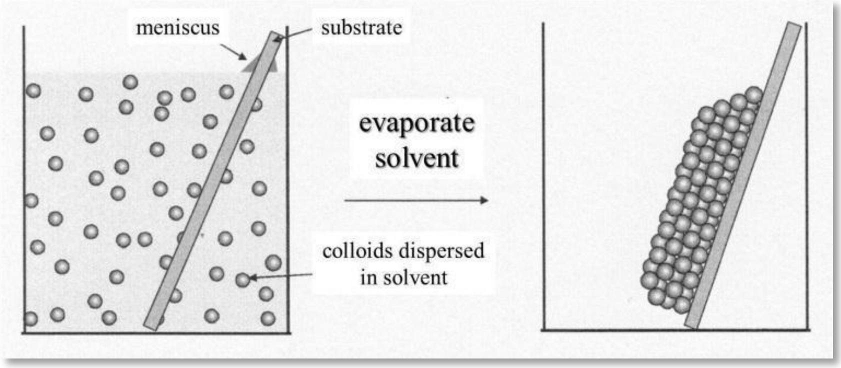

Figure 1.18: Preparation of well-ordered colloidal films by slow evaporation of the solvent under increased temperature and reduced ambient pressure. [43]

1.7 Binary super lattices

As discussed in Chapter 1.6 colloids with narrow size distribution can self-assemble into long range ordered lattices upon slow evaporation of the solvent. The lateral size of long-range ordered domains can approach hundreds of micrometers. Colloids with spherical shape usually form an fcc lattice. However, even minor different shape anisotropy or dipolar interactions can lead to other packing symmetries, such as hexagonal close-packed (hcp) or simple hexagonal phases.

The combination of two different sized and functionalized colloids in solution may lead to the formation of ordered binary super lattices. Multicomponent colloidal super lattices naturally provide a much broader range of compositions and structures as compared to the assemblies of one colloid component. When particles of different sizes and types are brought together, they have to adjust themselves to spatial constraints in a certain way.

Several strategies exist in order to direct crystallization in binary colloidal systems toward a binary super-lattice. The first and foremost principle is an entropic driving force in a concentrated mixture, which is based on the liberation of additional free volume as the liquid state transforms into a binary crystal. [50] The entropy of a system of spheres is composed of contributions associated with the degree of spatial ordering (the “configurational” entropy) and that associated with the space available to each particle for local motions (the “free volume” entropy). Confining the spheres of a binary solution to the lattice cells of a super lattice structure decreases the configurational entropy compared with a disordered fluid phase. However, the particles within a binary super lattice have more local free volume in which to move than they have in the fluid. Forming a binary super lattice increases the free volume entropy but at the expense of lowering the configurational entropy. At low concentrations, the configurational entropy dominates and the fluid is stable. But with increasing concentration, the gain in free volume entropy on binary super lattice formation more than compensates the loss of configurational entropy, and a stable binary super lattice is formed.

In the most simple mechanistic approach based on space filling, the formation of a binary assembly of hard and non-interacting spheres is expected to occur only if its packing density exceeds the packing density of single-component crystals in fcc or in hcp structure (~ 0.7405). [51,52] According to this expectation, the key factors determining the structure of binary super-lattices are particle size ratio ($\gamma = R_{\mathrm{small}}/R_{\mathrm{large}}$) and relative concentrations. Each structure has its own γ range of stability (TAB 1.1).

Table 1.1: Calculated size range of stability for binary crystals of hard spheres and their maximum packing density. [52]

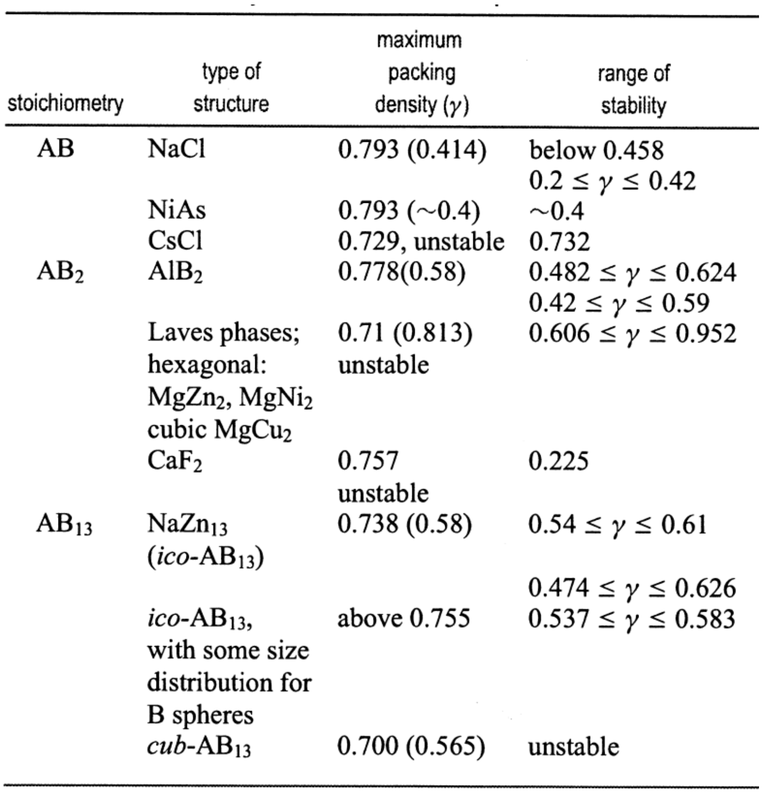

stoichiometry	type of structure	maximum packing density (γ)	range of stability
AB	NaCl	0.793 (0.414)	below 0.458 $0.2 \le \gamma \le 0.42$
	NiAs	0.793 (~0.4)	~0.4
	CsCl	0.729, unstable	0.732
AB_2	AlB_2	0.778(0.58)	$0.482 \le \gamma \le 0.624$ $0.42 \le \gamma \le 0.59$
	Laves phases; hexagonal: $MgZn_2$, $MgNi_2$ cubic $MgCu_2$	0.71 (0.813) unstable	$0.606 \le \gamma \le 0.952$
	CaF_2	0.757 unstable	0.225
AB_{13}	$NaZn_{13}$ (*ico*-AB_{13})	0.738 (0.58)	$0.54 \le \gamma \le 0.61$ $0.474 \le \gamma \le 0.626$
	ico-AB_{13}, with some size distribution for B spheres	above 0.755	$0.537 \le \gamma \le 0.583$
	cub-AB_{13}	0.700 (0.565)	unstable

In real systems, these entropic effects interfere with significant van der Waals attractions, which may be tuned by selecting index matching solvents [40] and with a coverage of the colloidal particles with a hairy layer of short polymer chains which introduces a steric repulsion.[53,54] These general tendencies can be assisted by the introduction of mutual interactions among the colloidal components. Such interactions are installed to act between particles from different components and are henceforth denoted as hetero-interactions. Along this line of thought, oppositely charged colloids were prepared and used to form binary super-lattices.[51-52,55] As the resulting electrostatic interactions are of long-range nature, an inert salt had to be added in order to appropriately screen the extent of the electrostatic interactions [55] or the charges on the colloidal particles had to be kept low enough by application of suitable capping agents or the crystals were formed according to a layer-by-layer addition of oppositely charged colloids [56]. In a detailed study on the occurrence of 16 binary assemblies the diversity of these structures were attributed to the impact of entropic effects, van der Waals attractions and electrostatic interactions among charges and dipoles.[51,52] Most of these attempts relied on a subtle interplay of sedimentation and solvent evaporation and a rather time consuming procedure had to be applied to achieve crystallization.

If only geometrical considerations are taken into account, the formations of super lattices like NaCl, $NaZn_{13}$, and AlB_2 can be expected. Contrary to atomic solids however, the nanoparticle super lattices possess extra degrees of freedom such as adjustable particle size and shape. Thus, super lattices with AB, AB_2, AB_3, AB_4, AB_5, AB_6, and AB_{13} particle stoichiometry with cubic, hexagonal, tetragonal, and orthorhombic symmetries have been identified. Shevchenko et al. [52] spent a lot of work with the entropy driven crystallization of nanometer sized semiconductor spheres. They could show that assemblies with the same stoichiometry can be produced in several polymorphous forms by modifying the particle size and deposition conditions. Numerous binary colloidal crystals which are isostructural with NaCl, NiAs, CuAu, AlB_2, $MgZn_2$, $MgNi_2$, Cu_3Au, Fe_4C, $CaCu_5$, CaB_6, $NaZn_{13}$, and *cub*-AB_{13} compounds were found by using various nanoparticle combinations. Currently, the structural diversity of binary colloidal crystals is explained by the interplay of multiple factors such as entropy, coulombic, van der Waals, charge-dipole, dipole-dipole, and other interactions, which all contribute to stabilization the binary crystal. [52]

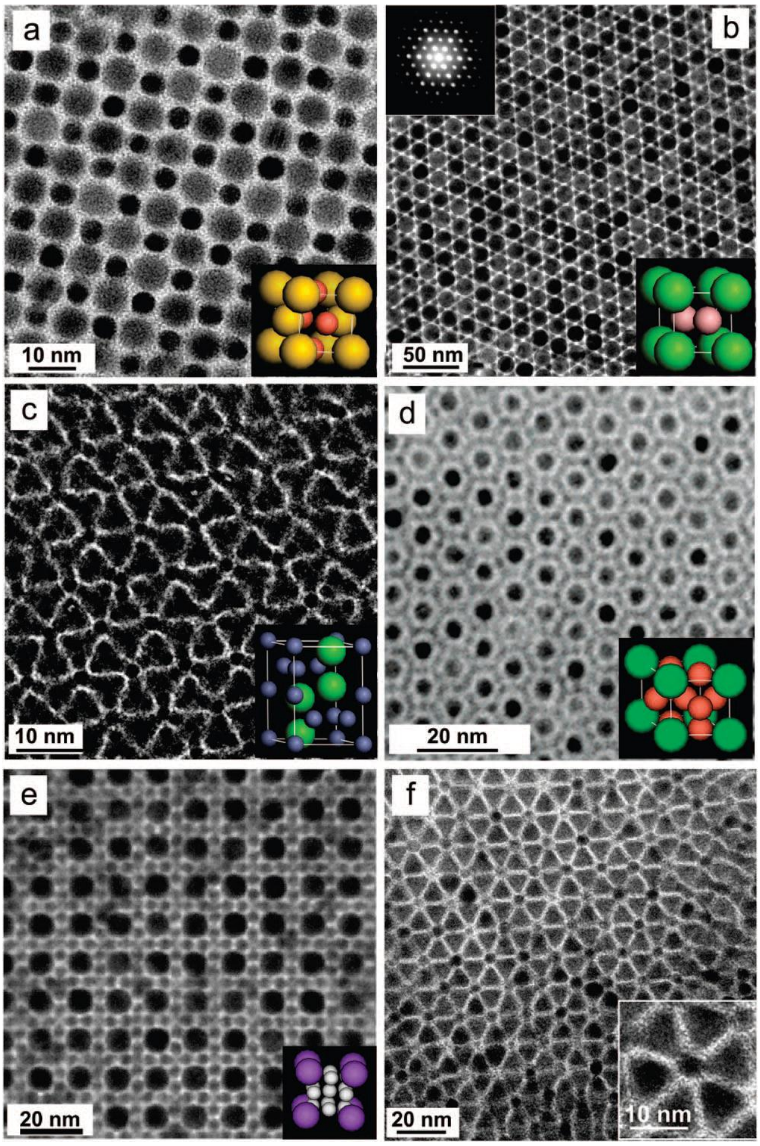

Figure 1.19: TEM images of binary colloidal super lattices self-assembled from various semiconductor, metallic, and magnetic nanoparticles. The bottom-right corner insets show the unit cells of corresponding structures. (a) (001) projection of AuCu type crystal formed by 7.6 nm PbSe and 5.0 nm Au nanoparticles. (b) (001) projection of AlB_2-type crystal assembled from 13.4 nm Fe_2O_3 and 5.8 nm PbSe particles. The top-left corner inset shows small-angle electron diffraction pattern. (c) (001) projection of Laves phase $MgZn_2$-type crystal formed by 6.2 nm PbSe and 3.0 nm particles. (d) (001) projection of $CaCu_5$ type crystal formed by 3.4 nm CdSe and 7.3 nm PbSe nm particles. (e) (100) plane of cub- AB_{13} type crystal formed by 8.1 nm CdTe and 4.4 nm CdSe nanoparticles. (f) Crystal self-assembled from LaF_3 triangular nanoplates (9.0 nm side) and 5.0 nm spherical Au particles. Pictures were taken from Shevchenko et al. [52].

Leunisssen et al. have reported an interparticular charge induced assembly of binary colloidal crystals. [55] They applied apolar solvents to match the density and refractive index of the colloids to avoid sedimentation and van der Waals attraction. The charges of the particles were fine-tuned by adding surfactants of opposite and dissimilar charges to avoid irreversible aggregation. All the resulting binary lattices showed nearly the same quality and were independent of the composition of the starting mixture of large and small particles. Even with micrometer-sized spheres, the authors were able to show various equilibrium phases, analogous to the atomic lattices of CsCl and NaCl.

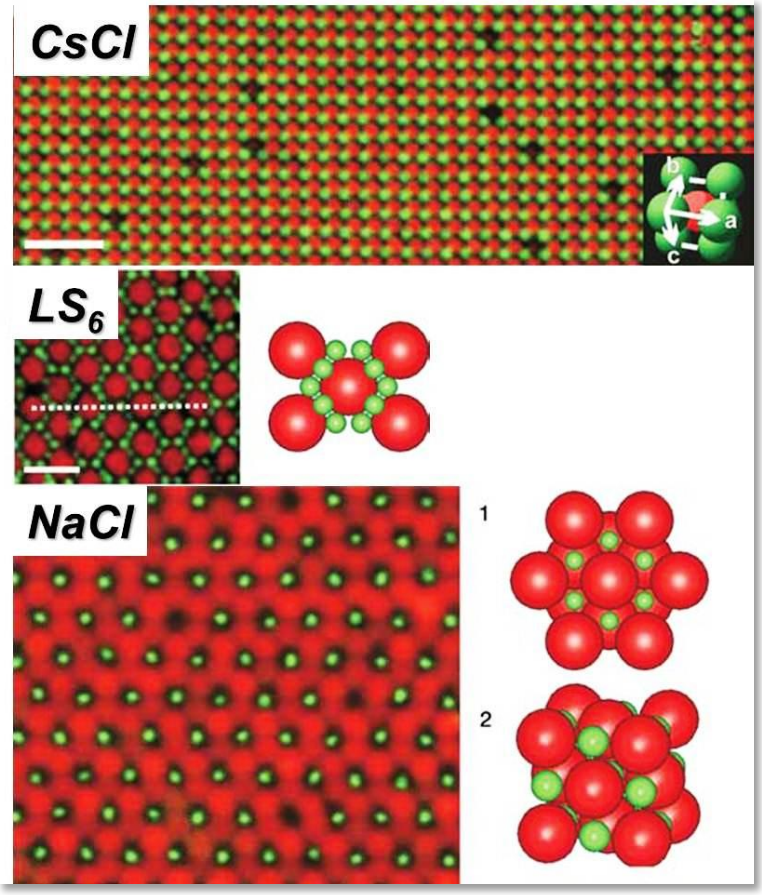

Figure 1.20: ***CsCl:*** Confocal micrograph of positive (red, radius 1.08 μm) and negative (green, 0.99 μm) PMMA-spheres building up a large (100) plane (scale bar, 10 mm). Inset, the cubic CsCl-type unit cell. ***LS_6:*** Positive (green, radius 0.36 μm) and negative (red, 1.16 μm) PMMA-particles forming a structure with LS_6 stoichiometry. **NaCl:** Charged (red, radius 1.16 μm) and uncharged (green, 0.36 μm) PMMA-particles building up a NaCl type crystal. Pictures were taken from Leunissen et al. [55].

In another important example for the assembly of interacting colloids, Lewis and co-workers [57] recently developed binary mixtures of attractive and repulsive microspheres, in which the structure of colloidal crystals formed by the attractive species and by the dynamics of the repulsive species, which can be tuned by solely varying the number ratio of the two constituents.

1.8 Hydrogen bonds

Hydrogen bonding interactions can play an important role in the organization of hierarchical systems and lead to materials with new structures and properties.

The use of H bonding functionalization on colloids may open new ways to direct the assembly of those colloidal particles to ordered superstructures. Since repulsion forces are always present to some extent in any system, the overall net attractive or repulsive interaction depends on the sum of all the interactions. (Figure 1.14) An important feature of H-bonding and of other weak attractive interactions in solution is that, at regular temperatures, only a fraction of the bonds are formed. While a certain number of new H-bonds are continually formed, an equal number of H-bonds are broken at equilibrium, due to the kinetic energy of motion of the interacting molecules. Contrary to the use of complementary charges H-bond forces are weaker than electrostatic interactions and hence of more reversible nature.

In 1980 *Emsley* [58] suggested a subdivision of H-bonds into three major classes (TAB 1.2). Hydrogen bond energies which extend from about 15-40 kcal·mol^{-1} form strong bonds, hydrogen bonds which extend from 4-15 kcal·mol^{-1} form moderate bonds and hydrogen bonds which keep below 4 kcal·mol^{-1} form weak bonds. This demonstrates a wider range of interatomic interactions than is observed for covalent or ionic bonds or van der Waals forces.

For this work we are dealing exclusively with moderate hydrogen bonds. Moderate hydrogen bonds are formed generally by neutral donor and acceptor groups, e.g. by

$$\mathrm{-O-H,\ \rangle N-H,\ ,-N(H)-H,\ and\ O\langle,\ O{=}C,\ N\langle}$$

in which the donor atoms *D* are electronegative relative to hydrogen and the acceptor atoms *A* have lone-pair unshared electrons. These are the most common hydrogen bonds both in synthetic chemistry and nature. They might be regarded as normal hydrogen bonds. Due to their selective interaction forces they are important and essential components for the structure and function of biological molecules. The discovery of the hydrogen bonding between the bases adenine and uracil and between guanine and cytosine by Watson and Crick (1953) [59] initiated the so called molecular biology. They stated that the hydrogen bonding between the bases is the major factor in determining the structure of the nucleic acids.

Table 1.2: Properties of strong, moderate, and weak hydrogen bonds suggested by *Emsley* [58]. *D* stands for hydrogen bond donor and *A* for hydrogen bond acceptor. ν_S is the observed IR active hydrogen bond frequency relative to a covalently bonded proton X---H.

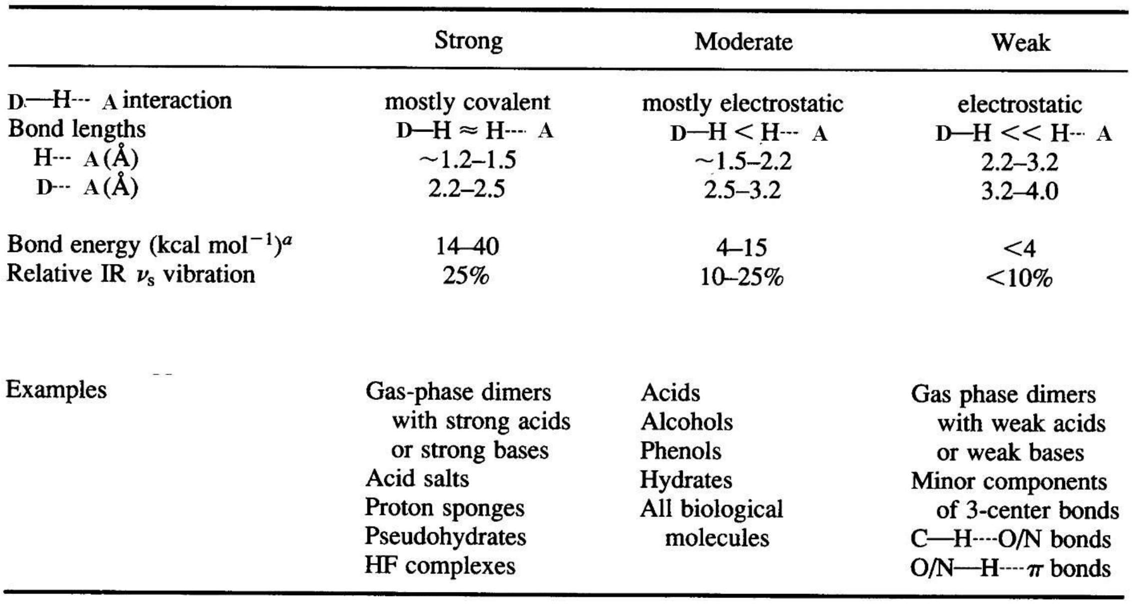

	Strong	Moderate	Weak
D—H--- A interaction	mostly covalent	mostly electrostatic	electrostatic
Bond lengths	D—H ≈ H--- A	D—H < H--- A	D—H << H--- A
H--- A (Å)	~1.2–1.5	~1.5–2.2	2.2–3.2
D--- A (Å)	2.2–2.5	2.5–3.2	3.2–4.0
Bond energy (kcal mol^{-1})^a	14–40	4–15	<4
Relative IR ν_s vibration	25%	10–25%	<10%
Examples	Gas-phase dimers with strong acids or strong bases Acid salts Proton sponges Pseudohydrates HF complexes	Acids Alcohols Phenols Hydrates All biological molecules	Gas phase dimers with weak acids or weak bases Minor components of 3-center bonds C—H---O/N bonds O/N—H---π bonds

It is at hand, that hydrogen bond interactions also offer new strategies in material design, e.g. the crystallization of binary colloidal systems toward a super-lattice. The formation of such binary crystals can be greatly assisted by specific interactions among the colloids from the two components respectively. In this sense, H-bonds may be a good choice as they are capable of providing complementary motifs. By now, there are a considerable number of publications in this field dealing with DNA-assisted colloidal aggregation. The concept was introduced by Mirkin et al. [60] and by Alivisatos et al. [61] in 1996. Both groups started with covering gold nano-particles with DNA strands and succeeded to reversibly self-assemble these particles into aggregates. Only recently, an excellent introduction into the field was provided by the Review from Geerts and Eiser [62]. However, the resulting self-assembly process, which is usually performed in aqueous systems, is controlled by many factors like temperature, pH, ionic strength and last but not least, the selection of a particular DNA bonding pattern. DNA bonding patterns apply various strategies like for instance supplying two colloidal fractions with two complementary DNA strands or adding a duplex DNA with two sticky ends to a binary colloidal mixture where each colloid is equipped with a DNA sequence complementary to one of the duplex ends respectively. In such DNA bonding patterns, the length of the DNA strands attached to the particles or used as connectors are further tunable factors. DNA functionalization in colloids is achieved via three alternative routes: attachment of DNA to neutravidin coated colloids via avidin-biotin complexation with the DNA strands covalently bound to biotin [63], binding of amino-labeled DNA via the carboxydiimide chemistry to polystyrene colloids [64,65] and, finally, swelling/deswelling based trapping of polyethylenglycol chains (PEG) to colloids with the DNA bound to PEG [66].

1.9 Motivation and goals of the present work: Hydrogen bond induced hetero-assembly in binary colloidal systems

As pointed out in Chapter 1.2 nanostructured materials using colloidal particles in the sub-micrometer range are of great relevance for the generation of photonic crystals. Under appropriate conditions colloidal crystals are able to show a photonic band gap as a result of the periodicity of the refractive indices. Monodisperse spherical colloids are most commonly used to form a cubic face centred structure. At a given ratio of the RIs it is possible to enhance the PBG in photonic crystals by changing the arrangement of the monodisperse colloids or alternatively vary the arrangement by switching to binary systems. A simple binary system is a NaCl like lattice. If interstitial lattice sites can be filled with silicon and the colloids can be removed, the resulting inverse air in silicon structure is expected to show a nearly doubled PBG compared to an inverse simple fcc structure.[19] As a consequence, the present thesis is aiming at the formation of binary super-lattices from binary mixtures of colloidal species. A crucial aspect in pursuing this goal is the impact of hetero-aggregation.

To form an ordered NaCl analogue crystal or another binary crystal with binary spherical colloids it is necessary to generate the proper size ratio. In addition it is beneficial to have complementary functionalizations on both colloidal components respectively. However, it remains challenging to form highly ordered colloidal crystals from sub micrometer particles.

The motivation of the present thesis is to introduce the benefits of complementary hetero-hydrogen-bonding into the crystallization process of a binary colloidal system. One goal is to obtain surface functionalizations of both colloids with multiple hydrogen bonding motives similar to those in biological systems. In Chapter 1.8 DNA-strands were mentioned to serve this purpose. But aside from the complexity of tuning the mutual interactions, furnishing the particles with an appropriate amount of DNA strands is a formidable task, notwithstanding the fact that DNA strands in its own are complex systems compared to its simple small molecular functionalities. Some reasons are: (i) homo-aggregation between colloids with equal types of DNA strands may be very pronounced. (ii) DNA is an elongated strand and thus causes undesired steric interactions in addition to the H-bonding. (iii) DNA-strands are expensive and not easy to synthesize or link onto colloids respectively. Therefore, the present Thesis suggests small hydrogen bond patterns that are bound covalently via comonomers. The self-assembly process of binary colloids should be supported and enhanced by colloids bearing for example triple-dentate complementary H-bond functionalization moieties like those shown in the scheme of Figure 1.21. Similar to DNA-functionalizations, such ligands with small H-bond patterns are not easily available, moreover difficult to synthesize and hard to link onto polymeric colloids.

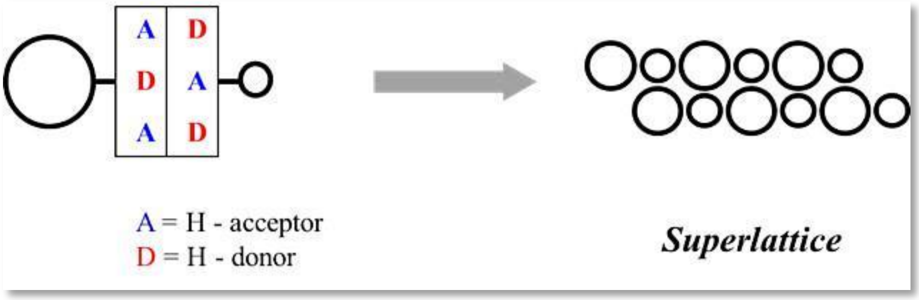

Figure 1.21: Scheme of complementary multiple hydrogen bond functionalizations of binary sized colloids leading to a crystalline super lattice.

A possible preparation of DAD functionalized polystyrene colloids that require a procedure with four synthetic steps is introduced in Chapter 2.1. Despite this effort, the concept of colloids with H-bond motif bearing co-monomers is considered to be an interesting alternative to the DNA functionalized particles. DAD colloids are less expensive and less laboriously to be prepared than the DNA functionalized colloids, exert H-bond interactions which can be tuned with simple low molecular weight antagonists, are based on covalently bound functionalities and are just as well applicable in non-aqueous solvent systems as in aqueous systems.

While taking a closer look on either multiple patterns like ADA, e.g. uracil, one might notice that those ligands are able to form H-bonds not only with its complementary form but also can build up H-bonds with itself. These are denoted as *wobble pairs*. [67] Uracil possesses six different wobble pairs shown in Figure 1.22. However, the presence of the direct complementary species, 2,4-diaminotrizine should lead to a stronger hetero-aggregation.

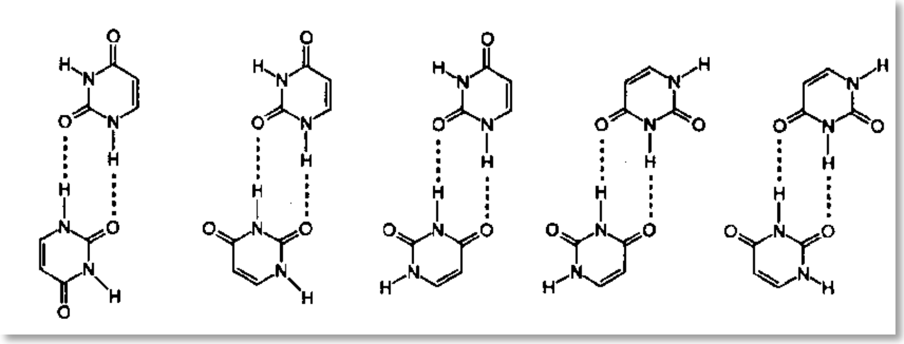

Figure 1.22: Ways of homo-base pairing of uracil – so called *wobble pairs*.

It might thus be helpful to also develop and characterize a simplified system with single hydrogen bond donors and acceptors on the two colloidal components respectively. At least this system might deliver a simple but useful combination of complementary functionalizations towards an exclusive hetero-assembly of binary colloids.

Different sized polymeric spherical colloids shall be prepared, which are able to aggregate and crystalize due to complementary single H-bond motifs. If the resulting colloids interact attractively via H-bonds there should be a clear cut difference of those H-bond functionalized colloids to the non-functionalized colloids. A suitable capping of the functionalizations on one of the respective colloids may help to moderate the extent of complementary H-bonding. In combination with a proper size ratio γ this may open up the opportunity to tune the aggregation and pave the way to new binary colloidal crystals.

1.10 Structure of the thesis

As suggested in Chapter 1.9, this work first introduces colloids with a complex tridentate uracil functionalization. The successful synthesis and their behavior in solution are analyzed extensively in Chapter 2. The system will enable us also to discuss some implications referring to hetero-aggregation with the use of tridentate H-bond motives.

It thus will turn out to be helpful to generate a binary colloidal system with a simplified surface functionalization using a single H-bond donor functionalization on one colloid and a single H-bond acceptor functionalization on the complementary respective colloid. Consequently, a binary colloidal combination with a vinyl pyridine functionalization on one side and phenol residues on the other side is introduced in Chapter 3 which concludes with a first demonstration of the feasibility of colloidal interaction and aggregation via complementary H-bonds.

This promising system of single H-bond moieties paved the way to controlled crystallization experiments treated in Chapter 4. Influences of several variables like the colloidal size ratio γ, the colloidal number ratio, the overall concentration and the type of substrate on super-lattice formation shall be followed in detail.

The work concludes with presenting an outlook in Chapter 5.

Chapter 6 will describe the experimental methods to synthesize and analyze colloids and binary colloidal systems. A brief introduction in emulsion polymerization will be given at first. Successively details of the colloid synthesis will be outlined. Then, the static and dynamic light scattering and the time resolved static light scattering will be described. The scanning electron microscopy and the ^{13}C solid state NMR will be briefly presented. Besides instrumental descriptions, the data evaluation procedures and the sample preparations are specified.

2. The triple hydrogen bond system

As already discussed in preceding chapters the formation of hydrogen bonds (single or multiple) can lead to a dramatic change in properties of the resulting assemblies. On a microscopic scale the presence of hydrogen-bond recognition elements in certain molecular building blocks can offer specific secondary structures, e.g. polymers having non-covalent main chains and side chains. [68] On a macroscopic scale those specific attraction forces lead to new material properties like a higher strength and/or an improved bending. In comparison to covalent bonds, which are stable under normal conditions and which can only be broken by providing sufficient energy, hydrogen bond formation is reversible and their strength depends on the chemical environment, such as the solvent or the temperature. Hence, hydrogen bonding can make a major contribution in the design of new polymer architectures and in polymer properties. Especially triple hydrogen-bonding motifs inserted in linear polymers have been studied extensively in the past by the research groups of Zimmermann et al. [69], Whitesides et al. [70,71], and Meijer et al. [72].

Mutual hydrogen bond interactions among colloidal components are new in literature and offer new strategies in order to direct crystallization in binary colloidal systems toward super-lattice. However, unlike to the simple homogeneous colloids, binary systems require a more complex pattern of interaction, which has to prevent pure components from domain formation. In this sense H-bonds may solve this problem as they are capable of providing complementary motifs. Complex multiple hydrogen bond patterns on colloid surfaces like ADA or DAD might support a directed crystallization in a particularly effective way.

In Chapter 2, colloids will be introduced that bear a DAD triple hydrogen bond pattern on their surface. The pattern is provided by a 2,4-diaminotriazine functionalization. This would give raise to the hope that controlled hetero-aggregation among complementary functionalized components will offer new ways to complex materials. For example there might be directly crystalizing colloidal super-lattices from a binary colloidal solution. In this context it is interesting to first analyze colloidal homo-aggregation by the unsymmetrical attractive interaction among two 2,4-diaminotriazine moieties, called wobble pairing. If homo-aggregation among the colloids exists molecular recognition of an antagonist with ADA pattern, e.g. uracil, on the colloids surface should be possible and observed (Figure 2.1).

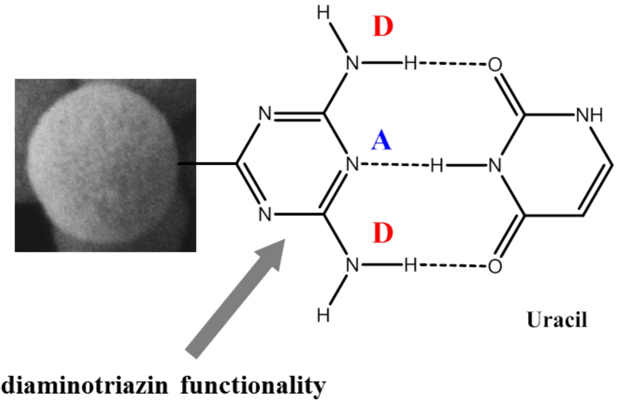

Figure 2.1: The image to the left is showing a 2,4-diaminotriazine functionalized polymeric colloid with a hydrodynamic radius of 115 nm. The DAD hydrogen bond pattern is capped by uracil. Uracil with its ADA hydrogen bond pattern is a direct antagonist of 2,4-diaminotriazine.

2.1 Colloid synthesis and ^{13}C CP/MAS NMR characterization

2,4-diaminotriazine functionalized colloids (PMS-Triazin-IV) provide a system capable of intra- and intermolecular self-assembly through a triple hydrogen bonding motif. Functionalization of the colloids with diaminotriazine moieties was obtained by carrying out a surfactant free emulsion polymerization (SFEP) with 90 mol% of pure 4-methoxymethylstyrene with 10 mol% 1,4-divinylstyrene as crosslinker. The methoxy groups (colloid PMS-M-I) were successively substituted against chlorine followed by a reaction of the chloromethyl groups (colloids PMS-Cl-II) with an excess of sodium cyanide. Reaction of the cyano functionalized colloids (PMS-CN-III) with dicyandiamide finally provided the 2,4-diaminotriazine bearing product PMS-Triazin-IV. A reaction scheme is given in Figure 2.2. Details to the entire reaction procedure can be found in the experimental section in Chapter 6.1.1.

For steric reasons it can be assumed that the final 2,4-diaminotriazine functionalizations are primarily on the surface of the colloids PMS-Triazin-IV. The whole reaction was successfully tracked by solid state ^{13}C-CP/MAS NMR. The spectra are shown in Figure 2.3.

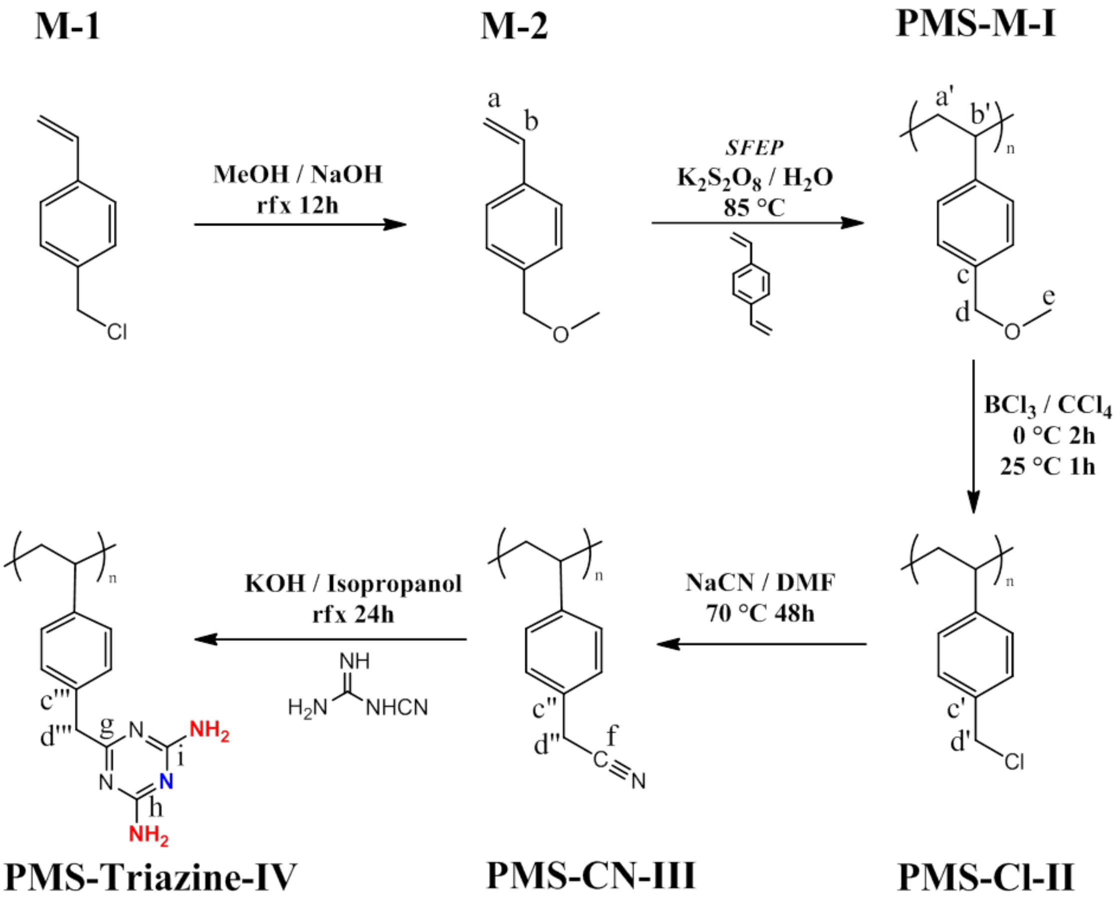

Figure 2.2. Scheme of the synthesis of DAD labeled colloids.

It is important to say that the peak intensities are not proportional to the respective number of carbon atoms because different carbon atoms have different cross polarization time constants. The spectrum of 1-(methoxymethyl)-4-vinylbenzene, depicted in the top of Figure 2.3, shows two peaks at 113 ppm and 116 ppm (labeled a and b), which are assigned to the C=C double bond of this monomer. In the spectrum of the 4-methoxymethyl functionalized colloid (PMS-M-I) (Figure 2.3, row 2), two new peaks, a' and b', appear at 39 and 46 ppm, respectively. They can be assigned to the polymer backbone. The peaks at 113 and 116 ppm are absent in the spectrum of

PMS-M-I, indicating that the polymerization was complete. The peaks of most carbon atoms not involved in the reaction stay at the same chemical shift except for the peak of the aromatic carbon atom connected to the main chain. This peak is shifted from 138 to 144 ppm. The polymer peaks are much broader than those of the monomer since different configurations and conformations of the amorphous atactic polymer lead to a spread in chemical shifts.

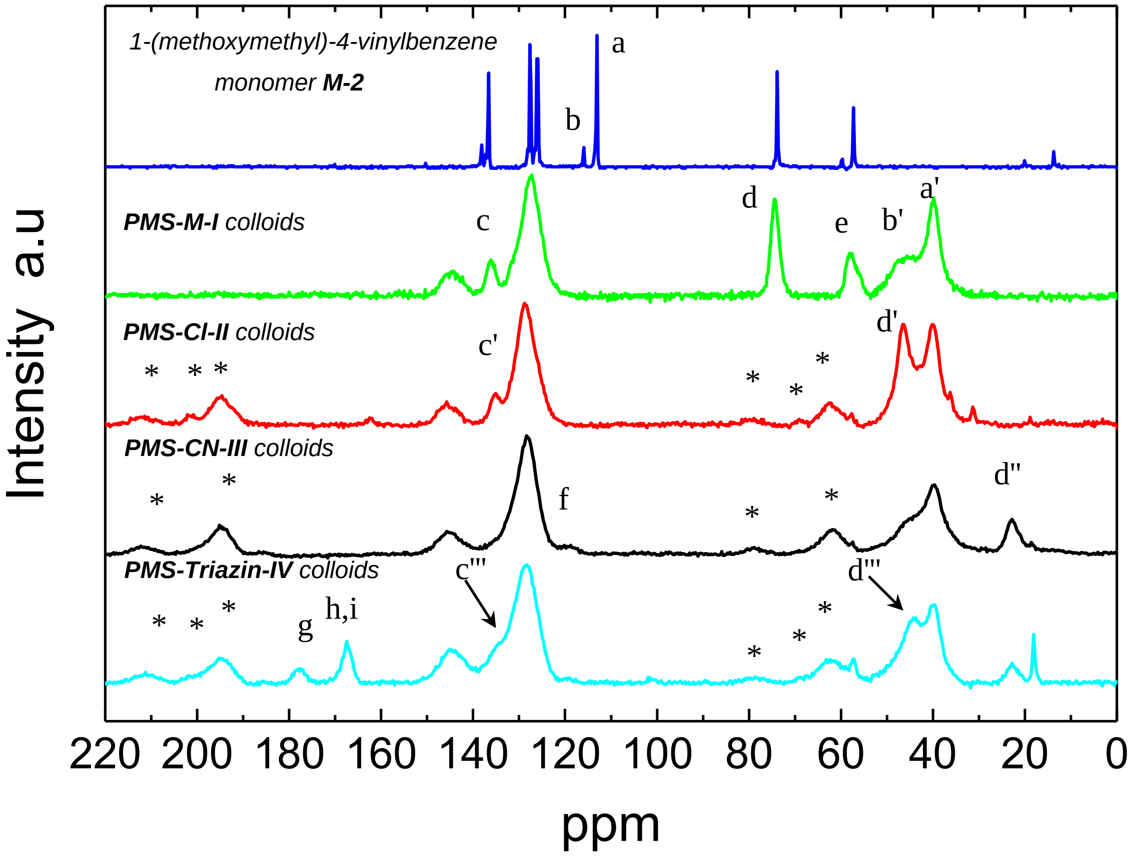

Figure 2.3: ^{13}C CP/MAS NMR spectra of the synthesized monomer *4-methoxymethyl styrene* (M-2) and the colloids obtained at a spinning rate of 5 kHz. Peak labels refer to those of the carbon atoms given in the reaction scheme in Figure 2.2. The asterisks denote the spinning side bands.

The third spectrum in Figure 2.3 was obtained from the 4-chloromethyl functionalized colloid (PMS-Cl-II). The peak from the methoxy group of PMS-M-I (carbon atom e) at 58 ppm disappeared in PMS-Cl-II. Furthermore, due to the stronger negative inductive effect of chlorine compared to oxygen, the methylene peak at 74 ppm (d) is shifted to 45 ppm (d'). This shows that colloid PMS-M-I was successfully chlorinated to form colloid PMS-Cl-II.

The spectrum of PMS-Cl-II is the first one showing spinning sidebands, indicating a lowering of the glass transition temperature due to the change of functionalities. Row 4 in Figure 2.3 shows the spectrum of the 4-cyanomethyl functionalized colloid (PMS-CN-III). When chlorine is replaced by the nitrile group, the methylene peak formerly at 45 ppm (d') shifts further to 22 ppm (d"). An additional small peak appears at 118 ppm, which belongs to the carbon atom in the nitrile group (f). The peaks c and c' at 136 ppm in polymers PMS-M-I and PMS-Cl-II have disappeared in the spectrum of PMS-CN-III. The peak of the corresponding carbon atom is shifted upfield and thereby hidden under the large peak of the aromatic carbon atoms at 127 ppm. The spectrum of the final product, the (2,4-diaminotriazine)methyl functionalized colloids PMS-Triazin-IV, is shown in the bottom of Figure 2.3. The two distinguished peaks at 166 and 177 ppm stand for the amino-substituted carbon atoms h and i and for carbon atom g of the triazine group. Two additional peaks are seen at 45 and 135 ppm, corresponding to carbon atoms d'" and c'", respectively. Their larger chemical shift values compared to the precursor can be attributed to the more electron-rich heterocycle compared to the nitrile. However, the remaining peak at 22 ppm shows that the last reaction was not complete. This is not surprising since a polymer analogous reaction involving a cycle with substituents cannot be expected to show complete conversion due to the steric hindrance.

After having established the successful preparation of PMS-Triazin-IV along the path outlined in Figure 2.2, we now discuss the colloidal properties of PMS-Triazin-IV in comparison to its precursor PMS-M-I.

2.2 Comparative SLS / DLS study of the precursor PMS-M-I and the final PMS-Triazin-IV colloid

The z-averaged diffusion coefficients in aqueous solution revealed by dynamic light scattering yield a hydrodynamic radius of 178 nm for the PMS-M-I. The colloids are crosslinked with 10 mol% 1,4-divinyl benzene and should not show a dramatic change in the size and distribution after passing the functionalization steps. Contrary, the evaluation of the DLS data for the end-product PMS-Triazin-IV yields an averaged hydrodynamic radius of 200 nm. In agreement with this increase in the hydrodynamically effective size, the radius of gyration R_g also adopts a larger value of 165 nm for PMS-Triazin-IV compared to R_g = 128 measured for PMS-M-I. A larger size of the PMS-Triazin-IV colloids can be caused by partial swelling due to a better solubility of 2,4-diaminotriazine moieties in water compared to the methoxy functionalized PMS-M-I colloids or alternatively due to a tendency to form oligomeric aggregates. Nevertheless, the structure sensitive factor ρ for PMS-M-I colloids with 0.72 as well for PMS-Triazin-IV colloids with 0.83 indicate homogeneous and compact spheres in both cases. Table 2.1 summarizes the characteristic parameters of the colloids PMS-M-I and PMS-Triazin-IV.

Table 2.1: Summary of particle properties including hydrodynamic radius (R_h), radius of gyration (R_g), shape sensitive parameter $\rho = R_g/R_h$, extent of polydispersity μ_2/Γ^2 from the experimental DLS data and the extent of polydispersity var $_{SZ}$ calculated from form factor fits based on equation (6.30).

Colloid sample	R_g [nm]	R_h [nm]	ρ	$\mu_2 / \Gamma^2_{(Cum)}$	var $_{SZ}$
PMS-M-I	128	178	0.72	0.08	0.03
PMS-Triazin-IV	165	200	0.83	0.32	0.10

The excess Rayleigh ratios $\Delta R(q)$ of the precursor colloid PMS-M-I and of the final colloid PMS-Triazin-IV, obtained from SLS, are represented in Figure 2.4. The least square fit to the scattering curves were performed with the SASfit freeware from PSI in Switzerland. As can be seen from the fits, the scattering experiment for PMS-M-I can perfectly be described with the model calculations for a polydisperse sphere with a Schulz-Zimm distribution of the colloid volume (top Figure 2.4, straight line). On the other hand, the 2,4-diaminotriazine-functionalized colloids PMS-Triazin-IV show a variation in the scattering form factor and a fit with the same model used already for the PMS-M-I colloids is not as good in the case of PMS-Triazin-IV colloids (bottom Figure 2.4, straight line). This may serve as a hint for aggregation of the functionalized PMS-Triazin-IV colloids. If di- or trimerization takes place the model for a hard sphere does no longer reveal reliable results. Further support for oligomerisation of PMS-Triazin-IV colloids is provided by an alternative fit based on polydisperse dumbbells (bottom Figure 2.4, dashed line), which is able to perfectly reproduce the experimental data. More details to the polydisperse dumbbell form factor can be found in the Experimental section in Chapter 6.2.6.

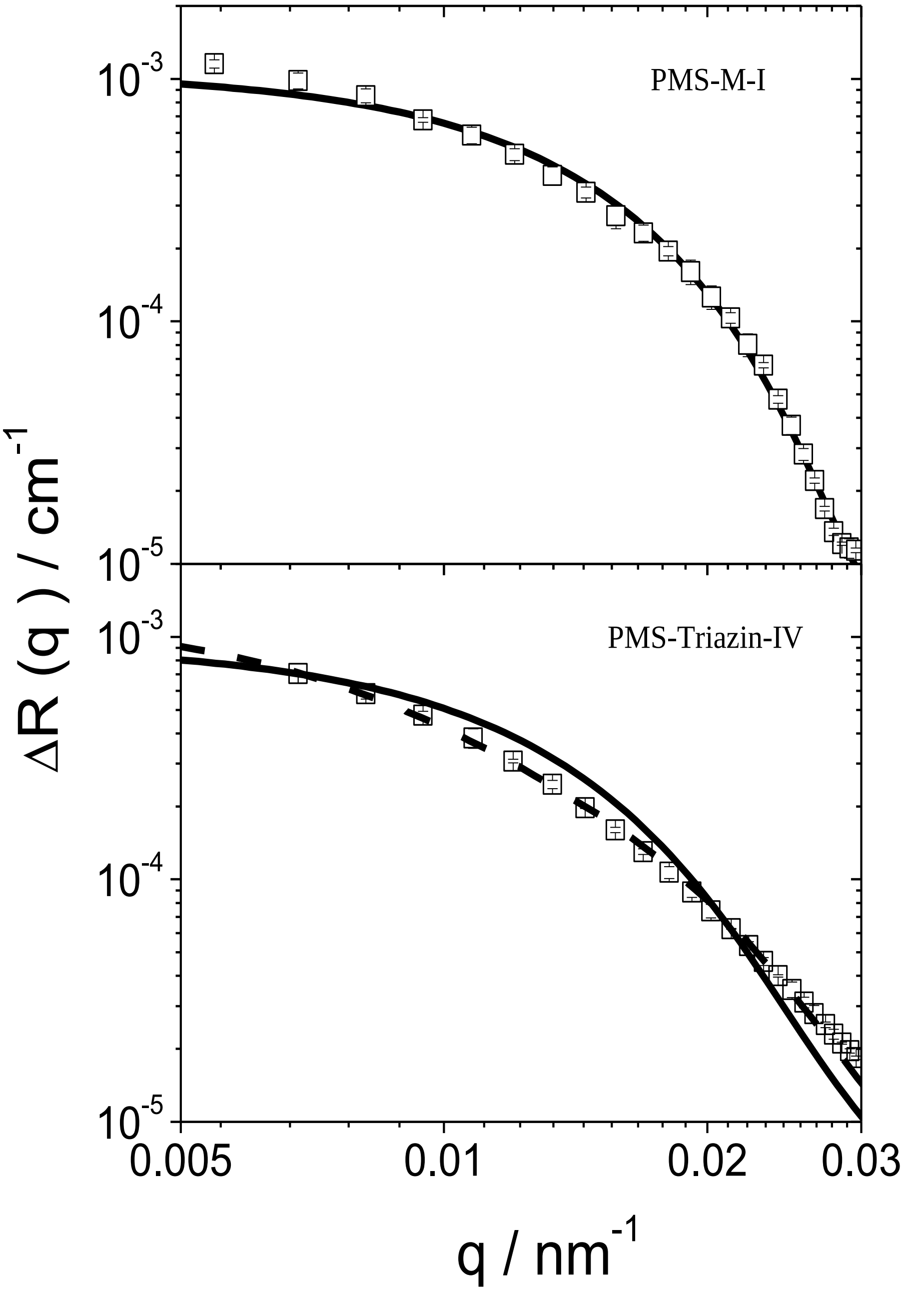

Figure 2.4: Excess Rayleigh ratios $\Delta R(q)$ of the precursor colloid PMS-M-I (top) and 2,4-diaminotriazine-functionalized PMS-Triazin-IV colloids (bottom) measured in aqueous solution. Straight lines give the best fits with a polydisperse sphere model based on a Schulz-Zimm distribution of the volume *V* according to Eq. (6.29, Chapter 6.2.6). The dashed line in the lower Figure shows the best fit with a polydisperse dumbbell according to Eq. (6.30, Chapter 6.2.6).

In addition the comparison of the distribution functions revealed from the CONTIN analysis (Figure 2.5) also indicates a larger polydispersity of the sample PMS-Triazin-IV than of PMS-M-I. The polydispersities var_{SZ} (Table 2.1) established from form factor fits and from the second cumulant analysis μ_2/Γ^2 (Table 2.1) of the correlation functions also results in a larger polydispersity for the sample PMS-Triazin-IV, hence supporting the hypothesis of oligomerisation of PMS-Triazin-IV. A detailed description of the approach to yield information of the polydisperity of the PMS-M-I and the PMS-Triazin-IV colloids in solution from the SLS data is given in the Experimental section in Chapter 6.2.6.

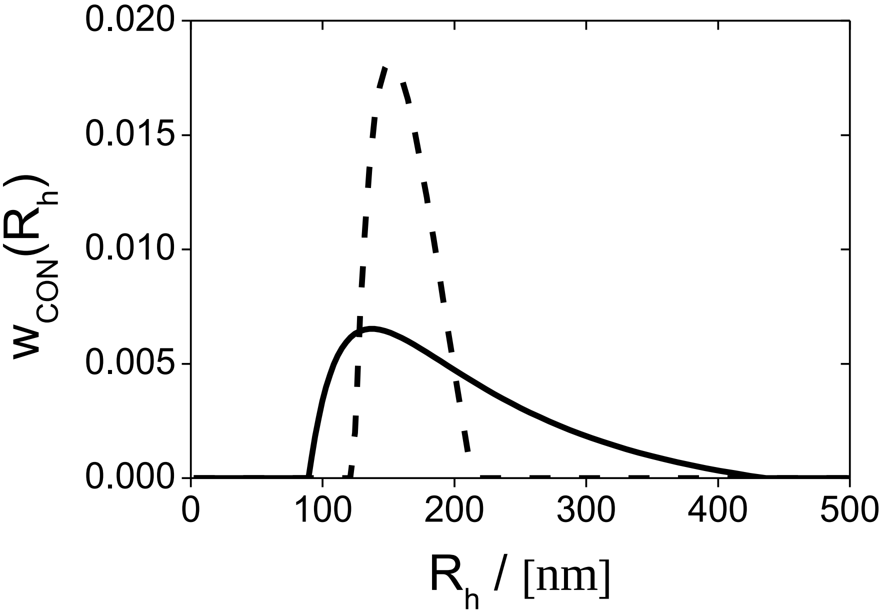

Figure 2.5: Colloid size distributions calculated from the CONTIN analysis at an angle of 30°. The lines indicate: Functionalized PMS-Triazin-IV colloids (▬▬); precursor colloids PMS-M-I (- - -).

2.3 SEM comparison of the precursor PMS-M-I colloid and the product PMS-Triazin-IV

The PMS-Triazin-IV colloid shows a behavior in solution slightly different to its precursor colloid PMS-M-I. However, we can clearly demonstrate that the colloids survive the 3-step chemical modification as colloidal entities. This confirmation is achieved by a comparison of SEM images from PMS-M-I precursors and from PMS-Triazin-IV colloids. A comparison of both SEM pictures, which do not show any significant variation is presented in Figure 2.6. In addition the obtained hydrodynamic size values of the PMS-M-I (R_h = 178 nm) colloids from light scattering are in good agreement with the colloid size values indicated by the SEM image.

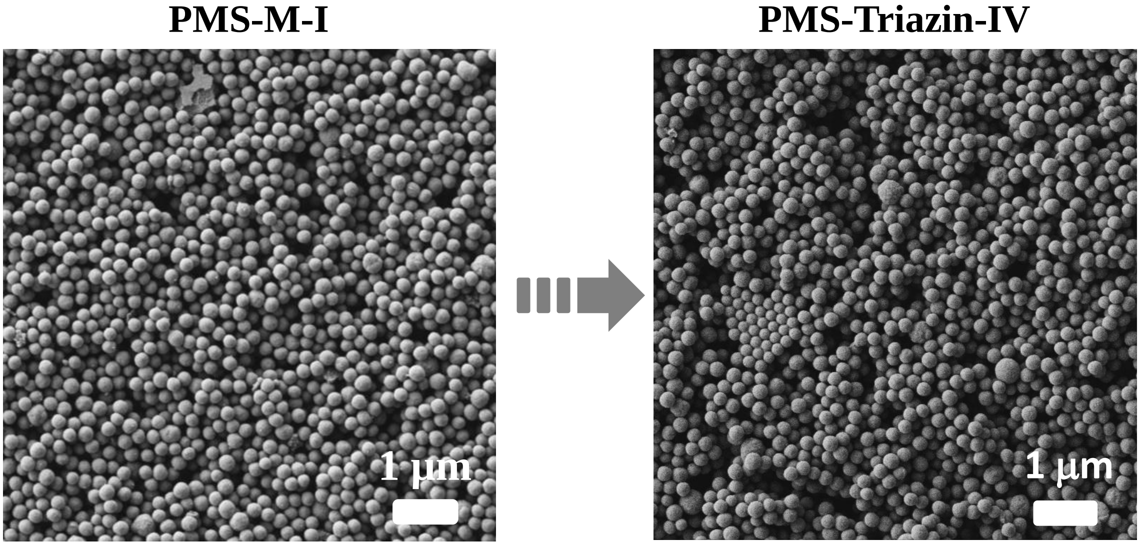
PMS-M-I **PMS-Triazin-IV**

Figure 2.6: Left side: SEM image of the PMS-M-I colloids directly after the surfactant free emulsion polymerization. Right side: SEM image of the PMS-Triazin-IV colloids. The particles stay apparently similar on the SEM images.

As already mentioned, the small discrepancies in the colloid size and in the quality of the form factor fits from PMS-M-I and from PMS-Triazin-IV may serve as a hint undergoing aggregation of the functionalized PMS-Triazin-IV colloids due to wobble base pairing. If a possible di- or trimerization takes place the model for a hard sphere in Figure 2.4 does no longer reveal reliable results.

2.4 Aggregation kinetics of 2,4-diaminotriazine functionalized colloids

The strong tendency to form aggregates is expected to be tunable by decreasing the concentration. Thus, highly dilute solutions may offer the opportunity to analyze the aggregation kinetics by means of time resolved static light scattering. At first a suitable solvent for such an aggregation experiments had to be selected. The following important aspects shall be considered carefully. The more polar the solvent is, the weaker the inter particular hydrogen bonds get because of the increasing solvation of donor and acceptor sites by solvent molecules. Therefore, we found no significant aggregation of the colloids PMS-Triazin-IV in pure ethanol while the aggregation of the particles in pure chloroform is too fast to be observed with TR-SLS even in high dilutions (c < 1.6 mg/L). THF turned out to be a suitable solvent for these experiments. In addition to the solvent variation the antagonist uracil can be used as tool to modify the aggregation process.

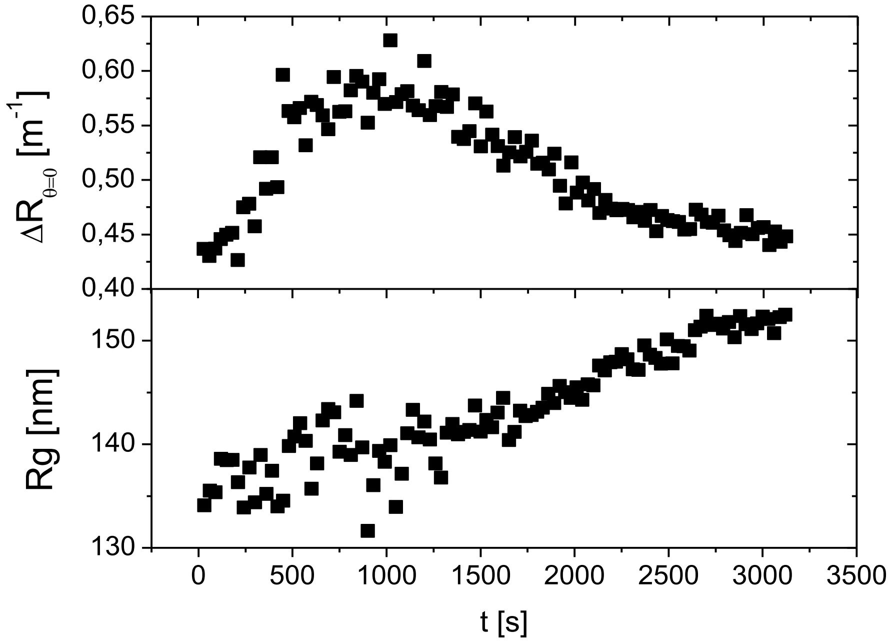

Figure 2.7: TR-SLS experiment of a solution of triazine functionalized colloids PMS-Triazin-IV in pure THF. The colloid concentration is 3.2 mg/L.

The graphs in Figure 2.7 show the characteristic parameters resulting from the time-resolved static light scattering of an aggregation experiment of the 2,4-diaminotriazine functionalized colloids in pure THF at a colloid concentration of 3.2 mg/l. The radius of gyration increases gradually from 134 nm to 154 nm within 3000 s. This is an increase of 20 nm. In line with the increase of R_g a growth of $\Delta R_{\theta=0}$ has been recorded. The latter parameter is a measure of the weight-averaged particle mass multiplied with the particle concentration. The decrease in $\Delta R_{\theta=0}$ beyond 1250 s is caused by sedimentation of the growing colloidal aggregates. The density of THF is only ~ 80 % compared to the polystyrene based PMS-Triazin-IV colloids. At a concentration of only 1.6 mg/L the time resolved experiment shown in Figure 2.8 did not show sedimentation anymore but yields an increase in size of only 10 nm within the same time regime as the one shown before in Figure 2.7.

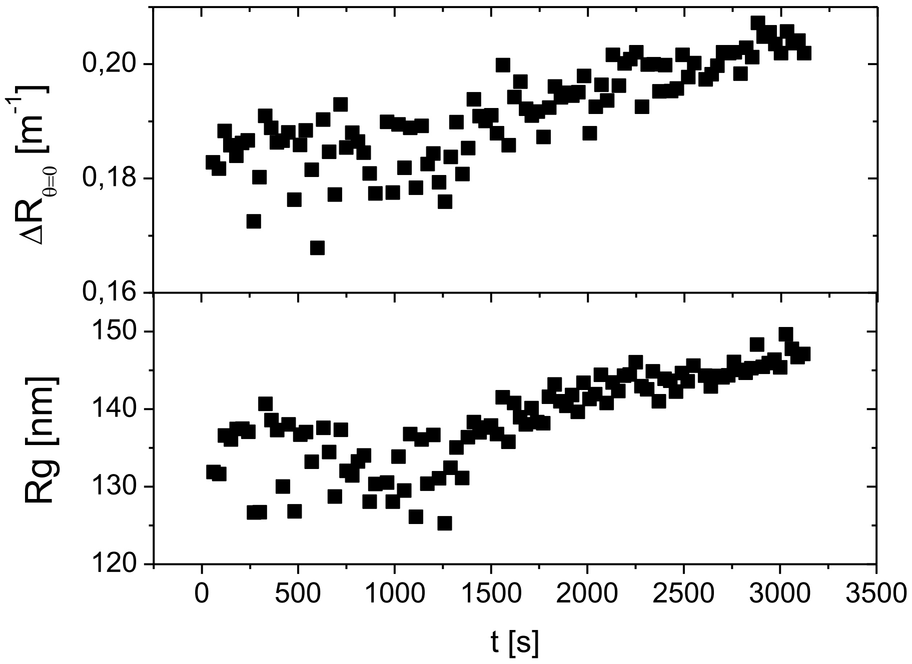

Figure 2.8: TR-SLS experiment of a solution of the 2,4-diaminotriazine functionalized colloids PMS-Triazin-IV in pure THF. The colloid concentration is 1.6 mg/L.

The aggregation is predominantly influenced by hydrogen bond interactions. Unlike the long-range electrostatic interactions, hydrogen bonds belong to the class of short-range interactions. See Chapter 1.8. In case of short range interactions, diffusion-limited aggregation takes place. At long enough times stable aggregates of two or more colloids may form and remain stable in the system. The low concentration of 1.6 mg/L or 3.2 mg/L has to be stressed as it may well explain that the increase in the radius is only 10 nm and 20 nm respectively.

In a combined SLS and DLS experiment Borkovec at al [73] followed a similar strategy and analyzed the onset of hetero-aggregation of spherical colloids based on opposite electrical charging. They succeeded to catch hetero-dimers as mutual intermediates in similarly low concentrations like those applied in the present work.

2.5 Docking of Uracil to the tridentate 2,4-diaminotriazine (DAD) moieties

Remarkably, the aggregation of the PMS-Triazin-IV colloids in THF presented in the preceding chapter could be fully inhibited by adding uracil to the colloid solution. Uracil with its ADA hydrogen bond pattern is a direct antagonist of 2,4-diaminotriazine and should be able to bind by hydrogen bond interaction preferentially on the triazine functionalities. Thus, the 2,4-diaminotriazine functionalized colloids are dissolved in THF saturated with uracil (12 mM). To verify whether aggregation can be inhibited, a time resolved experiment has been carried out in a THF solution saturated with uracil (12 mM) but otherwise under the same conditions as the aggregation experiment shown in Figure 2.7 performed at 3.2 mg/l.

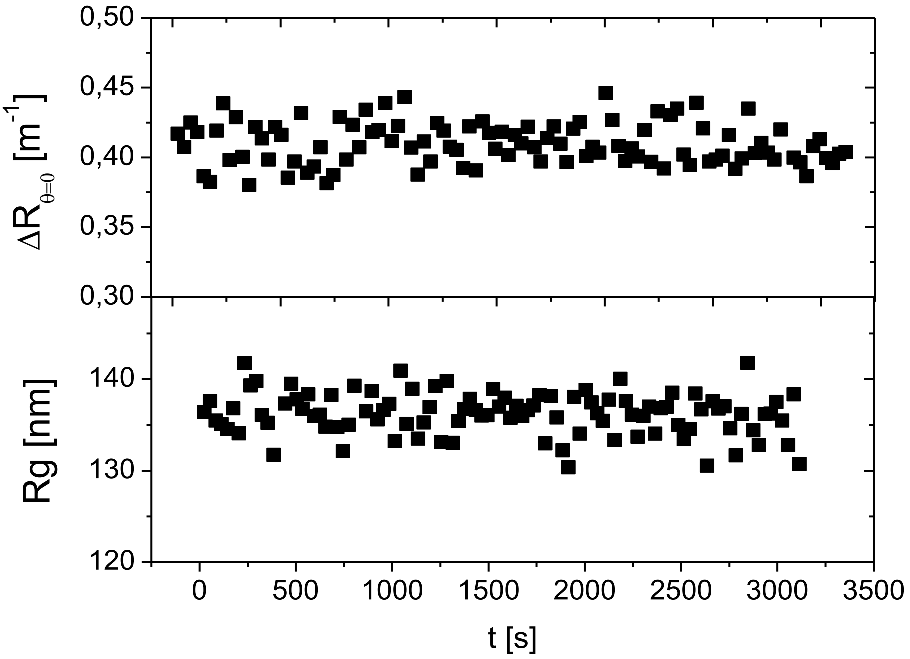

Figure 2.9: TR-SLS experiment of a solution of triazine functionalized colloids PMS-Triazin-IV in THF saturated uracil (12 mM). The colloid concentration is 3.2 mg/L.

Figure 2.9 clearly indicates that indeed no aggregation takes place anymore. The values for R_g and $\Delta R_{\theta=0}$ stay constant over the whole time. As a consequence this reference experiment is considered to be a proof for the hydrogen bonds to be the origin for aggregation of 2,4-diaminotriazine colloids in THF. It is possible to prevent this aggregation by completely capping the triazine moieties with the antagonist uracil.

The strong tendency of the PMS-Triazin-IV colloids to form hydrogen bonds is further more indicated by FTIR analysis. To this end we dissolved the 2,4-diaminotriazine functionalized colloids in THF saturated with uracil (12 mM). It is expected, that uracil binds considerably to the 2,4-diaminotriazine functionalized colloid surface. Figure 9a shows the spectrum of the pure 2,4-diaminotriazine functionalized PMS-Triazin-IV colloids with the characteristic N-H bands at 3300 – 3500 cm^{-1} and at 1600 cm^{-1}. Additionally a broad absorption regime is observable between 2500 – 3500 cm^{-1}.

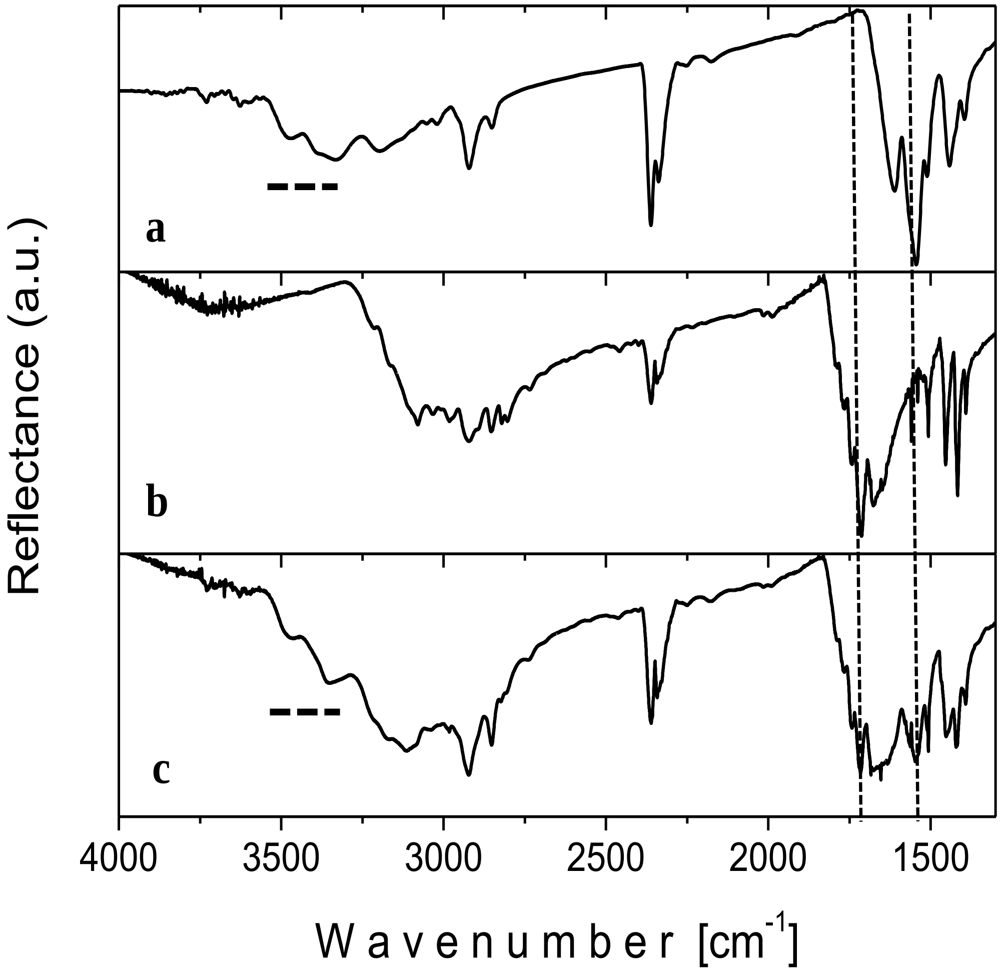

Figure 2.10: FTIR spectra of pure PMS-Triazin-IV colloids (a), pure uracil (b) and the dried mixture of both components (c) after three cycles of centrifugation and addition of pure THF. All samples were analyzed in the dried state in reflection.

This feature is considered to be characteristic for the self-associated 2,4-diaminotriazine residues. Elmsley [58] and Rossotti [74] found a similar broadening in the IR absorbance in systems of self-associated pyrazoles and imidazoles. As expected, a comparable behavior was also revealed for pure uracil in spectrum 10b. Uracil is also able to form inter molecular hydrogen bonds. In a mixture of uracil and PMS-Triazin-IV colloids recovered from a solution in THF saturated with uracil we found a combined IR pattern of both components even after two centrifuging cycles and successive addition of pure THF (spectrum 10c). Hence, the uracil cannot be removed by even three washing cycles, which indicates clearly a successful surface functionalization of the colloids and the recognition and strong binding of uracil on those functionalizations.

2.6 Conclusion

The synthesis of new colloids functionalized with a triple hydrogen bond motif was accomplished by means of surfactant free emulsion polymerization followed by three further synthesis steps. The functional groups are 2,4-diaminotriazine residues which bear a donor-acceptor-donor (DAD) pattern. Successful reaction was verified by ^{13}C-CP/MAS solid state NMR. Detailed characterization of the precursor colloids and the 2,4-diaminotriazine colloids via combined static and dynamic light scattering and SEM suggests a compact spherical shape of the PMS-M-I precursor colloids but light scattering of the PMS-Triazin-IV colloids did not show the same clear cut result. However, SEM imaging confirmed the conservation of the colloidal entities throughout chemical modification. Due to their functionalization, the colloids are able to aggregate in a suitable solvent via hydrogen bond formation. We were able to show that even in solvents with high polarity the formation of such hydrogen bonds is not completely inhibited. It turned out that THF is a convenient medium to dissolve the 2,4-diaminotriazine functionalized colloids while exhibiting controlled and gradual aggregation. This was analyzed in highly dilute solution by time resolved static light scattering in a concentration regime as low as a few mg per liter. If THF was saturated with uracil (12 mM) no aggregation of the colloids was observed any more. Uracil with its hydrogen bond pattern ADA is the direct antagonist of 2,4-diaminotriazine and could thus successfully be used to completely cap those functionalities on the colloids. Consequently, uracil cannot be removed from the colloids even with three THF washing cycles. This was scrutinized by IR measurements.

These promising results give raise to the hope that controlled hetero-aggregation among complementary functionalized components, like the present colloids on the one side and any tailor-made second colloid component or linear polymer with an antagonist functionalization on the other side will be feasible. This optimistic view is justified by the prospective of tuning the hetero-aggregation, while simultaneously suppressing homo-aggregation. At the same time PMS-Triazin-IV colloids turned out to act as a carrier for specific molecules as soon as they are tagged with an antagonistic H-bond motif.

However, an even more promising system for a binary colloidal crystallization, which is not able to form homo-aggregates at all, seems to be a simple H-bond donor functionalized colloid mixed with its antagonist which is a simple H-bond acceptor functionalized colloid.

3. The single hydrogen bond system

In the present chapter, a second strategy to insert mutual interactions among the colloidal components will be introduced. In analogy to Chapter 2, the strategy here is based on the coverage of colloidal particles with complementary H-bond patterns. The simplest complementary H-bonding motif in this sense is to cover one colloidal component with a single H-bond donor and the other colloidal component with single H-bond acceptor. This procedure completely avoids homo-aggregation among the colloidal particles of either sort.

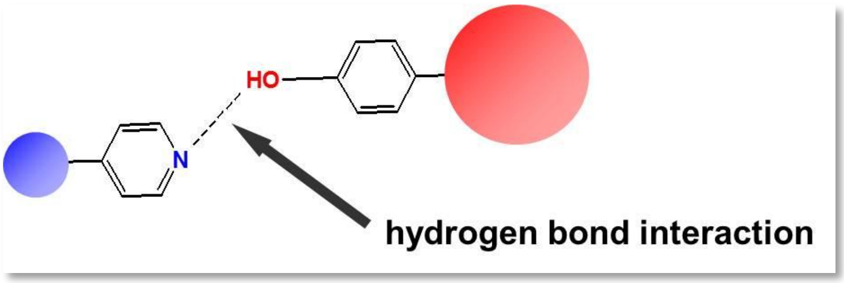

Figure 3.1: Schema of a simple single hydrogen bond interaction.

4-hydroxy styrene functionalized crosslinked polystyrene colloids (4OH-colloids) were synthesized as one component and 4-vinyl pyridine functionalized crosslinked polystyrene colloids (4VP-colloids) as the second component. Polymerization was carried out by means of surfactant free emulsion polymerisation (SFEP). This method yields monodisperse colloids without the use of surface active substances which might interfere with any interactions anticipated between our particles.

With the corresponding colloids available, the capability to form H-bonds will be proved first, both with complementary monomers or with complementary colloids. In the successive step, the system is analyzed for the appearance of hetero-aggregation among the colloidal components. Finally, first attempts to control the strength of these hetero-interactions shall be outlined, suggesting a promising route to generate binary super-lattices from these complementary colloidal systems.

3.1 Colloid synthesis and characterization

By varying the total monomer concentration in the SFEP processes different colloid sizes over a broad range are accessible. This is an important prerequisite for designing appropriate size ratios in binary colloid mixtures. As mentioned before, the size ratio of Na^+ to Cl^- ions in the NaCl crystal is $\gamma = r_{Cl^-}/r_{Na^+} = 0.55$. The highest packing density of a NaCl-type lattice or 79.3% is reached at a size ratio of 0.458. Based on non-interacting hard sphere model calculation the highest stability should be reached at size ratios in the range of 0.2 to 0.42. [50,52]

Table 3.1: Characteristic parameters of all synthesized colloids determined by SLS and DLS in $CHCl_3$ and of the colloids 4VP-1 and 4OH-3 in H_2O and of the colloids 4VP-1, 4OH-ref and 4OH-4 in a mixture of 70wt% toluene and 30 wt% $CHCl_3$. The total monomer concentration refers to the SFEP. Column seven gives two examples of the zeta potential of the respective colloids in $CHCl_3$.

Colloid sample	**total monomer conc. [mol / L]**	**R_g [nm]**	**R_h [nm]**	**ρ**	**μ_2 / Γ^2**	**z [mV]**
4VP-1	0.15	54.0	120.1	0.45	0.114	
4VP-1 (Tol70/Chloro30)	0.15	55.0	102.0	0.54	0.084	
4VP-2	0.20	81.3	137.8	0.59	0.071	26.7±5.4
4VP-2 (Tol70/Chloro30)	0.20	79.5	125.1	0.59	0.071	
4VP-2 (H_2O)	0.20	65.6	81.5	0.81	0.091	
4VP-3	0.66	154.9	212.2	0.73	0.066	
4OH-1 (Tol70/Chloro30)	0.09	57.8	93.2	0.62	0.046	
4OH-1	0.09	74.9	101.5	0.74	0.039	
4OH-2	0.12	117.5	150.9	0.78	0.129	
4OH-3	0.24	209.2	267.7	0.78	0.147	27.6±4.3
4OH-3 (H_2O)	0.24	185.9	224.3	0.81	0.112	
4OH-4	0.30	213.5	291.6	0.73	0.098	
4OH-4 (Tol70/Chloro30)	0.30	198.3	259.6	0.76	0.109	

The normalized form factors from SLS measurements of 4VP-2 and 4OH-3 are represented as an example in Figure 3.2. The experiments are in good agreement with the model calculation for a compact sphere. All SFEP synthesized colloids exhibit a similar behavior. An evidence for homogenous and monodisperse spheres is the appearance of a sharp minimum in the scattering function of the larger colloids (■). The inset is showing the narrow size distribution obtained by CONTIN for both colloids respectively.

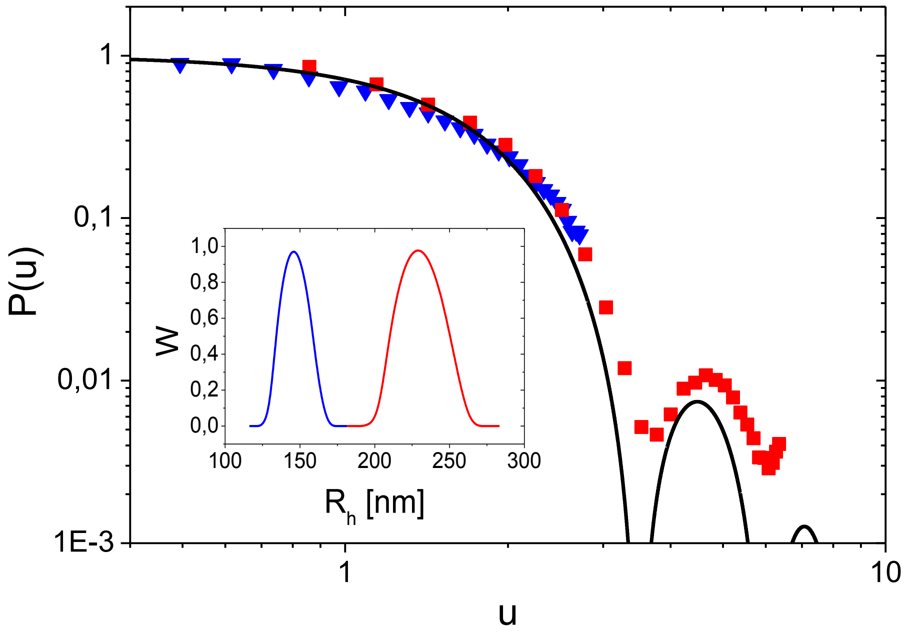

Figure 3.2: Form factor P(u) versus normalized momentum transfer $u = q R_h$ for the sample 4VP-2 (▼) and 4OH-3 (■) in $CHCl_3$. The solid black line represents the form factor for hard spheres [69]. SLS characterization in $CHCl_3$ solution indicates a spherical shape for the colloids. In comparison to measurements in H_2O and to the SEM pictures the colloids are slightly swollen in $CHCl_3$. The inset shows the distribution of the hydrodynamic radii obtained by a Contin analysis from DLS in $CHCl_3$ for both samples (small 4VP-2, large 4OH-3) at a scattering angle of $\theta = 30$ ° ($q = 0.0088$ nm^{-1}). The size distributions from DLS are monodisperse.

The resulting monodispersity of the colloids is due to the initiation of the polymerization process in the aqueous phase and the limiting solubility of the used monomers in water. It is this low equilibrium concentration which allows to control the resulting structure of the particles. The added comonomers, 4MeOS and 4-vinyl pyridine, are both much more water soluble then styrene. An initiation with KPS leads to a polymerization start in the aqueous phase. A detailed reaction scheme is given in Chapter 6.1.2. 4-vinyl pyridine chains or 4MeOS chains respectively grow until a critical degree of polymerization is reached and the short free radical chains adsorb onto the styrene / DVB droplets and polymerize them. This procedure [75] results in spherical particles with a surface that is enriched with the added polar comonomers. The resultant “core-shell” colloids are composed of a core with predominantly polystyrene and a shell enriched with poly-4-vinyl pyridine or poly-4MeOS segment respectively. Table 3.1 summarizes the characteristic parameters of the colloids used in the present work.

IR spectra of pure 4MeOS precursor colloids, 4OH colloids and pure 4VP colloids in KBr tablets are given in Figure 3.3. The successful conversion is proved by the appearance of the characteristic OH peak around 3500 cm^{-1}. Whereupon the sharper spike at 3600 cm^{-1} belongs to the free OH-groups and the broader band around 3400 cm^{-1} belongs to the intercolloidal hydrogen bonded OH-groups.

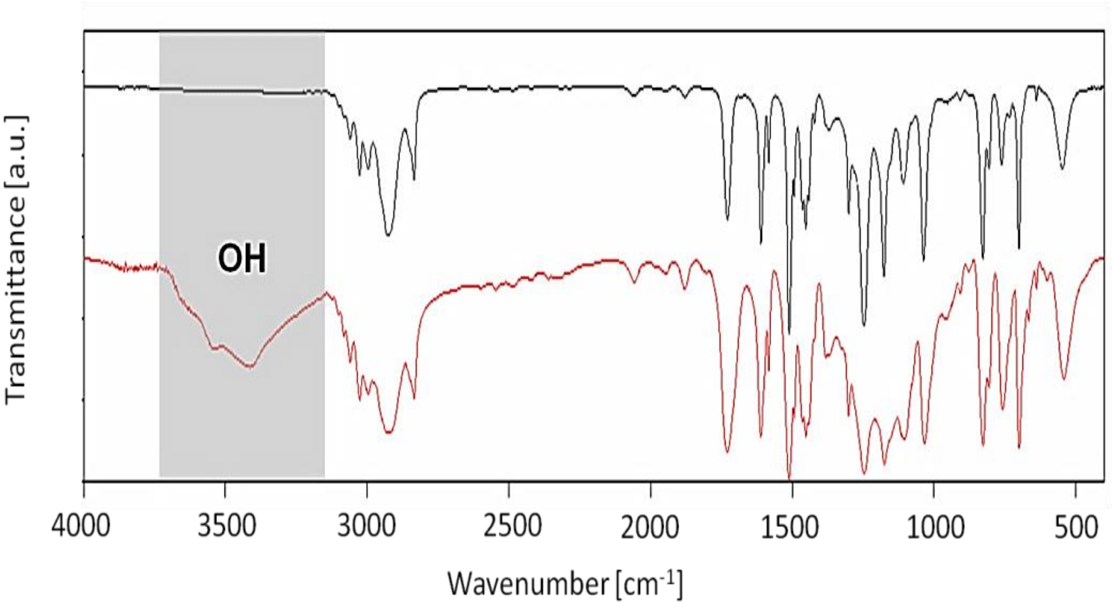

Figure 3.3: IR spectra. The black line represents the phenolic methoxy functionalized precursor. The red line represents the colloid sample 4OH-2 after silylation and hydrolysis of the given precursor. Measurements were performed with KBr tablets containing 5 wt% colloid.

Figure 3.4 shows the IR spectra of pure 4VP-2 and pure 4OH-3 colloids in the wavenumber (λ^{-1}) range of 2000 cm^{-1} to 4000 cm^{-1}. The evidence for OH functionalization in the 4OH-3 colloids is indicated by the characteristic free

(3600 cm^{-1}) OH band and their H-bonds (3400 cm^{-1}). Additionally Figure 3.4 (blue line) shows the IR hetero aromatic bands of the 4VP-2 colloids. Quantitative determination of comonomer content in the colloidal samples was performed by elemental analysis with a vario MICRO Cube (Elementar, Germany) on vacuum dried samples. The content of 4VP comonomer in the 4VP-colloids was analyzed by means of the nitrogen content. The content of 4OH comonomer in the 4OH-colloids was analyzed with the oxygen content. Elemental analysis of oxygen in the 4OH-3 sample gives a 4MeOS precursor comonomer incorporation of 74 % with respect to the used comonomer amount in the SFEP. Elemental analysis of nitrogen in 4VP-2 colloids gives a total 4-vinyl pyridine comonomer incorporation of 67 % with respect to the used comonomer amount in the SFEP. Thus, IR analysis proves the successful incorporation of the desired functional groups.

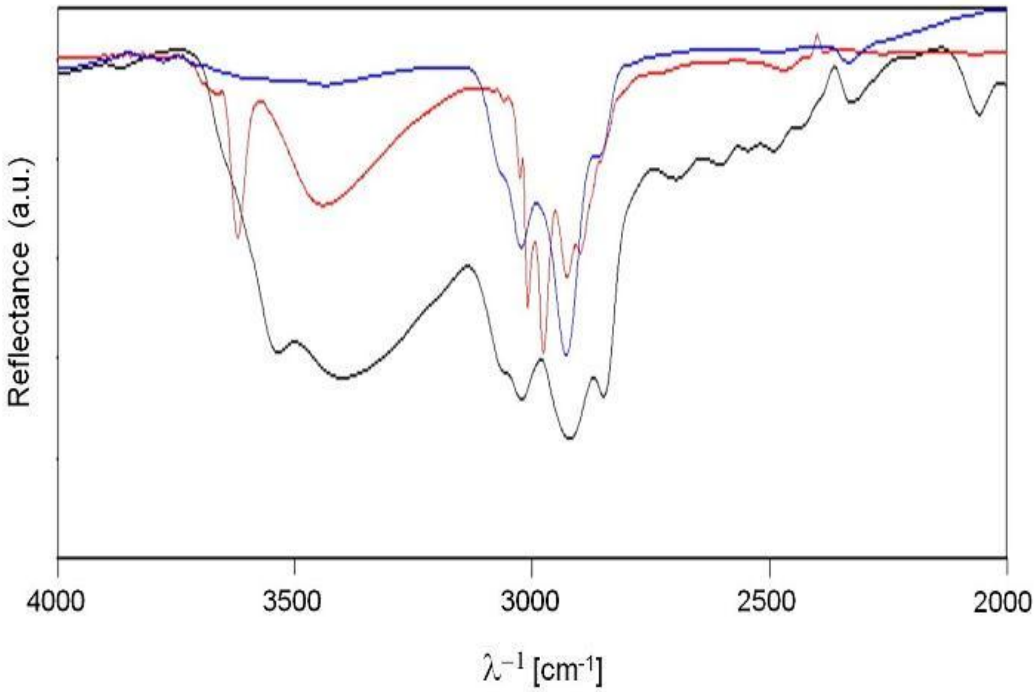

Figure 3.4: IR-spectra in the range of 2000 - 4000 cm-1 of the pure 4VP-2 colloids (blue line) and of the pure 4OH-3 colloids (red line). The black line shows the IR-spectra of the aggregates of this mixture after precipitation. A broad decrease with several subsidiary minima in the reflectance intensity in the range of 2200 - 3200cm^{-1} is due to the H-bond between the complementary functionalized colloids [67,74]. The experiments were made with dried samples in reflectance.

3.2 Combination of the complementary single hydrogen bond functionalized colloids in $CHCl_3$

The combination of the small colloids 4VP-2 and the large colloids 4OH-3 was performed first in chloroform solution. This combination offers a size ratio γ of 0.36 based on the hydrodynamic radii of 4VP-2 colloids to 4OH-3 colloids in water. However, water is a bad solvent for the present colloids and hard sphere like behavior similar to their dry conditions can be expected. $CHCl_3$, in turn, is a good solvent for the synthesized colloids and the particles are slightly swollen in $CHCl_3$ but still compact. In $CHCl_3$ a slightly increased size ratio of $\gamma_{\mathrm{Rh(4VP\text{-}2)\,/\,Rh(4OH\text{-}3)}} = 0.52$ was revealed. In addition the aprotic $CHCl_3$ is not able to break or inhibit possible H-bond interactions between the colloids. These conditions are considered to be an essential prerequisite to build up a binary super-lattice and $CHCl_3$ was chosen as solvent for further analysis in this Chapter.

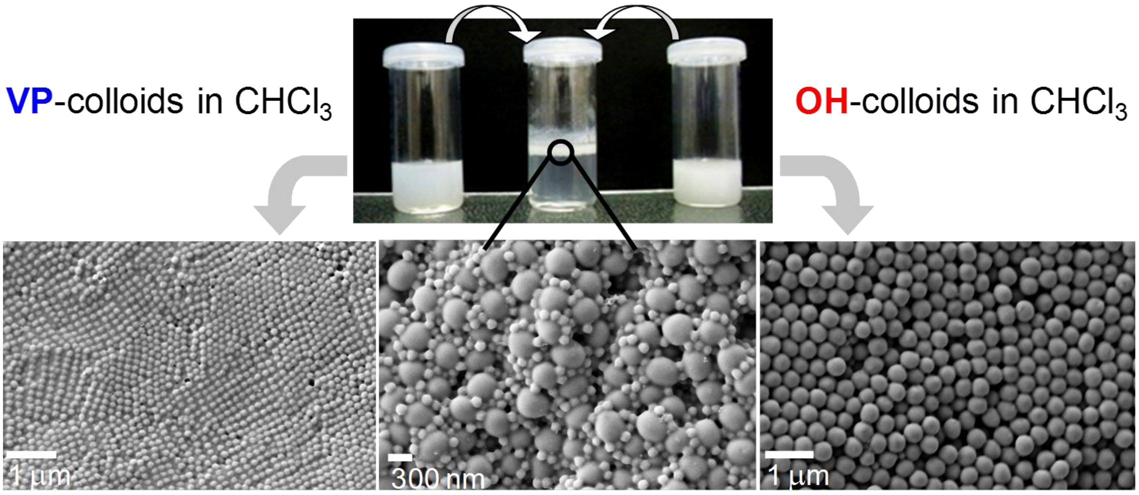

Figure 3.5: Stable chloroform solutions of small vinyl pyridine functionalized colloids 4VP-2 (left side) and large phenolic OH functionalized colloids 4OH-2 (right side) before and after combination (center) together with SEM pictures of the respective dried samples.

An exciting moment was the combination of two milky but stable dispersions containing complementary colloids in $CHCl_3$ at a total colloid concentration by weight of 3%, which is considered to be a high concentration. Represented in Figure 3.5 a clear solution with floating aggregates was formed immediately. The corresponding SEM images show the dried single colloids, 4VP-2 and 4OH-3, and the dried floating hetero-aggregates. This process is surprisingly fast and within approximately 1 minute the hetero-aggregation is completed.

It can be seen that the aggregates are still far from being crystalline. However, hetero-aggregation between 4VP-2 and 4OH-3 is considered to be a clear evidence of hydrogen bonds between the two colloid components in $CHCl_3$. From systems with opposite charges it is well known that electrostatic long-range attractions lead to irreversible colloidal aggregation. Hydrogen bonds are not long-range attractive forces. However, they still seem to be too strong to reveal well-ordered lattices. As already stated in Chapter 1.8 the present hetero-aggregates are based on H-bonds formed by neutral donors and acceptors in which the bond energy extends over a regime of 4 - 15 kcal / mol. [58]

Further evidence for hydrogen bonds between the 4VP-colloids of the sample 4VP-2 and the 4OH-colloids of the sample 4OH-3 is given additionally in Figure 3.4. The IR spectrum of dried aggregates in reflectance shows a very broad band located in a wave number range of $2200\ \mathrm{cm}^{-1} < \lambda^{-1} < 3200\ \mathrm{cm}^{-1}$. Several secondary transmission minima, which are considered to be characteristic for self-associated compounds, show strong H - bonded Ph-OH – N groups. Elmsley [58] and Rosotti [74] found this characteristic change in the IR transmittance in systems of self-associated pyrazoles and imidazoles respectively in solution. In addition to this, the band of free OH groups decreases relatively to the band of H-bonded OH groups. Altogether this behavior was found even more pronounced in the system of pure 4-vinyl pyridine and phenol as complementary compound in CCl_4 as well as in the two other possible combinations 4VP colloids + phenol and 4OH colloids + pyridine. Those spectra can be found in the following (Figure 3.6 + 3.7).

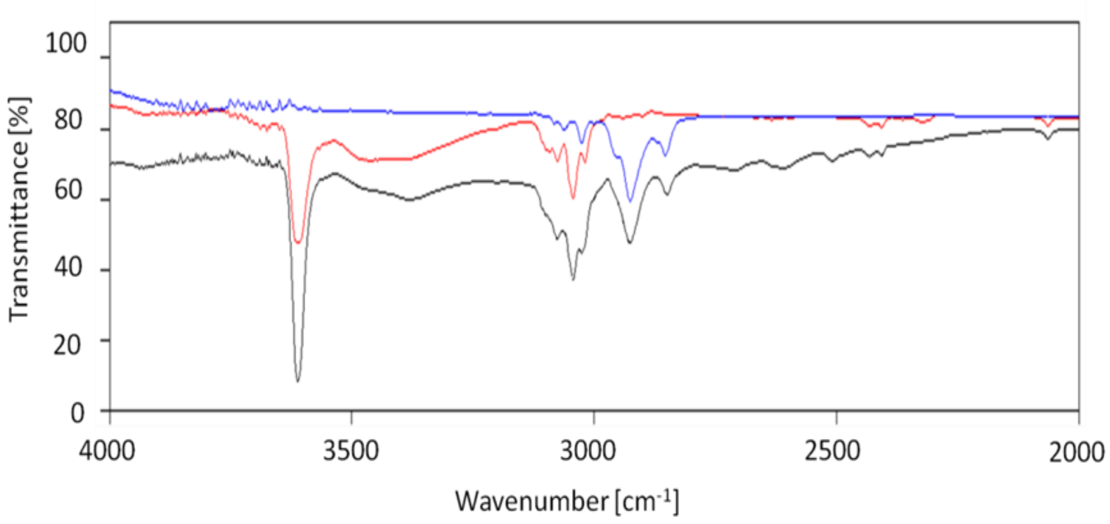

Figure 3.6: Single component 2 wt% 4VP-2 colloids (blue) and 0.25 wt% phenol (red) in CCl_4. The black line is showing the 1 : 1 mixture of both components in CCl_4.

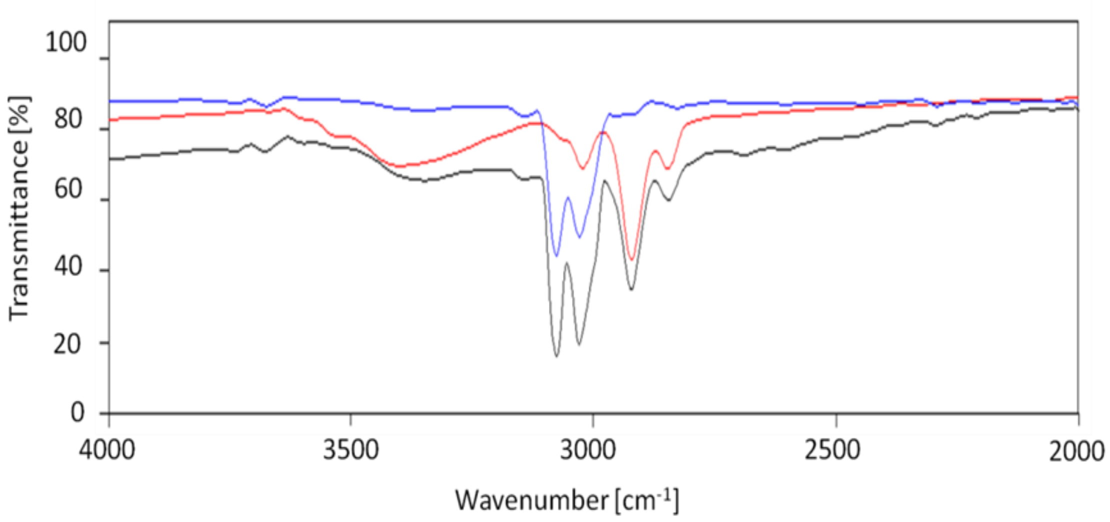

Figure 3.7: Single componet 2 wt% 4OH-1 colloids (red) and 0.25 wt% pyridine (blue) in CCl_4. The black line is showing the 1 : 1 mixture of both components in CCl_4.

In order to identify an aggregate stoichiometry in these binary aggregates, precipitation experiments were carried out at variable composition of the binary colloidal mixture in $CHCl_3$. To this end the filtrated serum was analyzed after precipitation by SLS at variable volume ratios of the initial mixed solutions. While the concentration of the large 4OH-2 colloids was kept constant the concentration of the small 4VP-3 colloids used as variable to set the certain number ratios. The respective serum solutions were revealed by filtration of the suspensions immediately after precipitation of the hetero-aggregates. The 3D graph in Figure 3.8 shows an abrupt change of the resulting scattering curves around the colloid volume ratio of 4OH-2 to 4VP-3 of 2 : 1 corresponding to a colloid number ratio of ~ 1 : 2. This change turned the scattering curve from a form factor close to the pure 4OH-2 to the one close to the pure 4VP-3. Distinction became possible as the pure colloids still show form factors which are distinguishable enough despite the relative large size ratio in $CHCl_3$ of $\gamma_{Rh(4OH-2)\,/\,Rh(4VP-3)} = 0.71$.

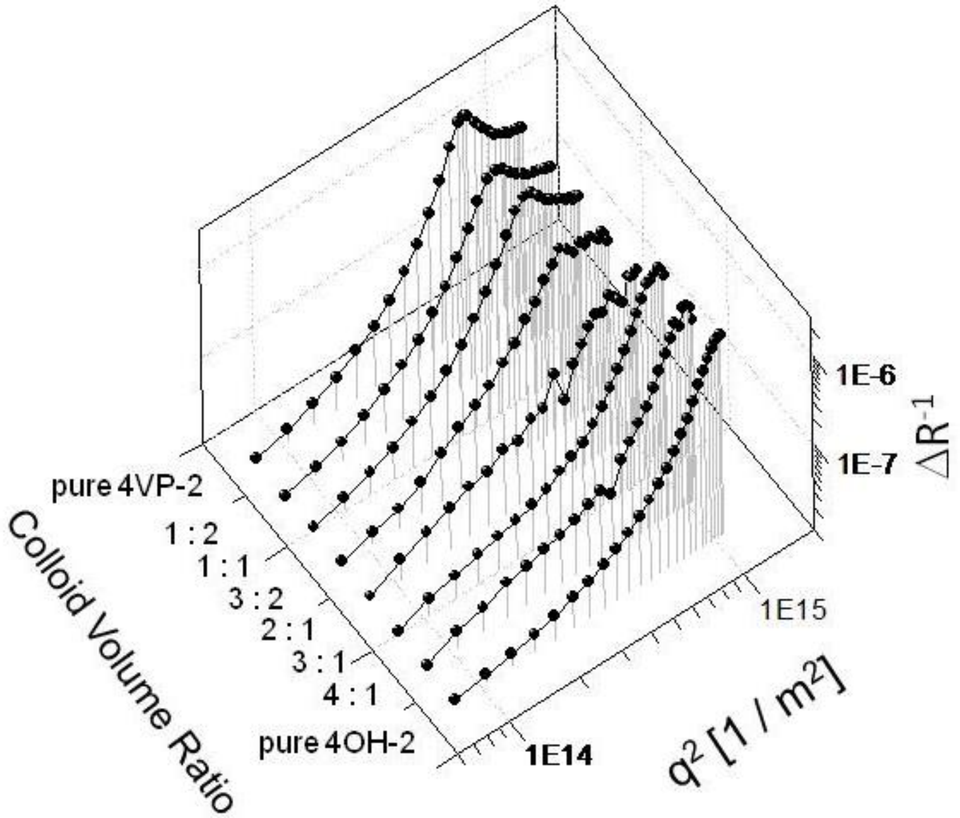

Figure 3.8: Light scattering analysis of the filtrated solutions of 4VP-3 colloids combined with 4OH-2 colloids in $CHCl_3$ after precipitation at variable composition in the original mixture. The 3D graph shows an abrupt change of the scattering curve close to the ratio of 4OH-2 / 4VP-2 = 2 : 1.

Colloid combinations with a larger size difference of the components showed more pronounced differences between the component form factors but indicated a transition over a broader range of volume ratios leaving us with a much less well defined stoichiometry. The results are summarized in the 3D graph in Figure 3.9. Obviously it needs an excess volume of smaller colloids to compensate one large colloid. It has to be mentioned here again that the aggregation process is quite fast. A correct stoichiometry could not be reached then.

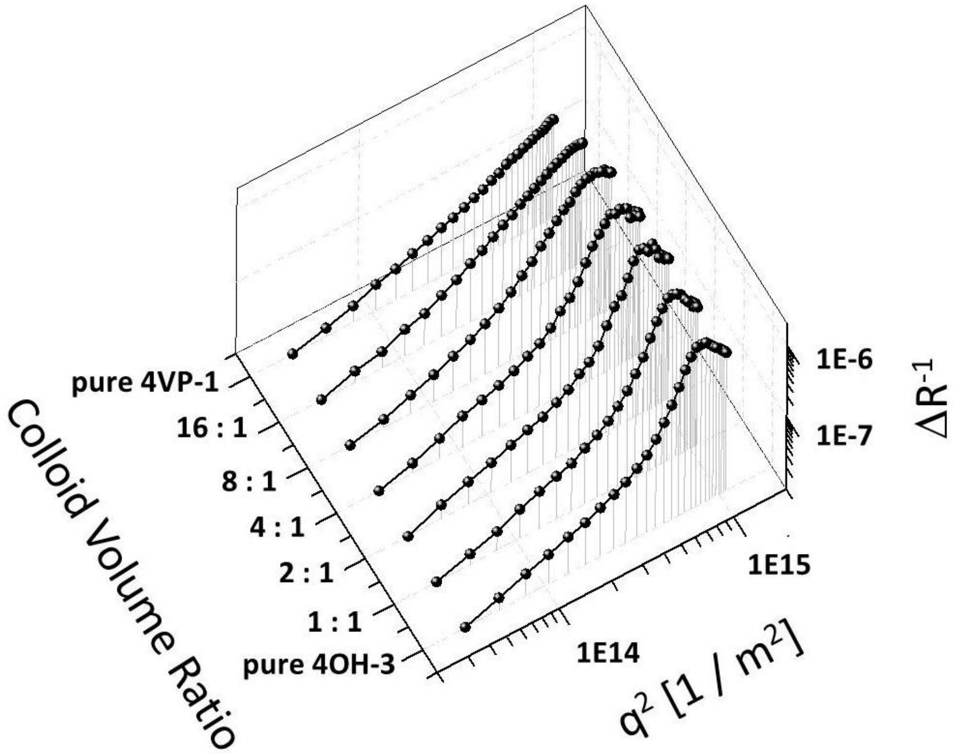

Figure 3.9: Light scattering analysis of the filtrated solutions of 4VP-2 colloids combined with 4OH-3 colloids in $CHCl_3$ after precipitation at variable composition in the original mixture. The 3D graph shows a slow change of the scattering curve over a broad colloid volume ratio range.

3.3 Time resolved experiments and aggregation kinetics

The strong aggregation discussed in the preceding paragraphs is expected to slow down in highly dilute solution. This offers the opportunity to analyze the aggregation kinetics as function of particle concentration and particle composition by means of time resolved static light scattering. Such experiments have been performed with the colloid combination 4OH-3 with 4VP-2. With its hydrodynamic colloid size ratio of ~ 0.5 in $CHCl_3$ this combination is expected to fit into an AB_2 lattice. Figure 3.10 shows a TR-SLS measurement and associated SEM images at an overall colloid concentration of 50 mg / L and a colloid volume ratio of 4OH-3 to 4VP-2 = 5 : 1. This experimental condition turned out to be the most suitable one for TR-SLS experiments. After a short induction period an aggregation is observed. The radius of gyration increases from 193 nm approaching a plateau at 243 nm. This is an increase of 50 nm. In line with the increase of R_g an increase of $\Delta R_{\theta=0}$ has been recorded. The latter parameter is a measure of the weight averaged particle mass. SEM images were successively recorded with colloids from the same solution used for TR-SLS. The images show that the larger 4OH-colloids are picking up small 4VP-colloids thus forming a shell. In the enlarged SEM image of the same experiment one can see a large single colloid with an incomplete shell of small colloids. If a closely packed shell is assumed around the larger particles a radius of gyration not larger than 290 nm can be expected. This value simply results by summing up both hydrodynamic radii according to $R_g = (R_h$ (4VP-2) + R_h (4OH-3) $\cdot$ 0.778. However, the spheres in a monolayer have a lower density even if they form a shell in close contact to each other.

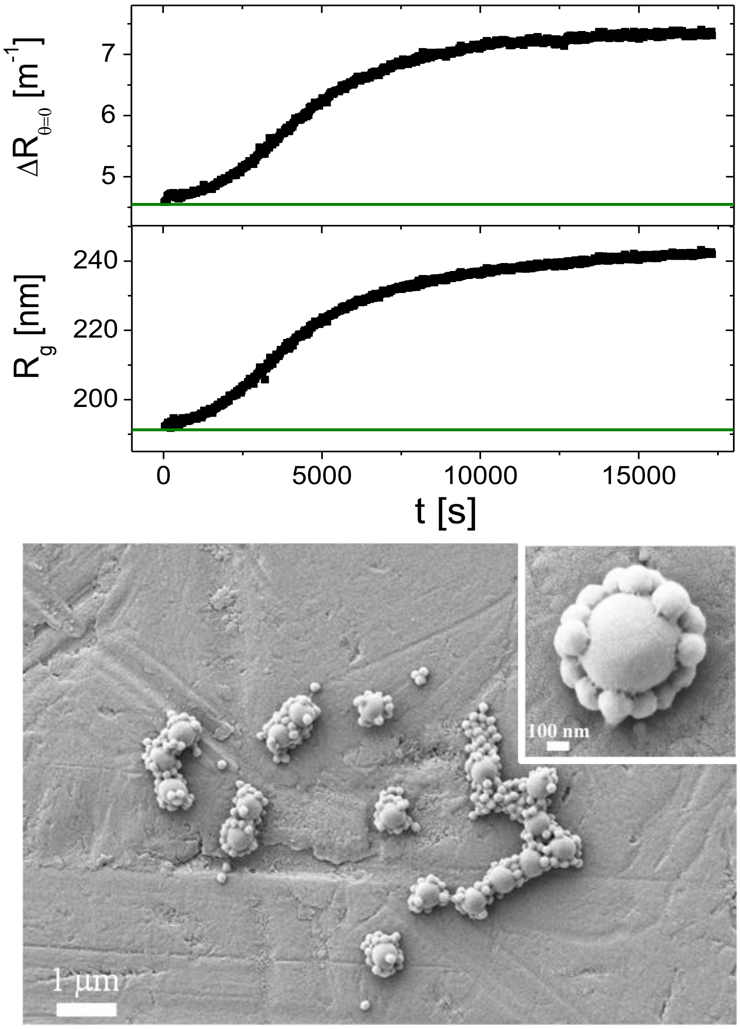

Figure 3.10: TR-SLS experiment with a mixture of 4OH-3 colloids (R_g = 209 nm) and 4VP-2 colloids (R_g = 81 nm) with a colloid volume ratio of 5 : 1 in $CHCl_3$ (top). SEM pictures of aggregates formed after $CHCl_3$ evaporation. The same solution has been used for both experiments. The overall concentration was ~ 50 mg/L.

Further TR - SLS measurements with a smaller colloid volume ratio of 4OH-3 / 4VP-2 = 2 : 1 corresponding to a higher concentration of the small 4VP-2 colloids give the same R_g of approximately 240 nm (Figure 3.11). Experiments with a higher colloid volume ratio of 4OH-3 / 4VP-2 = 8 : 1 corresponding to a lower concentration of the small 4VP-2 colloids yield a R_g of 215 nm (Figure 3.11). The corresponding increase in size of ~ 20 nm is considerably smaller than the 50 nm increase observed at the volume ratios of 2 : 1 and 5 : 1. Obviously there is a maximum surface coverage of the small colloids on the large colloid. Apparently the shell remains incomplete once the fraction of the smaller 4VP-2 colloids in the mixed solutions drops below a certain value. Due to movement and steric repulsion among the same functionalized small colloids on the surface of the large colloids it is not possible to exceed a distingue particle surface occupation.

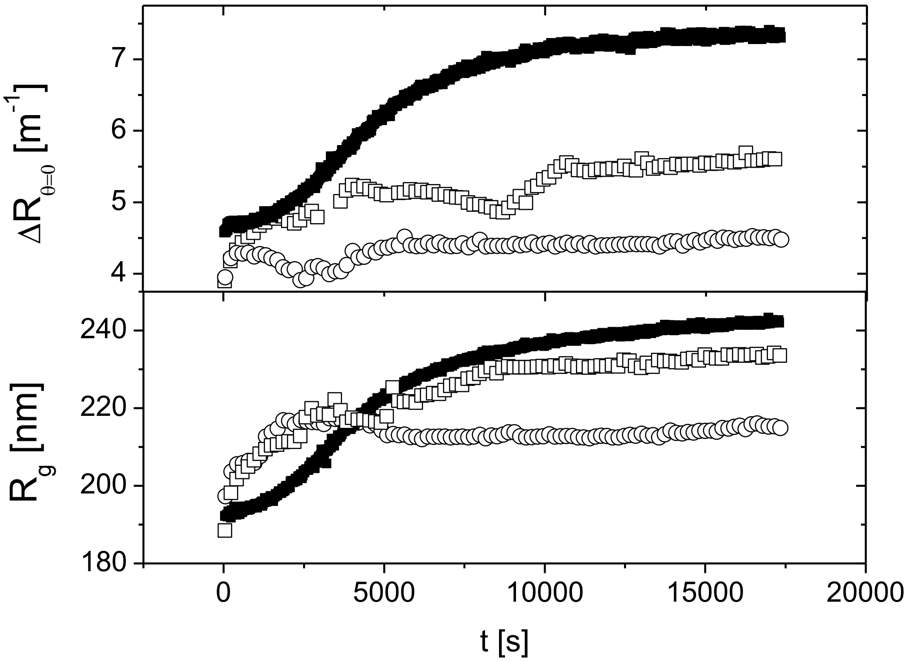

Figure 3.11: TR-SLS experiments with a mixture of 4OH-3 colloids (Rg = 209 nm) and 4VP-2 colloids (Rg = 81 nm) in $CHCl_3$ with a colloid ratio of 4OH-3 volume to 4VP-2 volume of 8 : 1 (○), 5 : 1 (■) and 2 : 1 (□). The volume ratio was varied at constant concentration of 4OH-3 colloids and the overall colloid concentration was ~ 50 mg/L.

It has to be stressed at this point that the R_g values established are fitted according to a simple Guinier approximation. Easily calculated, a monodisperse sphere with R_g = 250 nm generates an error of 20 % in R_g if evaluated with a linear Gunier fit in a regime of $1.6 < qR_g < 2.8$. Although this error decreases drastically with polydispersity and with smaller R_g it is not the only source of error to be considered here. With increasing colloid size the Rayleigh scattering pattern [76] is gradually transforming into a Mie pattern [77]. For polystyrene latex particles in H_2O with $R_h = 290$ nm Borkovec et al [73] determined this inaccuracy in R_g with 3 % as negligible. However, these two sources of error modify Guinier values for both colloidal mixtures toward the same direction and the difference in geometric growth (50 nm compared to 20 nm for the two mixtures respectively) can be considered as significant.

As expected, a decrease in the overall colloid concentration from 50 to 25 mg/L decreases the aggregation rate drastically.

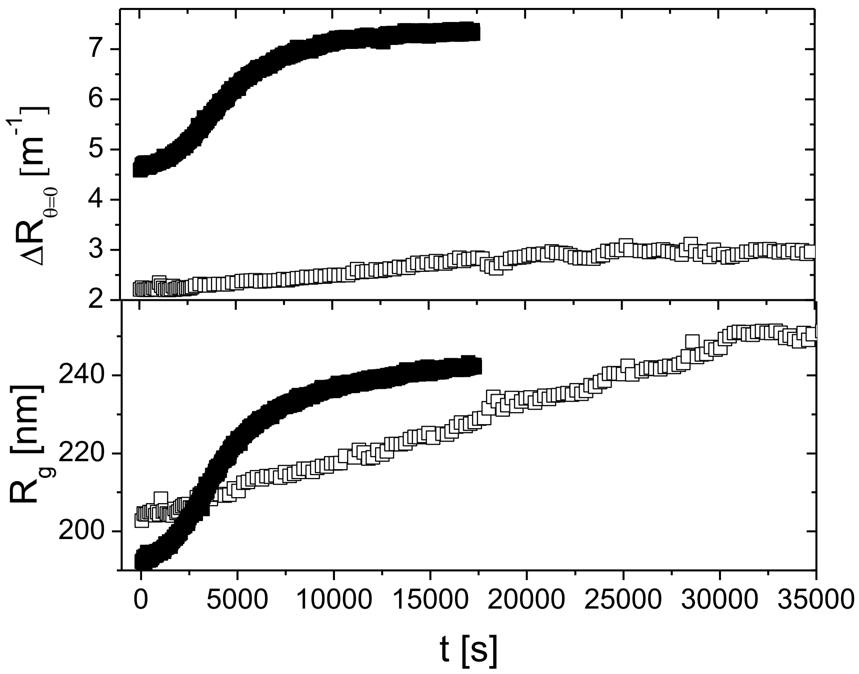

Figure 3.12: TR-SLS experiments with a mixture of 4OH-3 colloids (Rg = 209 nm) and 4VP-2 colloids (Rg = 81 nm) with a colloid volume ratio of 5 : 1 in $CHCl_3$. The overall colloid concentration is ~ 25 mg/L (□) and ~ 50 mg/L (■).

Since the colloids under present consideration were prepared according to the SFEP, they include a few ionic groups stemming from the initiator. In addition the 4VP- and 4OH-comonomers have polar residues and are thus capable of adsorbing ions. Hence the colloids are expected to bear some electric charges. In principle, the interference pattern among 4VP- and 4OH-colloids based on complementary H-bonds motifs maybe superimposed by electrostatic interactions. To scrutinize any significant influence of charge interactions on the hetero-aggregation the zeta potentials of the colloids 4VP-2 and 4OH-3 have been measured. Experimental details can be found in Chapter 6.6.

With z(4VP-1) = + 26.7 mV and z(4OH-3) = + 27.6 mV the obtained zeta potentials in $CHCl_3$ have the same sign. This result excludes hetero-interactions based on oppositely charged colloids. In addition to this fact aggregation experiments were also performed in $CHCl_3$ saturated with 20 mmol/l NaCl to screen electrostatic forces from the possible charges. At high colloid concentration the same aggregation was observed as outlined in Figure 3.5 for the case of pure $CHCl_3$. At low colloid concentration the aggregation pattern outlined in Figure 3.10 for pure $CHCl_3$ could be reproduced also in $CHCl_3$ saturated with NaCl in Figure 3.13. Since the addition of a screening salt does not affect hetero-aggregation its origin cannot be caused by electric charges.

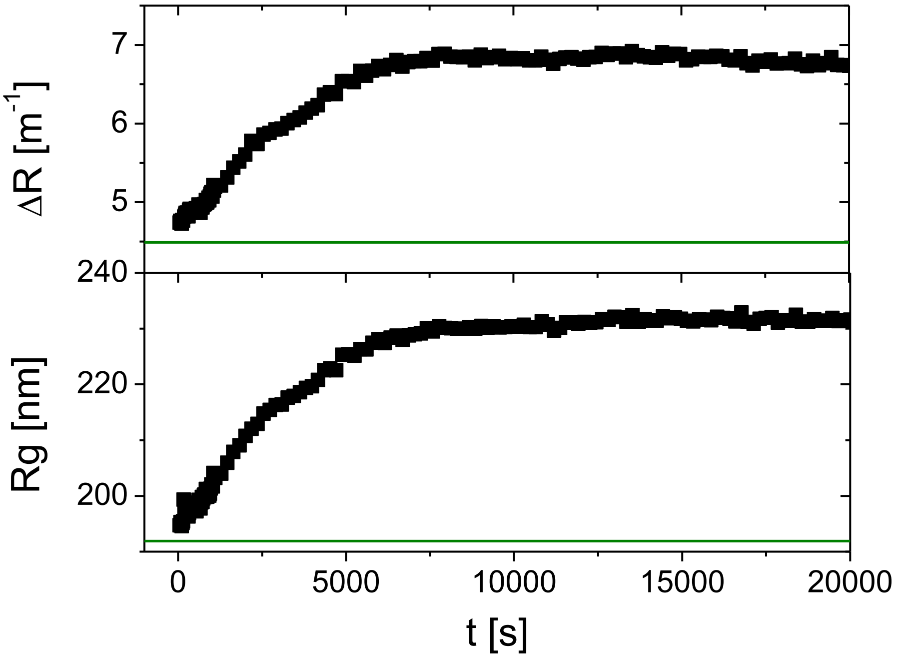

Figure 3.13: TR-SLS experiment with a mixture of 4OH-3 colloids (R_g = 209 nm) and 4VP-2 colloids (R_g = 81 nm) with a colloid volume ratio of 5 : 1 in *$CHCl_3$ saturated with NaCl* (~ 1.2 g/L). The overall colloid concentration is ~ 50 mg/L.

Additionally in a reference experiment, shown in 3.14, a combination of the sample 4OH-3 as large component and the sample 4OH-1 as small component is chosen. Now both components have the same functionalizations at a size ratio which is comparable to the one applied for the hetero-aggregation experiment just outlined. Contrary to the SEM image from the hetero-aggregation experiment in Figure 3.10, the SEM image of this reference experiment shows the small colloids randomly dispersed without any preferential adsorption to the larger colloids. In line with this the TR-SLS measurements do not indicate any increase in R_g and $\Delta R_{\theta=0}$. As a consequence the reference experiment is considered to be the final prove for the H-bonds to be the origin for hetero-aggregation in our binary 4VP - 4OH colloid system.

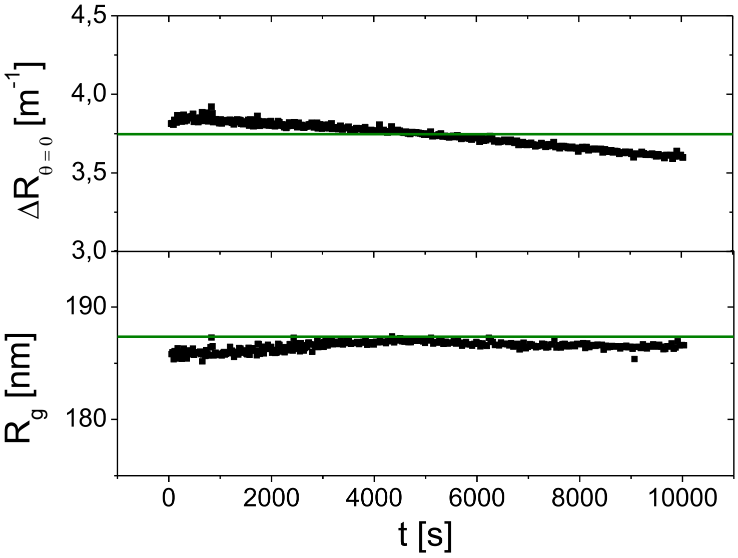

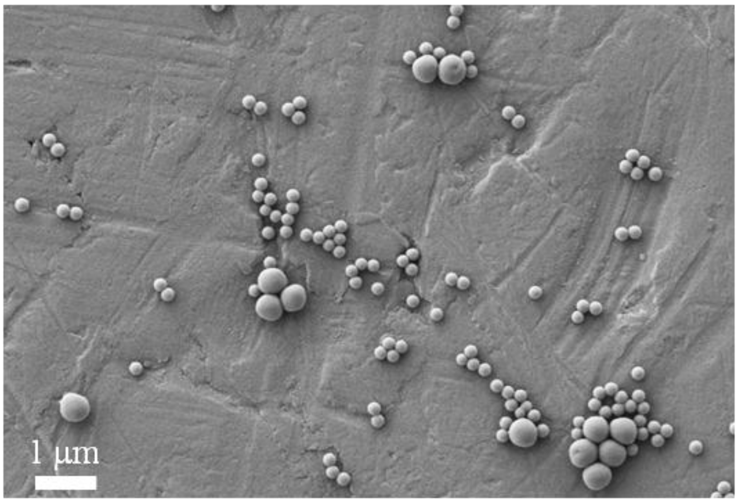

Figure 3.14: TR-SLS reference experiment with a mixture of 4OH-3 colloids (R_g = 209 nm) and 4OH-1 colloids (R_g = 75 nm) with a colloid volume ratio of 5 : 1 in $CHCl_3$. The overall concentration is ~ 50 mg/L. Constancy of $\Delta R_{\theta=0}$ and R_g exclude any aggregation. The SEM picture of the dried solution does not indicate any specific interactions among the colloids from the two samples. Compare with Figure 3.10.

3.4 First controlled crystallization experiments

As mentioned before, the aggregation process in highly concentrated colloid mixtures is too fast to lead to a well ordered super-lattice. Phenol is expected to act as a capping agent for the 4VP donor groups on the 4VP-2 colloids. To analyze the effect of such a capping agent on the aggregation a concentration series of phenol in a 4VP-2 colloid solution in $CHCl_3$ with a fixed colloid concentration has been prepared. To each of these solutions a fixed amount of 4OH-3 colloid solution was added. The total concentration including both colloids amounted to 1.25 wt% corresponding to a colloid number ratio of roughly 1 : 1. This series of mixing experiments at variable content of capping agent indicates a relatively sharp aggregation threshold. At the present experimental conditions this threshold for hetero-aggregation appears between 1.15 M and 1.25 M phenol. Hence aggregation can be inhibited if the capping agent phenol is added to concentrated solutions of binary colloids. This crucial point facilitates the possibility to control the aggregation with a capping agent.

First SEM studies of a dried stable binary solution of 4VP-2 and 4OH-3 on a glass substrate at a number ratio of 1 : 1 with the 4VP-colloids capped at a phenol concentration of 1.25 M, showed the first appearance of an ordered assembly in a NaCl cubic arrangement (Figure 3.15). The weakening of the H-bonds due to the capping of the 4VP-2 colloid gives the particles more time to order during the approach.

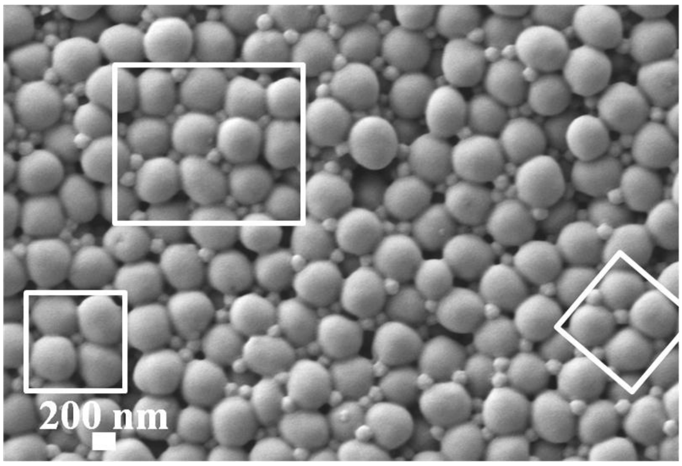

Figure 3.15: SEM picture of the colloid mixture 4OH-3 and 4VP-2 (1 : 1) generated from concentrated solution (1.25 wt%) after gentle evaporation of solvent. The 4-VP2 component solution has been treated with phenol as capping agent. First appearance of an ordered assembly in a NaCl cubic arrangement is demonstrated.

Following a similar strategy as the crystallization experiment shown in Figure 3.15 a reference experiment has been designed. At this time the combination of the same functionalized colloids 4OH-1 and 4OH-4 with γ_{dried} = 0.25 in highly concentrated solution gives an amazing result after slow solvent evaporation (Figure 3.16). The SEM imaging displays strong phase separation behavior (see Chapter 1.5.3) of the used colloids. This is again a clear cut difference to complementary H-bond functionalized binary colloids combined in a mixture.

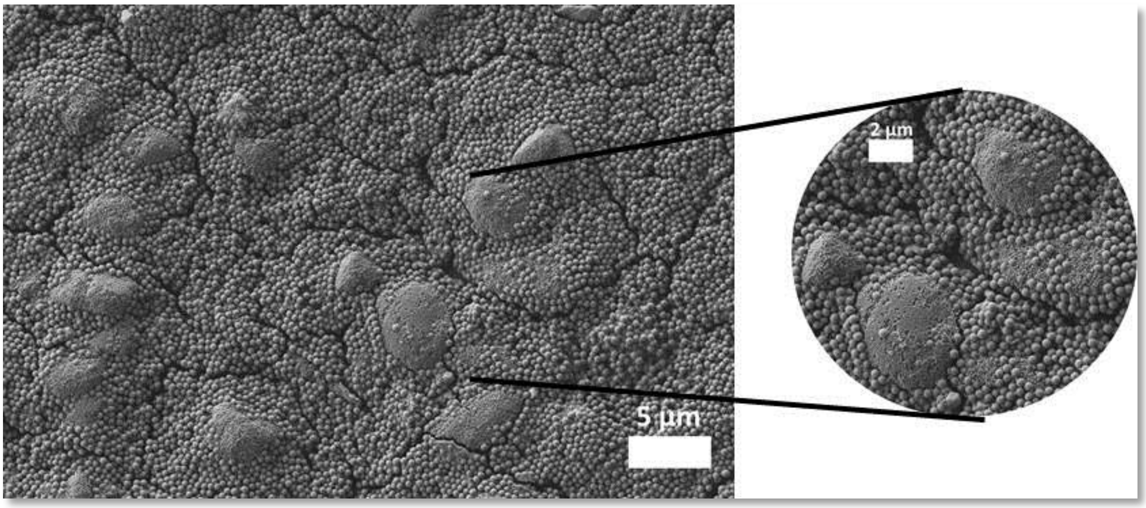

Figure 3.16: Binary mixture of colloidal particles. The large colloids have a radius in the dried state of 400nm and the small particles have a radius of 100nm with a narrow particle size distribution for each. Both types of colloids are prepared from the same material (colloids 4OH-1 and 4OH-4). Hence, they do not show any specific long range repulsive or attractive interaction. They show strong depletion behavior. Phase separation appears during slow solvent evaporation (70 wt% Toluene : 30 wt% $CHCl_3$).

3.5 Conclusion

A new system of two complementary colloids, both based on crosslinked polystyrene is presented. The complementary nature of mutual interactions is accomplished by means of the incorporation of H-bond donors on one colloidal component and H-bond acceptor on the other component. Phenol residues in 4-hydroxy styrene comonomers act as H-bond donors and 4-vinyl pyridine as the alternative comonomer serves as the corresponding H-bond acceptors. The colloidal components form H-bonds according to their specific comonomers, thereby leading to a selective hetero-interaction among the components in the dried state. As an important feature, the colloidal components also form H-bonds with the respective complementary molecular residues in $CHCl_3$ as the solvent.

The complementary functionalization of the colloidal components with H-bonding residues leads to a significant and selective interaction between the two colloidal components, which could be proven by the occurrence of hetero-aggregation. Thus the extent of this hetero-aggregation could be controlled by the volume ratio of the two components, by the concentration of the colloidal mixture and by the addition of either low molecular weight H-bond functionality. It is expected, that the extent of interaction as well as the stoichiometry of the hetero-aggregate will also depend on the size ratio of the two colloidal components. Proof of these hetero-interactions was performed by joint IR-spectrometry, light scattering and SEM imaging. Most of the present experiments were performed at a size ratio of R_h (4VP-1)/R_h (4OH-3) = 0.52 this size ratio is expected to provide promising conditions for the generation of binary super-lattices, and more explicitly, to provide a binary lattice with a NaCl design.

In the high concentration regime (~ 3 wt%) of binary colloidal suspensions in $CHCl_3$, hetero-aggregation causes solid formation, preferably at a specific stoichiometry of 2 : 1 for the colloid combination 4OH-2 / 4VP-2 $\gamma_{(CHCl_3)} = 0.71$. Noteworthy, the solid material is floating. If the overall concentration is appropriately lowered, hetero-aggregation could be followed by means of time resolved static light scattering. In a suitable reference experiment performed with two binary 4OH-colloids having a size ratio of $\gamma_{(CHCl_3)} = R_S/R_L = 0.38$, no sign of hetero-interaction could be revealed.

Finally, it is an advantage that the functionalized colloidal components are able to also form H-bonds with the respective complementary low molecular weight counterpart. While varying the concentration of phenol in a binary colloidal mixture of 4OH- and 4VP-colloids, hetero-aggregation of the two complementary colloidal components could be suppressed at a certain critical phenol concentration. Based on these findings, we equilibrated colloidal mixtures at a number ratio of one 4OH-particle per 4VP-particle with a phenol content close to this critical concentration threshold and generated films via gentle evaporation of the solvent. SEM images of the resulting deposits indicated the onset of binary lattice formation. Additionally to that, the combination of similar functionalized colloids in high concentration and slow evaporation of the solvent leads to phase separation. These results are proving the necessity of the complementary H-bond motifs for the present hetero-aggregation. These promising results give raise to the hope, that controlled hetero-aggregation with complementary donor and acceptor colloids will offer new ways to complex materials and to binary super-lattices. Consequently, more controlled crystallization experiments are performed, which are presented in the in the following Chapter 4.

4. Crystallization experiments

In the following several series of controlled crystallization experiments shall be described. The system is studied at variable overall colloid concentration, colloid size ratio and colloid number ratio. A mixture of 70wt% toluene and 30wt% chloroform serves as solvent. Also the substrate is varied in order to improve the surface quality.

4.1 The solvent system

In the previous section we used pure chloroform. Chloroform is an aprotic, polar and good solvent for both types of colloids, the vinyl pyridine and the phenol functionalized colloids. It shows no characteristic bands in the relevant IR wavenumber range but more strikingly it is not able to interfere with emerging hydrogen bonds. A disadvantage of chloroform for the present work however is the high density of 1.48 g/cm^{-1}. Our colloids are based on polystyrene. Hence, a density of ~1.10 g/cm^{-1} can be assumed. As a consequence (Figure 3.5) the aggregates are floating. This makes controlled crystallization experiments more difficult. Hence all experiments described in the present chapter were performed in a mixture of 70wt% toluene (ρ = 0.87 g/cm^{-1}) and 30wt% chloroform. This mixture shows a density of 0.99 g/cm^{-1}. Therefore, the colloids settle slowly under normal conditions. Additionally the refractive index of the new solvent system (toluene: n_D^{20} = 1.496, chloroform: n_D^{20} = 1.445) is closer to the refractive index of our colloids which is 1.58. A better refractive index matching is expected to reduce possible attractive forces among the colloids due to induced fluctuating dipoles in the electron clouds. This is crucial as the van der Waals forces would considerably interfere with the H-bond interactions.

In order to determine the sizes for the colloids, which are used in the following crystallization experiments, light scattering measurement of the respective systems have been done. The sizes of the colloids in 70wt% toluene and 30wt% chloroform can be found in Chapter 3, Table 3.1.

4.2 General conditions

All mixtures with 0.33wt% total colloid concentration (if not stated otherwise) were stabilized with appropriate amounts of phenol to avoid aggregation of the binary colloid mixtures completely for at least 24h. Colloids should be driven towards a tilted substrate by slow evaporation of the solvent and hence emerging capillary forces among the particles. This was already discussed in detail in Chapter 1.6. Details to the evaporation procedure are outlined in Chapter 4.3. The pressure in a vacuum oven during the solvent evaporation was lowered to 500mbar. The temperature was set to 35°C. The slightly elevated temperature assists the Brownian motion which decreases a possible settling of colloids faster than the solvent evaporation. It is important that the colloids are moved to the meniscus by convective forces, whereby they are coerced by capillary forces to self-assemble into a colloidal crystal film. In order to further promote H-bond formation as the one represented in Figure 3.15 phenol was removed successively at a slightly elevated temperature of 40 °C and a strongly reduced pressure of ~ 10^{-2} mbar for 24 h.

4.3 The substrate

As shown in the previous Chapter 3.4 a first appearance of an ordered assembly was accomplished on a cleaned, untreated glass substrate. Figure 3.15 illustrates this appearance from a binary mixture of large to small colloids in a 1 : 1 solution with an overall concentration 1.25wt%. When crystalizing from less concentrated solutions, e.g. 0.20wt% glass turned out to be not a suitable substrate. Despite a smooth surface, glass carries a lot of surface hydroxyl functionalizations after treatment with PIRANHA solution (75 % concentrated sulfuric acid (conc.) plus 25% hydrogen peroxide solution (30%)). The resulting functionalizations interact strongly with the small vinyl pyridine functionalized particles and cause an enrichment of the small particles at the glass substrate as can be seen in Figure 4.1. Hence, it is hardly possible to set correctly the desired colloid number ratio. A similar behavior was observed on glimmer. Glimmer also bears surface hydroxyl functions and similar behavior like on glass was clearly seen in SEM pictures (not shown here). The vinyl pyridine functionalized colloids were mainly arranged on the substrate surface. This makes it unfeasible for further experiments.

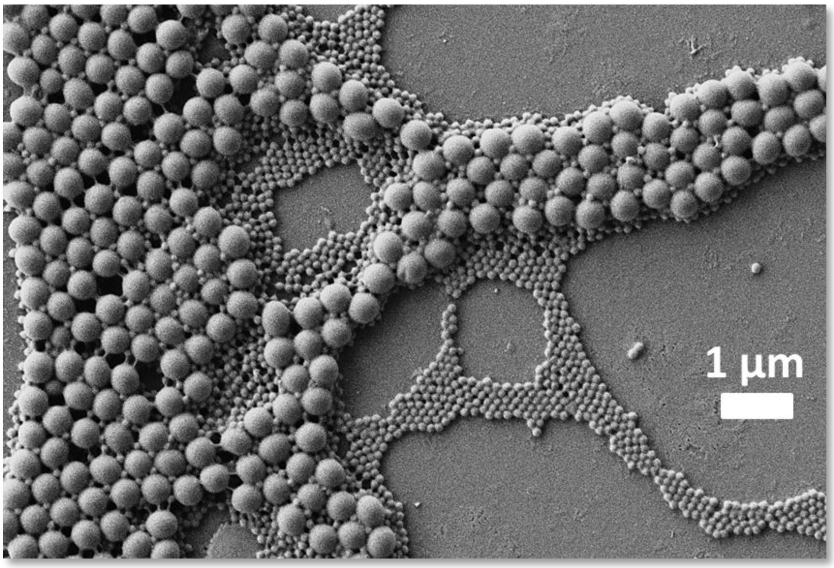

Figure 4.1: SEM image of a 1 : 1 mixture of 4VP-1 (R_h = 102 nm) and 4OH-4 (R_h = 260 nm) colloids on a cleaned and hydrophilic glass substrate treated with a piranha solution. The separation of the small 4VP-1 colloids due to hydrogen bond interaction with hydroxyl groups on the glass surface is clearly seen.

Better results were achieved on a clean silicon wafer. A homogeneous mixture of the small 4-vinylpyridine functionalized colloids and 4-hydroxyl functionalized colloids including small ordered hexagonal patterns could be identified. See Figure 4.2. It seems to be recommendable to deal with smooth and plane substrates that do not show any preferential attraction to either colloidal species.

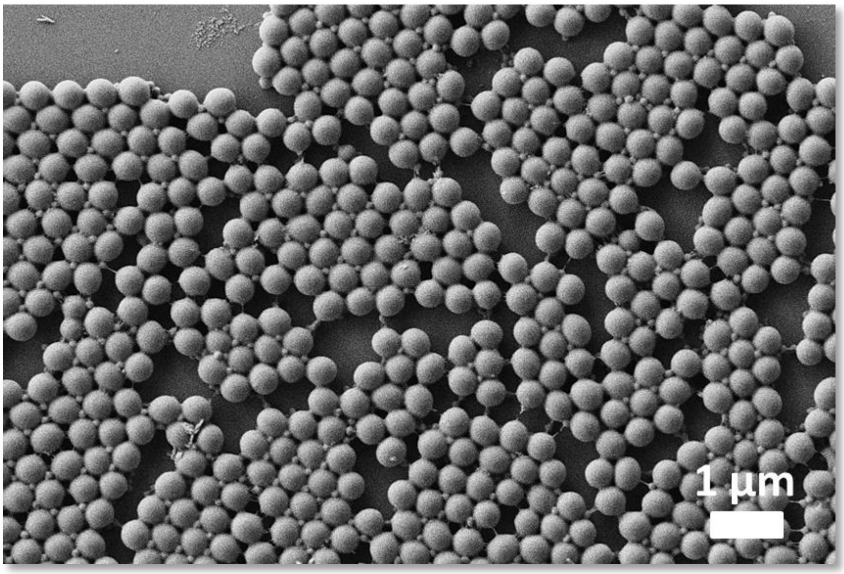

Figure 4.2: SEM image of a 1 : 1 mixture of 4VP-1 (R_h = 102 nm) and 4OH-4 (R_h = 260 nm) on a clean silicon wafer.

Unfortunately, the use of silicon wafers turned out to be also problematic. It is not possible to set the similar geometric conditions for every experiment. Cleaned aluminium SEM stubs as substrate brought as good or even better results as the silicon wafers. For a detailed analysis of the impact of the colloid number ratio and the colloid size ratio on the crystal quality, it is necessary to set the geometrical set-up of the substrate as accurately as possible for every single crystallization experiment. The SEM stub makes it easy to reproduce the same geometric conditions in every vial (Figure 4.3). Henceforth, all experiments are performed on stubs. The lower end of the aluminium stub was grinded flat to avoid rolling. This facilitates analysis of the deposited colloid film in dependency of evaporation. The overall concentration is changing during the evaporation process. This leads to fluctuations in the deposited film thickness and with it to possible variations in the lattice formation of the ordered colloids. Hence, it is useful to know in which direction the meniscus is retreating.

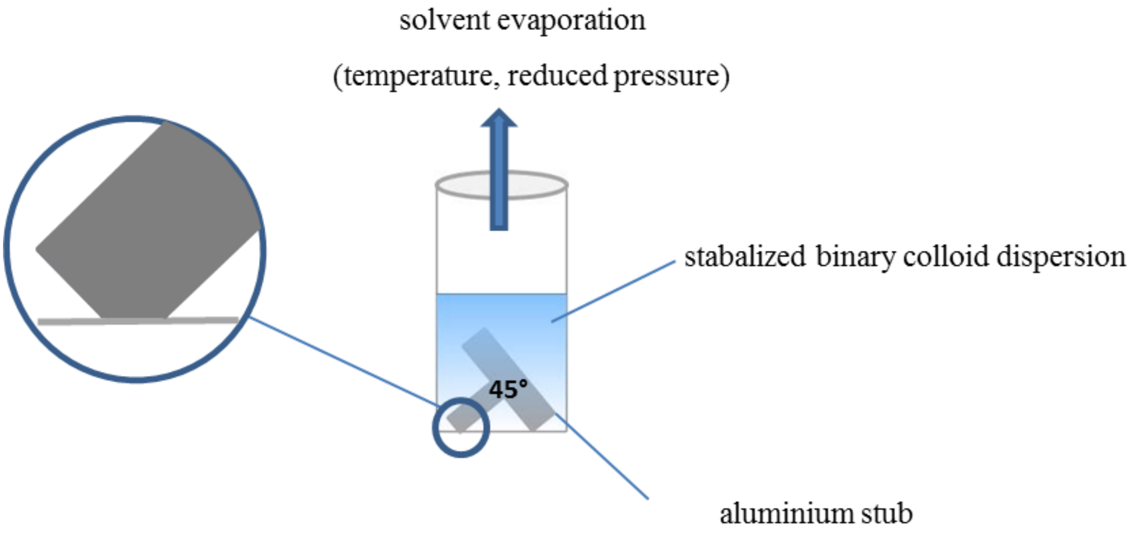

Figure 4.3: Design of the evaporation procedure including geometric details of the positioning of the aluminium stub..

In Figure 4.4 one can see two layers of large 4OH-colloids with hexagonal arrangement. Several of the interstitial vacancies are occupied with 4VP-colloids to give a hexagonal AlB_2 (from aluminium bromide alloys) lattice. This is a clear improvement compared to the experiments before.

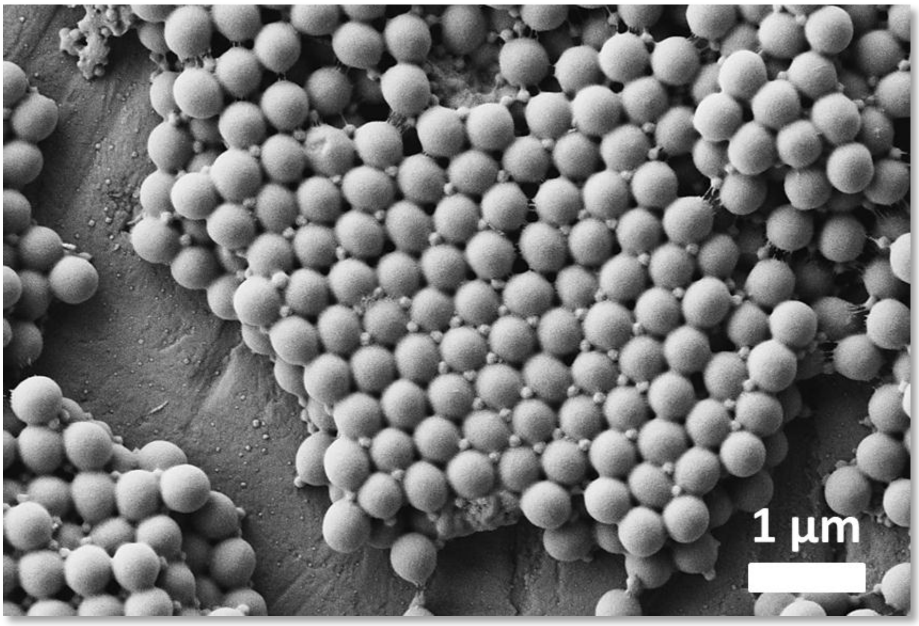

Figure 4.4: SEM image of a 1 : 1 mixture of 4VP-1 (R_h = 102 nm) and 4OH-4 (R_h = 260 nm) on an untreated SEM aluminum stub.

Nevertheless the rough and uneven surface of the untreated aluminum stub is clearly visible. In a next step the surface was smoothened by polishing. To this end the stubs were treated 2 minutes on a turning polishing plate with a very fine abrasive paper with a grid of 4000 followed by a 2 minutes treatment with 1µm diamond slurry on a wetted polishing pad. At the end of the polishing step the stubs were fixed to give a preferential orientation to the polishing rills. Afterwards the orientation of the polishing rills was chosen to be perpendicular to the evaporation front during the crystallization.

As can be seen in Figure 4.5 this polishing treatments lead to a significantly improved lattice formation. The large 4OH-4 colloids orientate with the polishing rills to form large hexagonal structures in AlB_2 conformation. Consequently all experiments outlined in Chapters 4.4, 4.5 and 4.6 are carried out on polished aluminium stubs.

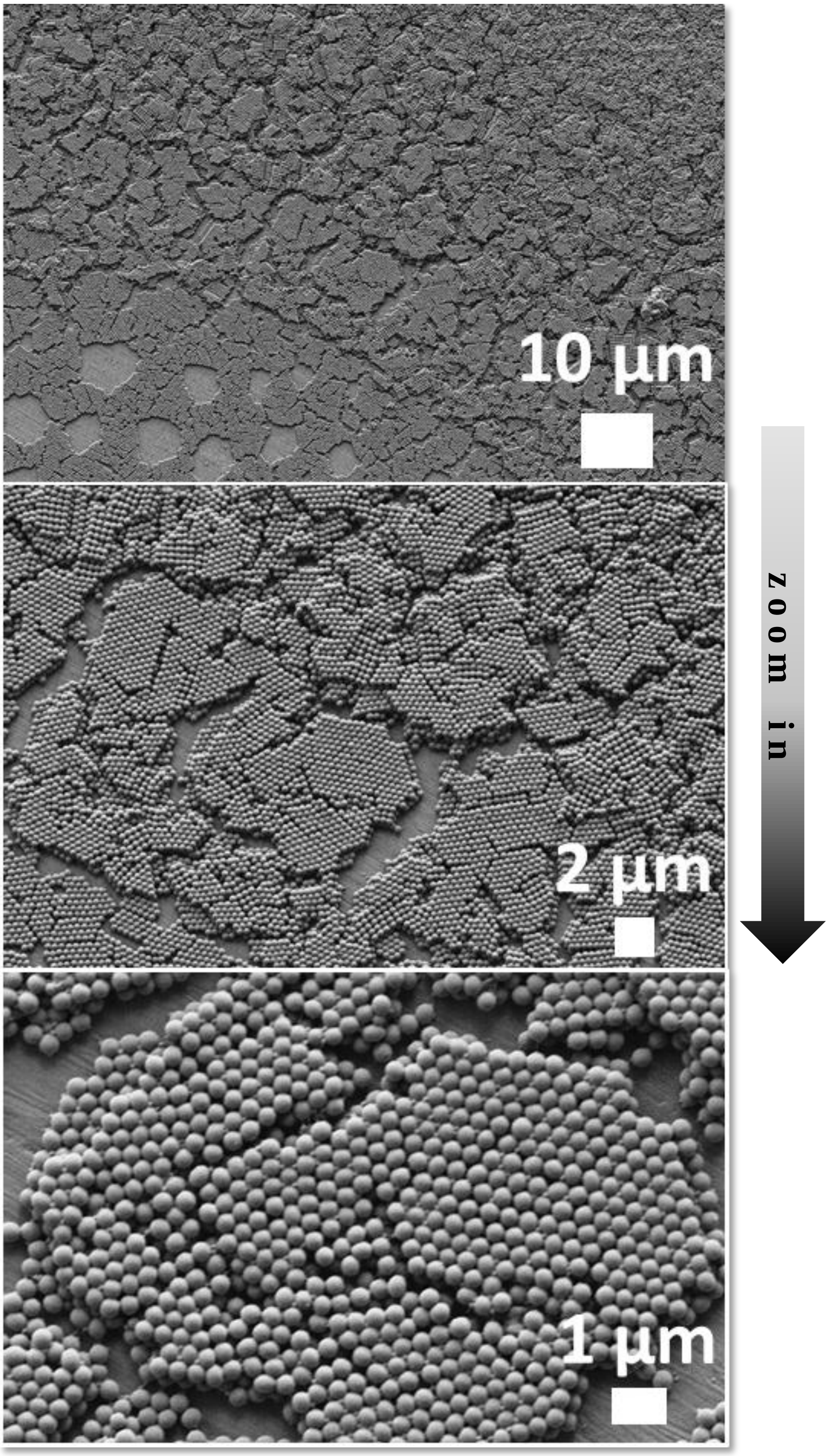

Figure 4.5: SEM images of a 1 : 1 mixture of 4VP-1 (R_h = 102 nm) and 4OH-4 (R_h = 260 nm) on a polished SEM aluminum stub. Large hexagonal areas are formed with an orientation of the large 4OH-4 colloids. The polishing rills can clearly be seen.

4.4 The overall concentration

Most likely the crystallization is harder to be controlled the higher the concentration gets. If the colloid concentration is increased an increased number of collision events among the complementary colloids occur. Collisions can cause the assembly of unsystematic and non-ordered colloidal agglomerates. During the solvent evaporation agglomerates cause defects in the crystal structure. Those defects can propagate and accumulate with growing crystal thickness resulting in non-ordered structures. In the following, crystallization experiments from highly dilute solution with two different overall concentrations were performed. One concentration was 0.33 wt% and one more, 1 wt%, three times higher. In the first case three layers of the large 4OH-4 colloids were built at most. Large ordered structures with AlB_2 conformations can be proven. The higher the thicknesses of the colloid film gets the less ordered the structure appears. In addition drying cracks show up making the formation of super-structures impossible. In Figure 4.6 the effect of a threefold concentration can be seen.

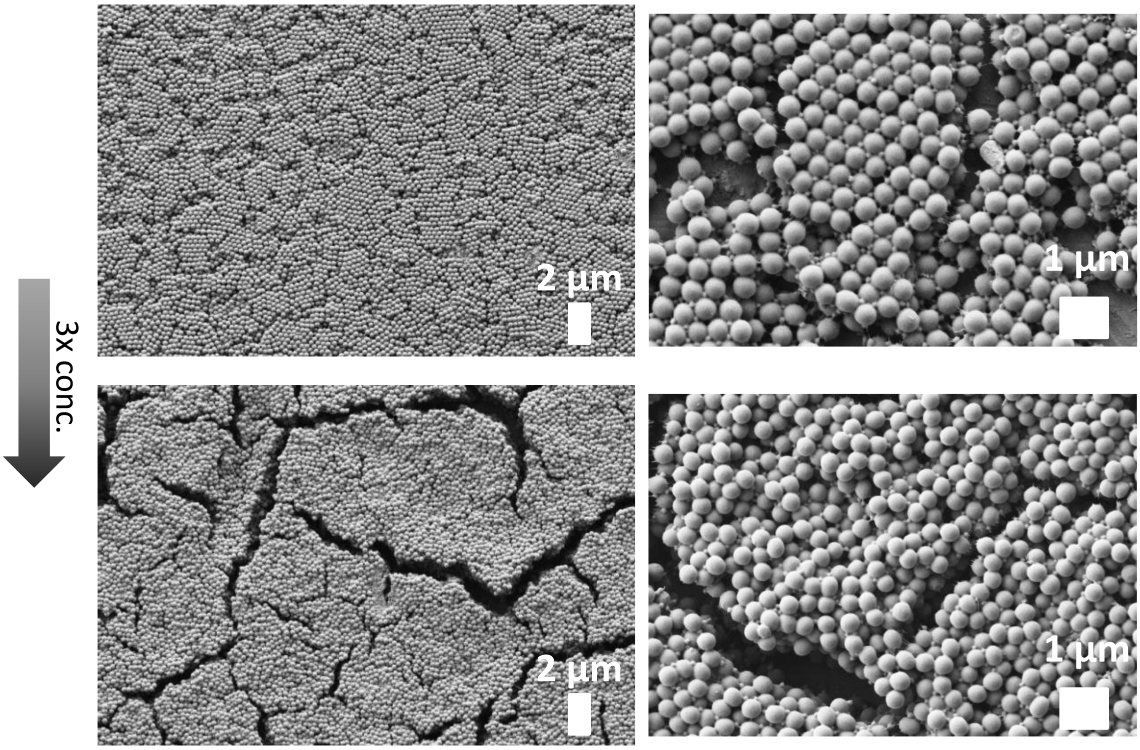

Figure 4.6: Effect of increasing concentration on the crystal formation of the same colloid system. On top (left) a 1 : 1 mixture of 4VP-1 (R_h = 102 nm) and 4OH-4 (R_h = 260 nm) on a polished aluminum stub shows ordered patterns over a broad area. At the bottom the same mixture in a three times larger concentration (1 wt%). On the right side the respective magnifications are presented.

4.5 The colloid size ratio

As already discussed in detail in Chapter 1.7 the size ratio of the colloids plays a prominent role in determining the structure of binary super-lattices. When particles of different sizes and types are brought together, they must adjust themselves to space constraints in a certain way.

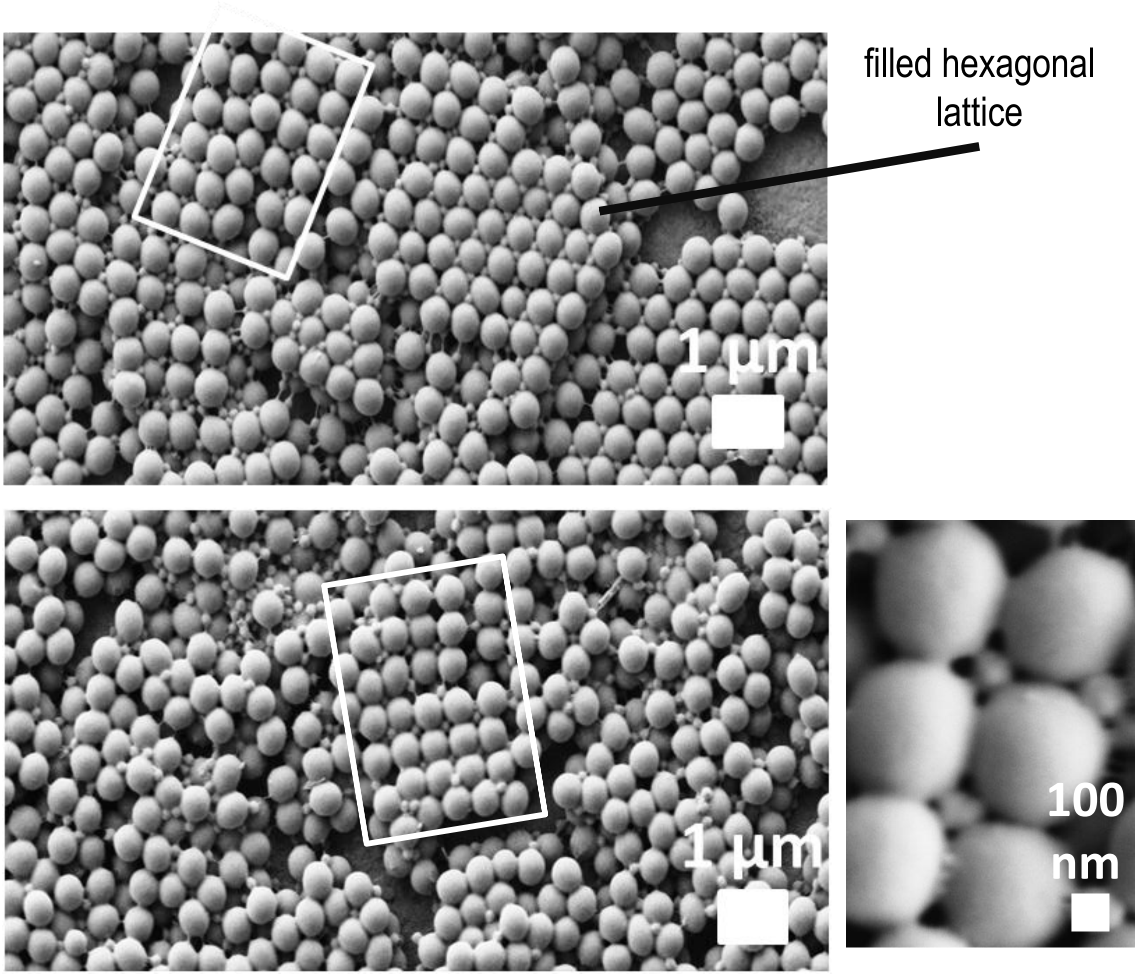

Figure 4.7: Effect of colloid size ratio on the crystal formation. Upper SEM image shows a 1 : 1 mixture of 4VP-1 (R_h = 102 nm) and 4OH-4 (R_h = 260 nm) (→ hexagonal AlB_2 system) and the bottom image shows the binary mixture of 4OH-4 (R_h = 260 nm) with 4VP-2 (R_h = 125 nm) (→ cubic AB system). The cubic systems are highlighted with boxes. The magnified REM is showing the perfectly fitting of the small colloids in the interstitial gaps between the large colloids in a cubic arrangement.

Hence, the colloid 4OH-4 (R_h = 260 nm) in a 1 : 1 mixture with the colloid 4VP-1 (R_h = 102 nm) or alternatively with the colloid 4VP-2 (R_h = 125.1 nm) are considered to be the most promising systems available, where R_h had been determined in the same solvent toluene 70 wt% / chloroform 30 wt% used for the present crystallization experiments. This solvent combination leads to a size ratio of γ = 0.39 in the first and γ = 0.48 in the second case. In the dried state the colloids shrink to give colloid size ratios of 0.25 and 0.39, where the radius now had been determined by REM. The smaller ratio of 0.25 should lead to hexagonal lattices in AlB_2 conformation and the larger ratio of 0.39 should mainly lead to a cubic system analogous to the NaCl configuration. It is clear that the colloid system with the larger size ratio is not able to form binary hexagonal structures in AlB_2. In a hexagonal system the interstitial gaps between the large colloids are too small to host the small 4VP-2 colloids. On the other hand, the system with the smaller colloid size ratio should predominantly form hexagonal structures but it is also able to build cubic arrangements. In the latter case, two or even more smaller 4VP-1 colloids will fill the interstitial gaps.

Figure 4.7 gives some representative examples for a colloid size combination that should lead to a hexagonal lattice (top) and a colloid size combination that should lead to a cubic NaCl binary lattice (bottom). As expected, hexagonal structures occur over large areas from the binary system with colloid size ratio of 0.25. However, the system is also able to form cubic patterns of higher free energy. Simultaneously some cubic arrangements appear with two, three or even four smaller 4VP-1 colloids filling the interstitial gaps (highlighted in the upper SEM image). Further remarkable examples for this fact are presented in Chapter 4.6, Figure 4.8 d and in the Appendix

The colloid combination with a size ratio of 0.39 shows only a few ordered arrays at all. It is much more disordered than the other colloid combination and the ordered patterns are exclusively of cubic nature. One can see that the smaller colloid is perfectly fitting in the interstitial gaps. The NaCl lattice has the highest packing density (0.793 at a size ratio of 0.414) among the binary lattices with AB stoichiometry. The packing density of the NaCl-type lattice exceeds the packing density of fcc close-packed spheres for all size ratios below 0.458. Nevertheless, the overall ordering at all is much worse than the ordering of the other colloid combination that gives the hexagonal AlB_2 patterns. A reason might be that the cubic crystal formation is energetically less favored than the hexagonal crystal formation and thus the hexagonal arrangement is more preferred.

4.6 The colloid number ratio

Like the colloid size ratio and the colloid concentration, the colloid number ratio is considered to be a factor determining the structure of binary assemblies. In the following experiments with the larger 4OH-4 colloids and the smaller 4VP-1 four different colloid number ratios were investigated. It can readily be seen that with increasing amount of small 4VP-1 colloids more interstitial gaps are filled (Figure 4.8 a-d), but additionally to this the overall ordered area decrease drastically. In going from the binary mixture of 2 : 1 small/large (Figure 4.8 b) to 3 : 1 (Figure 4.8 c) the crystal quality gets considerably worse.

Contrary to this a crystallization experiment with a colloidal dispersion of the pure large 4OH-4 particles exhibits large ordered crystal domains of several layer thickness and millimeters in lateral dimensions (see Chapter 1.6, Figure 1.16). Hence, it is obvious that the small colloids distort the system during crystallization. The higher the number of small 4VP-1 colloids gets the less hexagonal AlB_2 phase domains could be found. However, cubic lattice formations with two, three or even four small 4VP-1 colloids in an interstitial gap appear more often then.

Concerning the overall binary crystal quality in terms of space filling in an ordered lattice the system with the colloid number ratio of 2 : 1 small/large seems the most promising option. Towards predominantly cubic ordered systems with two or more small colloids in the interstitial gaps a colloid number ratio higher than 4 : 1 seems to be most suitable. The increase of frequency in cubic domains with increasing amount of small colloids in the binary mixture is proven.

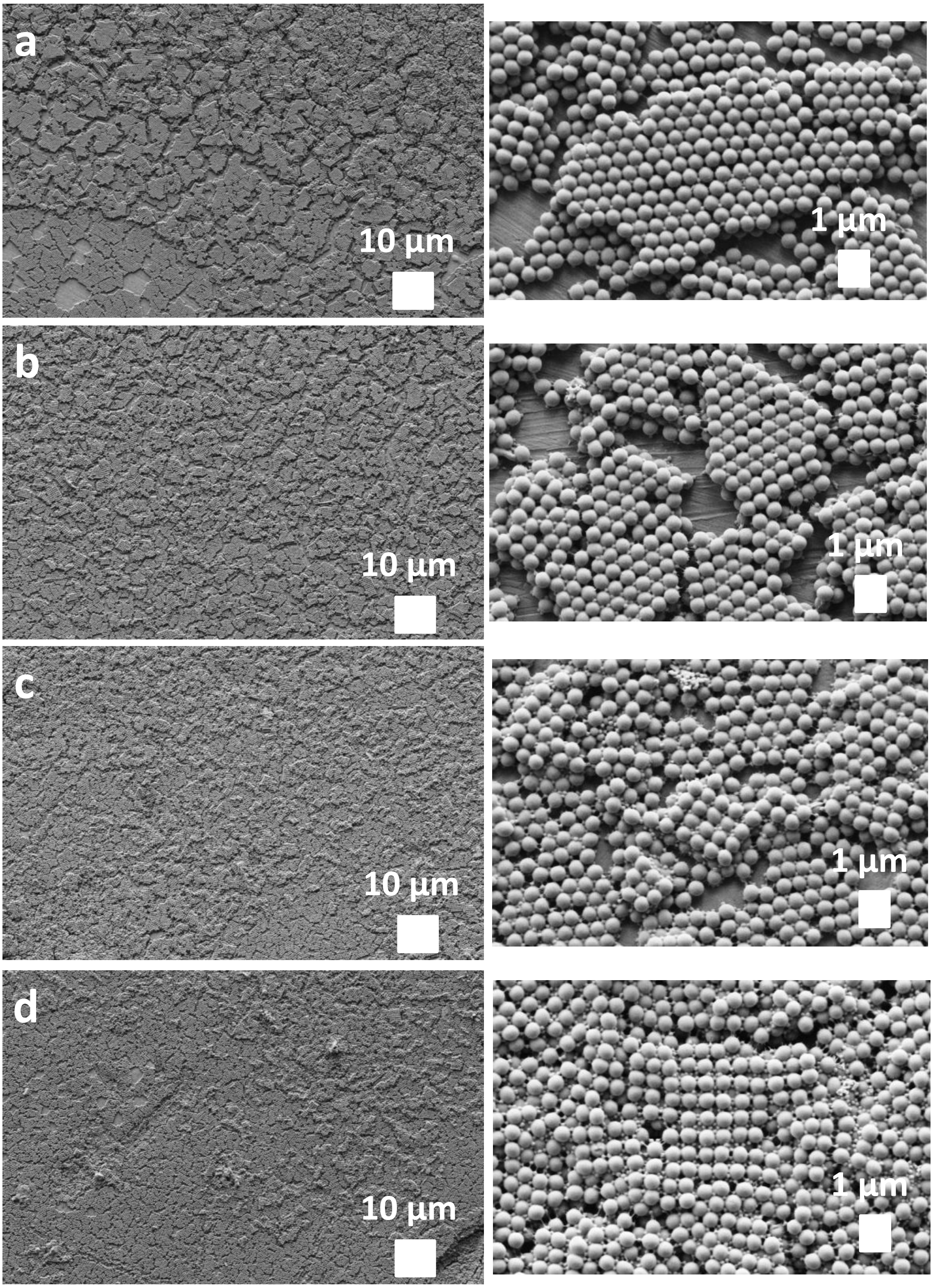

Figure 4.8: Effect of colloid number ratio on the crystal formation of the colloids 4VP-1 (R_h = 102 nm) and 4OH-4 (R_h = 260 nm) → hexagonal AlB_2 system. a) SEM images show a **1 : 1** mixture. b) SEM images show a **2 : 1** mixture. c) SEM images shows a **3 : 1** mixture. d) SEM images show a **4 : 1** mixture The right side images present the corresponding magnifications.

4.7 Conclusion

The present chapter establishes several ways to take influence on the crystal formation. The dependence of crystal formation and crystal structure on various parameters such as colloid size ratio, colloid number ratio, overall colloid concentration and substrate properties was studied by means of scanning electron microscopy. Thereby the crystallization experiments on a polished aluminum SEM stub indicated that polished aluminium stubs are the most useful substrate for our investigations. Using a SEM stub as substrate had remarkable benefits in terms of smoothening and treatment of the surface and convinced us to fix the same geometric conditions for all experiments shown in Chapter 4.3.

Overall concentrations higher than 0.5 wt% lead to a poorer crystal ordering of the colloids. The dried crystal films then have just a few layers of colloids but with a pleasant ordering. The analysis of the crystal formation in dependence of the colloid size ratio induces a switch from a hexagonal system to a cubic system. The size ratio encompassing the hexagonal structure is able to show also a cubic crystal formation when filling the interstitial gaps with more than one small colloid. Contrary to this the colloid system with the larger size ratio prefers the cubic system and does not show any hexagonal appearance. Here the small colloids would be too large to fill the interstitial gaps between the larger colloids. Unfortunately, the overall ordering is worse than in the uniform colloid system which prefers the hexagonal lattice. Ordering in the present binary colloidal system seems to be dominated by the large colloid. While the crystalized large colloids alone show huge crystals with only few defects the disorder increases when adding more and more small colloids. The best colloid number ratio to get ordered domains is between 1 : 1 and 2 : 1 small/large colloids. Here the results were the best and larger-scale binary colloidal crystals with up to three layers with mainly face-centered cubic crystal formation could be generated. Also small cubic crystal formations could be realized if the binary system is furnished with a higher amount of small colloids to fill the interstitial gaps more efficiently.

Further examples for the variation of the overall colloid concentration, the colloid size ratio and the colloid number ratio can be found in the **Appendix** (Chapter 7).

5. Outlook

As has been outlined in Chapter 1, 3D photonic crystals, that can reflect light from any direction or guide photons, potentially offer advances in the next generation micro photonic devices and the integration of existing optoelectronic devices. In the last twenty years, there has been a race in developing new techniques to fabricate 3D photonic crystals structures with large complete PBGs. In recent years, considerable effort has been directed to explore novel materials and technics that will enable mass production of 3D photonic crystal with controlled size, symmetry and defects. While self-assembly approaches are simple and the least expensive, they inevitably will introduce random defects during the assembling process. Thus, control of surface chemistry, composition, and concentration of colloidal particles together with the proper choice of the dispersion medium are critical to the long-range ordering and orientation in colloidal crystals.

In the last decade the focus was on the use of complementary charged colloids to promote binary crystal aggregation. The present thesis shows the possibility of using complementary hydrogen bonds among colloids to support the directed assembly towards binary colloidal crystals. It was shown for the first time that colloids with complementary hydrogen bond patterns are indeed able to hetero-aggregate in the desired manner.

On the way to complex H-bond patterns, like three dentate H-bond motifs known from nature, a single hydrogen bond system occurred to our mind as alternative for controlled crystallization experiments. The single H-bond system with phenol functionalities on one colloid and vinyl pyridine on the complementary colloid is easier to synthesize and is easier to handle then multiple H-bond patterns. The strength of hetero-aggregation can be tuned to some extend by adding suitable capping agents. The switch to multiple hydrogen bond systems as more complex functionalizations is possible as shown in this thesis. But the more complex tridentate triazine functionalized system chosen in this work come along with more difficulties. The triazine moieties can interact via wobble base pairs and thus undergo home-aggregation. For a controlled hetero-crystallization the homo-aggregation among the functionalized colloids must be avoided or suppressed whereas the direct and selective hetero-aggregation must be assured instead. Possible systems for this route may be tetra-dentate ligands with hydrogen bond patterns like AAAD – DDDA. But those functionalities are even more difficult to synthesize and to incorporate on colloid surfaces.

Nevertheless the controlled hetero-aggregation among complementary functionalized components, like the tridentate PMS-Triazin-IV colloids in this thesis on the one side and any tailor-made second colloid component or linear polymer with a complementary functionalization on the other side is possible. This optimistic view is justified by the prospective of tuning the hetero-aggregation and at the same time suppressing home-aggregation with suitable low molecular weight antagonists. Additionally PMS-Triazin-IV colloids can be useful as a carrier for specific molecules. If those molecules are tagged with an antagonistic H-bond motif docking on colloids and controlled release due to changes in the pH-value or an increasing temperature could be possible.

The feasibility of the use of hydrogen bonds to form binary super lattices was demonstrated with the single H-bond system based on phenol functionalities on one colloid and on vinyl pyridine on the complementary colloid. The crystallization experiments outlined in Chapter 4 are very promising but have to be extended. With further different sized colloids the dependence of the colloid size ratio in combination with the colloid number ratio should be analyzed in more detail. This work as others before [40,52,55] point to the fact, that this might be the key to improved binary lattice formation. Another promising idea is to tune the crystallization process with the solvent composition. When starting from a binary colloidal solvent mixture in toluene containing also a strong protonic and volatile solvent component (e.g. methanol) it should be possible to fine tune the hetero-aggregation and thus the lattice formation by means of controlled evaporation. By predominantly evaporation of the H-bond inhibiting solvent the hetero-attractive interaction gets possible and binary crystallization sets in.

Another aspect to be improved is a more quantitative evaluation of the structural features with micrographic images from the crystalized samples. To manifest the respective quality of a certain binary colloidal crystal the support of a proper working image analyzing tool would be helpful. With such a tool certain geometric features, e.g. one small colloid in the interstitial gap of three large colloids, could be defined and its frequency measured to give a measure of the degree of crystallization.

6. Experimental

6.1 Polymer colloids - syntheses

Colloidal crystals are usually assembled from monodisperse polystyrene (PS), poly(methylmethacrylate) (PMMA), and silica particles with sub-micrometer size. [54] This is because particle size variation disrupts the crystalline lattice. Simulation shows that high quality colloidal crystals can be formed if the standard deviation in particle size is within 2%. [56] As the size distribution increases, the intensity reflectance by the stop band decreases rapidly. The PBG in the inverted structures disappears completely when the standard deviation of the particle diameter is larger than ~ 5%.

Polymer microspheres are typically made by heterogeneous radical polymerization. [78-82] Smaller size ranges require modified types of those polymerization processes, like micro-emulsion, emulsion, surfactant free, re-growth, and dispersion polymerization. Different kinds of initiators, surfactants, and co-monomers are used to establish size and charge. Additional functionalities can be introduced during the synthesis of colloidal particles. [80]

In the present work surfactant free emulsion polymerization (SFEP) has been applied as the method to obtain polymer colloids with a narrow spherical size distribution. This method gives access to particles with radii from 75 to 300 nm. [75,82] The difference to the "classical emulsion polymerization" is given by the lack of the surfactant. The aqueous reaction mixture includes the poorly water-soluble monomer and a water-soluble initiator (mostly $K_2S_2O_8$). Polymerization starts by the addition of a sulfate radical to the monomers dissolved in equilibrium in water. (Figure 6.1) The resulting charged oligomers with one sulfate group get insoluble in water with growing chain length. They act as surfactants then and aggregate into micelles. Thereafter the process is analogous to the "classical" emulsion polymerization with further polymerization taking place in the micelles formed during the first step. As the time for initiation and micelle formation is short, but the time during the micelles grow is relatively long, the colloids get very monodisperse in size.

As a result the colloids are ionically stabilized, but with a rather low charge density. This last point is advantageous for the crystallization into polymer opals. The absence of free surfactants prevents the sticking together of dense packed colloids due to migrating surfactants. In combination with the low charge density the colloids behave like hard spheres.

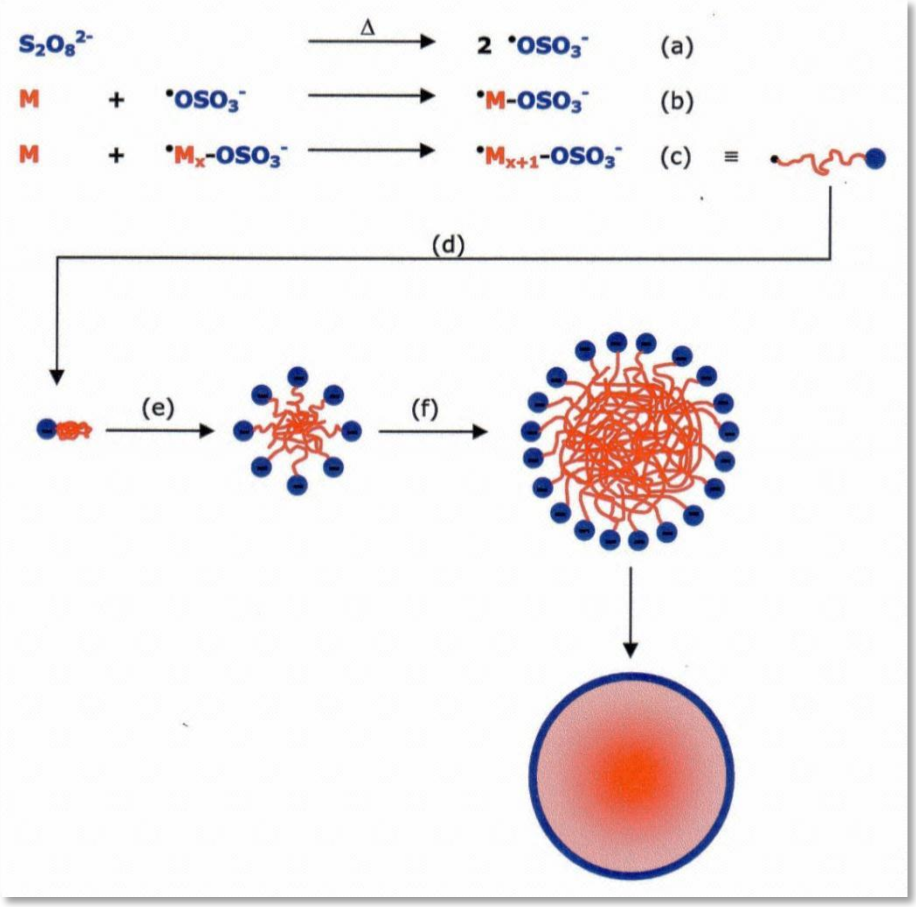

Figure 6.1: Reaction scheme of the surfactant free emulsion polymerization used for the syntheses of highly monodisperse polymeric colloids. a) Radical breakup of the initiator, b) initiation by radical attack of a vinyl monomer, c) chain growth, d) solubility in water decreases with growing length, e) aggregation in micelles, f) incorporation of further monomers in the micelles and polymerization there in leads to the classic emulsion polymerization.

The architecture of the formed particles can be controlled by thermodynamic and kinetic tools. The thermodynamic stability of a polymeric micro-phase system depends on the interfacial energy. The Gibbs free enthalpy of a system with internal interfaces is given by the surface tension of the related components. It is given by:

$$\Delta G = \sum \gamma_{ij} \cdot A_{ij} \qquad (6.1)$$

ΔG = Gibbs free enthalpy

γ_{ij} = Surface tension at the interface of the polymer i and polymer j

A = interfacial energy

On the other side the interface amongst the generated polymers and the interface between the polymers and the surrounding water have to be considered. In a two monomers / two generated polymers (I and II) system the free enthalpy of the entire system is:

$$\Delta G = \sum \gamma_{I-II} \cdot A_{I-II} + \gamma_{I-H2O} \cdot A_{I-H2O} + \gamma_{II-H2O} \cdot A_{II-H2O} \qquad (6.2)$$

The formation of a “core-shell” like colloid with a polymer II rich core and a polymer I rich shell is thermodynamically and kinetically favored if the polymer I is more hydrophilic than polymer II. In our case polymer I consists of vinyl pyridine and polymer II consists of styrene.

Is the used monomer I strongly hydrophilic the formed oligomer radicals I are moving into the already formed tenside micelles of the oligomer radicals II. In those micelles they are growing separated in micro-domains to give a nearly separated shell. Is the concentration of added monomer I not large enough to give a complete shell a so called raspberry structure would be resulting.

6.1.1 Synthesis of 2,4-diaminotriazine DAD hydrogen bond motive functionalized colloids

6.1.1.1 Chemicals

4-vinylbenzyl chloride and boron trichloride (1.0 M in methylene chloride) were purchased from Aldrich, UK. 1,4-divinylbenzene (DVB), sodium hydroxide, potassium hydroxide, potassium peroxodisulfate (KPS), sodium cyanide (NaCN), 1-cyanoguanidine, methanol, carbon tetrachloride, *N*,*N*-dimethylformamide (DMF), 2-propanol, tetrahydrofuran (THF) and uracil were purchased from Merck KGaA, Germany. All chemicals were used as received from the manufacturer without further purification, unless stated otherwise.All monomers were destabilized prior to use via a flush column charged with basic aluminium oxide (Woelm B - Super I from Woelm Pharma, Germany). Doubly distilled water was used for the synthesis and dialysis of the colloids.

6.1.1.2 Synthesis

Deans et al. [83] published the synthesis of linear 2,4-diaminotriazine functionalized random polystyrene copolymer in solution. Their aim was to analyze the chain folding due to intramolecular hydrogen bonding between the triazine moieties followed by an unfolding of those polymeric globules enforced by specific docking of an added antagonist or by changing the solvent polarity respectively. The procedure of Deans et al. is adapted to the preparation of colloids via surfactant free emulsion polymerization (SFEP) of 4-methoxymethyl styrene and divinylbenzene as crosslinker. This method gave access to quite monodisperse particles and avoided surfactants, which may have interfered in further applications. Furthermore, this method enabled us to control the particle size for example by varying the monomer concentration. The 4-methoxymethyl styrene colloids (PMS-M-I) were successively transformed into 2,4-diaminotriazine functionalized colloids. A complete scheme of the synthetic route is shown in Figure 6.2. The complete synthesis was successfully tracked via solid state ^{13}C CP/MAS NMR. The spectra are given in Figure 2.3.

Synthesis of the monomer 4-methoxymethyl styrene (M-2)

The monomer for the SFEP was obtained by a simple methanolysis of 4-chloromethyl styrene (M-1). Although the chloromethyl styrene also constitutes a suitable monomer for further polymer analogue reactions, the detour of polymerizing 4-methoxymethyl styrene was chosen for the following reason: 4-chloromethyl styrene may undergo several side reactions at higher temperatures during the SFEP (e.g., hydrolysis, and hydrogen and/or chlorine abstraction), which then cause an interparticular crosslinking and finally the agglomeration of particles. For the preparation of 4-methoxymethyl styrene 10 ml of 4-chloromethyl styrene were placed into 40 ml of methanol. Precipitated paraffin, which acts as inhibitor was separated by a simple filtration. The mixture was successively added to a solution of 10 g NaOH in 100 ml methanol and refluxed for 6 h with rigorous stirring. Excessive methanol was removed by distillation. 200 ml water was given to this mixture and the aqueous phase extracted successively with diethylether (3 x 100 ml) and n-hexane (2 x 50 ml). The combined extracts were finally washed with saturated aqueous ammonium chloride and with pure water before drying over magnesium sulfate. Solvents were removed to give 8,4 g 4-methoxymethyl styrene and stored after stabilization with 50 mg hydrochinone.

The polymerization - SFEP

A two-necked round bottom flask filled with 47.4 g doubly distilled water was heated to 85 °C and degassed with a gentle stream of argon. 10 mmol (1.48 g) of the synthesized 4-methoxymethyl styrene and 10 mol% (0.13g) destabilized DVB as crosslinker were added to the degassed water via a septum. After the initiation with 1 mol% (29.7 mg) KPS in 1 ml degassed water the polymerization was performed for 5 h at 85 °C. Unreacted monomers were removed by exposing the flask to air for 1 h at 95 °C. After purification by dialysis for five days and successive freeze drying, 1.33 g of the resulting crosslinked 4-methoxymethyl styrene colloids (PMS-M-I) were redispersed in 25 ml CCl_4 while exposing it to ultra-sonic treatment for 30 min.

*Preparation of **PMS-Cl-II** via the methoxymethyl function*

For the rechlorination of the methoxy function on our colloids, the redispersed colloids in CCl_4 were mixed under stirring with 8 ml of 1 M boron trichloride (8 mmol) in CH_2Cl_2 for 2 h at 0 °C and stirred for 2 h more at room temperature. The reaction took place under argon. Unreacted boron trichloride was destroyed by careful addition of 2 ml methanol. The colloids were purified by repeated centrifugation (20 min at 4000 rpm, 3 times) with methanol, followed by resuspension and repeated centrifugation (20 min at 4000 rpm, 3 times) with DMF. The centrifuged colloids were redispersed by ultrasonication in 40 ml DMF.

*Preparation of **PMS-CN-III** via the chloromethyl function*

To insert a cyano function on the colloids the PMS-Cl-II particles were treated with 15 mmol (0.74 g) sodium cyanide in 40 ml DMF. This mixture was stirred at 70 °C for 60 h under argon. The modified colloids were purified by repeated centrifugation (20 min at 4000 rpm, 3 times) with DMF and by resuspension and repeated centrifugation (20 min at 4000 rpm, 3 times) with 2-propanol. The centrifuged 4-cyanomethyl functionalized PMS-CN-III colloids were redispersed in 40 ml 2-propanol for the next step.

*2,4-Diaminotriazine functionalization (**PMS-Triazin-IV**) of PMS-CN-III*

For the last step the colloids PMS-CN-II in 2-propanol were combined with 20 mmol (1.68 g) 1-cyanguanidine and 10 mmol (0.56 g) sodium hydroxide. This mixture was refluxed for 24 h under argon and kept at room temperature for another 24 h under rigorous stirring. The cream-colored colloids were purified by repeated centrifugation (20 min at 4000 rpm, 2 times) with 2-propanol and followed by resuspension in warm water and repeated centrifugation (20 min at 4000 rpm, 3 times) with water. To get the 2,4-diaminotriazine functionalized colloids (*PMS-Triazin-IV*) the aqueous suspension was freeze-dried. The final yield amounts to 1.02 g.

6.1.2 Synthesis of single hydrogen bond motive functionalized colloids

6.1.3 Chemicals

Styrene, 4-methoxy styrene (4MeOS), ethylene glycol dimethacrylate (EGDMA), divinyl benzene (DVB), potassium peroxodisulfate (KPS), trimethylsilyl iodide (TMSI), potassium bromide (KBr), chloroform UVASOL ($CHCl_3$), methanol abs. (MeOH) and tetrachloromethane for IR spectroscopy (CCl_4) were purchased from Merck KGaA, Germany. 4-vinyl pyridine (4VP) was purchased from Alfa Aesar GmbH & Co KG, Germany. All monomers were destabilized prior to use via a flush column using basic aluminum oxide (Woelm B - Super I from Woelm Pharma, Germany). All other chemicals were used as received from the manufacturer, unless stated otherwise.

6.1.3.1 Synthesis

The phenol functionalized crosslinked colloids and 4-vinyl pyridine functionalized crosslinked colloids were synthesized by means of SFEP. This basic method gave access to monodisperse polystyrene based colloids and avoided surfactants, which may have interfered in further applications. Furthermore, this method enabled us to exactly control the particle size for example by varying the monomer concentration.

Pyridine Functionalized Crosslinked Polystyrene Colloid - ***4VP-colloids***

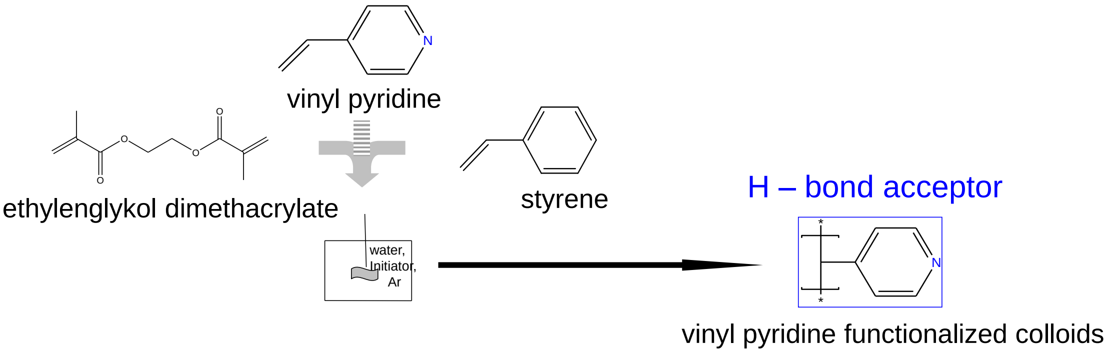

The basic procedure was a SFEP published by Zhang et al. [84] to give monodisperse spherical particles with a core shell like structure in one step. 50 ml of distilled water in a two-necked round bottom flask was heated to 80 °C and degassed with a gentle stream of argon. Styrene and 4VP in a molar ratio of 3 : 1 and 7.5 mol% EGDMA as crosslinker were destabilized before use as described above. After this mixture was added to water under vigorous stirring for 15 min the reaction was started with 1 mol% KPS in a small amount of degassed water. The reaction was stopped after 2 h by fumigating with air for at least 5 min. In order to remove unreacted monomers, the reaction vessel was opened and heated up to 95 °C for 1 h. Inter-crosslinked aggregates of larger size were removed by filtration. Further purification was performed by dialysis over seven days and by repeated centrifugation (30 min at 6000 rpm, 2 times) and resuspension of the particles in distilled water after each cycle. Finally, the aqueous solution was freeze dried to give a fluffy, light and white powder which can be stored.

*Phenol Functionalized Crosslinked Polystyrene Colloids - **4OH-colloids***

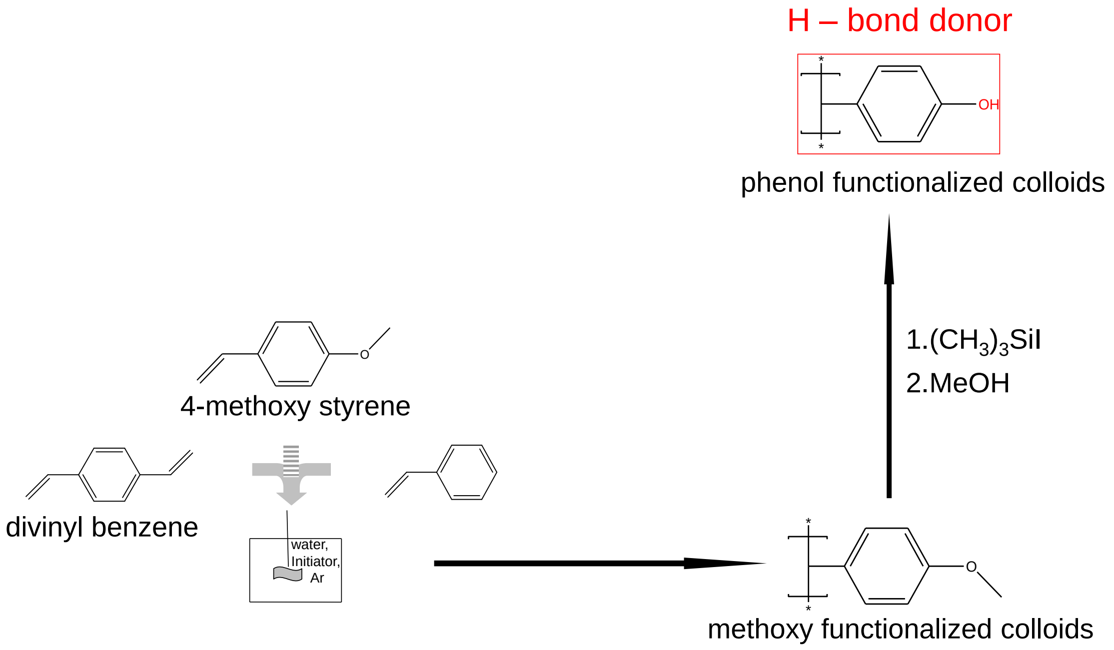

Xiang and Jiang [85] published the synthesis of poly[styrene-co-(4-vinylphenol)] in bulk in order to receive monodisperse spherical crosslinked colloids. This bulk polymerization method was changed into a SFEP. Styrene and 4-MeOS in a molar ratio of 2 : 1 and 7.5 mol% DVB as crosslinker was added to distilled water. Similar to the 4VP-colloid preparation, 1 mol% KPS was added for the initiation. The polymerization was performed at 85 °C for 20 h. Unreacted monomers were removed by opening the flask for 1 h at 95 °C. After purification by centrifugation (30 min at 5000 rpm, 4 times) and successive freeze drying, the colloids were redispersed in 25 ml $CHCl_3$ while exposing it to ultra-sonic treatment. For the quantitative demethylation of the phenolic methoxy function a treatment with TMSI and further methanolysis was applied (second step). [86,87] To this end 1 - 2 ml of TMSI was added under argon to the colloid suspension in $CHCl_3$. The mixture was stirred for 72 h at 40 °C. A violet color indicated the formation of silyl oxonium ions and iodod counterions. The alcoholysis was induced by dropwise addition of MeOH. After further stirring for 1 h the colloids were precipitated with an excess of MeOH. Preliminary purification was reached by gentle centrifugation at 1000 min^{-1}. The centrifugate was redispersed in $CHCl_3$ by means of ultrasonic treatment and successively centrifuged and redispersed four times (15 min at 10000 min^{-1}). The colloids were stored as $CHCl_3$ solutions.

Similar to the 4VP-colloids, the functionalizations in the 4OH-colloids should predominantly occur on the particle surface. This is due to a better solubility of the respective functionalized monomer in the reaction medium water compared to styrene.[83]

6.2 Static and dynamic light scattering

Detailed informations on the method for the analytics of polymeric and colloidal systems by light scattering exists in text books by Chu [88], Brown [89], Berne and Pecora [90] and Schärtl [91].

6.2.1 Static light scattering

Dust particles glitter in sun light because light is scattered by the particles. Its intensity is determined by the particle size and the particle shape. Analogously, light is scattered by molecules and colloids. The incident electromagnetic wave shifts the atomic nuclei and the electrons in opposite directions. This induces an oscillating dipole moment which follows the oscillating electric field with the same frequency and thereby emits electromagnetic radiation itself. The scattering intensity increases with the number of dipoles per molecules, which allows us to determine molecular weights. Scattering is also controlled by the spatial distribution of the dipoles in the scattering particle. This allows determination of the size and shape of molecules or particles.

Depending on the size d of the particle relative to the used wavelength λ_0 of the impinging beam and the difference between the refractive indices of the particle (n_p) and the medium (n_0), three ranges can be distinguished:

- **Rayleigh scattering** : $d < \lambda_0/20$ and $n_p \approx n_0$;
- **Debye scattering** : $d \leq \lambda_0$ and $n_p \approx n_0$;
- **Mie scattering** : $d > \lambda_0$ and $n_p > n_0$ or $n_p < n_0$.

The used colloidal solutions scatter predominantly in the Debye range.

If light is scattered at colloids much larger than $\lambda_0/20$ they must be represented by an ensemble of dipoles or scattering centers respectively. Light waves emitted by these numerous scattering centers and observed at a scattering angle ($\theta > 0$) get out of phase. This interference is measured by the phase shift Δ which is controlled by the scattering angle θ. The destructive interference is zero at $\theta = 0$ but increases with increasing scattering angle (Figure 6.3). Hence, the scattering intensity decreases with the detection angle. The extent of decrease varies with the size and shape of the particles.

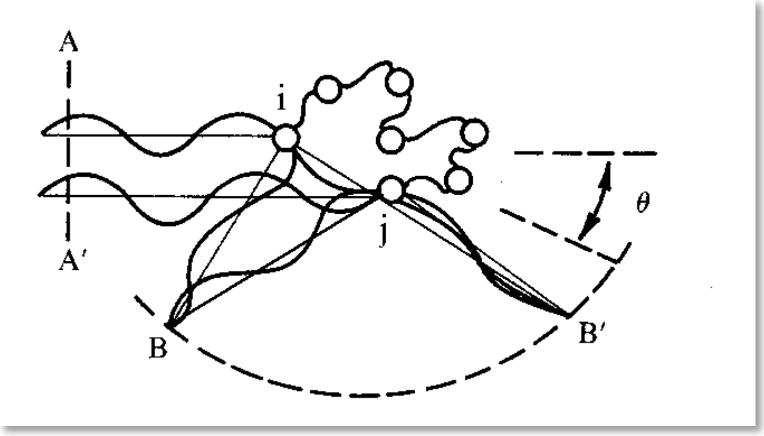

Figure 6.3: Optical retardation in B and B` of two electromagnetic waves scattered at i and j.

To take this effect into account the angular dependence of the normalized scattering intensity from a single particle at infinite dilution is described by a particle scattering factor, *P(q)*.

$$P(q) = \frac{\Delta R_\theta}{\Delta R_{\theta=0}} \qquad (6.3)$$

In equation 6.3 ΔR_θ is the experimental scattering intensity at angle θ and $\Delta R_{\theta=0}$ the scattering intensity at the angle zero. The particle scattering factor is usually not represented as function of θ itself but as a function of the momentum transfer q. The momentum transfer q can easily be related to θ by vector analysis.

$$q = \frac{4\pi \cdot n_{Solvent}}{\lambda_0} \sin\left(\frac{\theta}{2}\right) \qquad (6.4)$$

In equation 6.4 n_{Solvent} is the refractive index of the solvent.

As mentioned before, the particle scattering factor is showing characteristic patterns, which depend on particle shape (Figure 6.4). The scattering function *P(q)* of an isotropic compact sphere with the radius R was derived by RAYLEIGH [86]:

$$P(q) = \frac{9}{(qR)^6}(\sin(qR) - qR\cos(qR))^2 \qquad (6.5)$$

where *R* is the outer radius of the sphere.

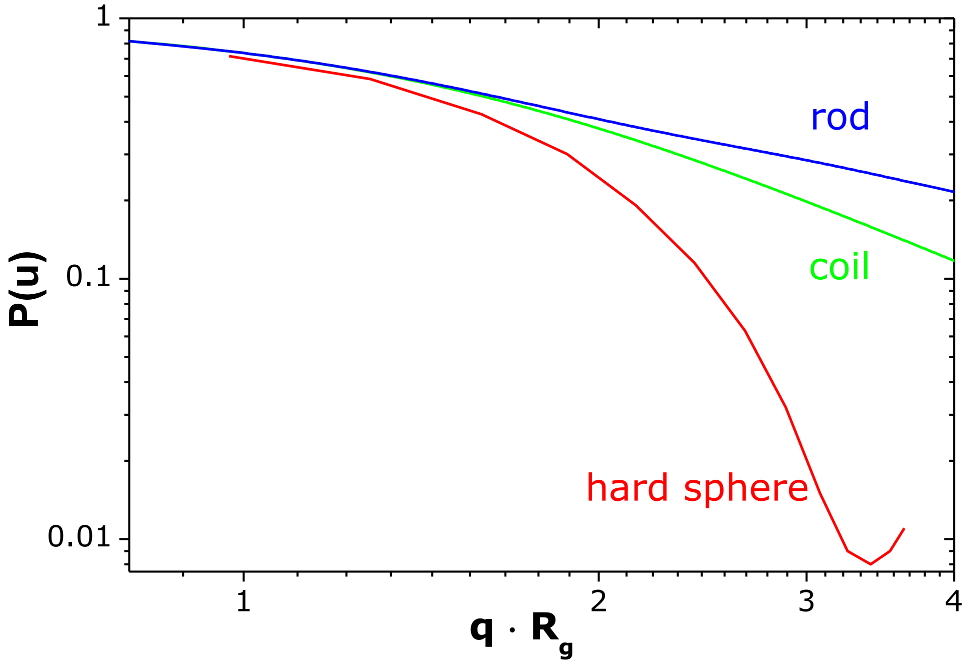

Figure 6.4: Form factors *P(u)* (rod, coil and hard sphere) in the *q*-range accessible by static light scattering as function of *q* normalized with the radius of gyration (= 150 *nm*) ($u = q \cdot R_g$)

For highly dilute solutions one of the most important equation for the data evaluation is the ZIMM equation [92]:

$$\frac{Kc}{\Delta R_\theta} = \frac{1}{M \cdot P(q)} + 2 \cdot A_2 \cdot c \qquad (6.6)$$

with c the concentration of the dissolved colloids in grams per liter, *M* the molecular weight of the colloids, A_2 the second osmotic virial coefficient, with *K* the contrast factor and with ΔR_θ the net scattering intensity, expressed as RAYLEIGH ratio of the colloids. The RAYLEIGH ratio of the colloids contains the experimental scattering intensities.

$$\Delta R_\theta = RR_{\theta,\text{Standard}} \cdot \frac{r(\theta)_{Solution} - r(\theta)_{Solvent}}{r(\theta)_{\text{Standard}}} \tag{6.7}$$

In equation (6.7) $RR_{\theta,\text{Standard}}$ is the RAYLEIGH ratio of a well-known standard. Here toluene is used exclusively ($RR_{\theta,\text{Standard}} = 2{,}7377 \cdot 10^{-5}\ cm^{-1}$ at $\lambda_0 = 532nm$ and $T = 25°\text{C}$). $r(\theta)_x$ is the scattering ratio normalized with the primary beam intensity of the solution, the solvent and the standard respectively.

The optical constant (= contrast factor) K for cylindrical cuvettes according to Hermann and Levinson [93] contains the Avogadro constant, N_A, and the experimental quantities n_{Bath}, which is the refractive index of the used solvent in the goniometer bath, and $\left(\frac{dn}{dc}\right)$, the refractive index increment. This value describes the change of the refractive index of a dissolved material with its concentration in a certain solvent.

$$K = \frac{4\pi^2}{N_A \cdot \lambda_0^4} \cdot \left(n_{Bath} \cdot \frac{\partial n}{\partial c} \right)^2 \tag{6.8}$$

The second osmotic virial coefficient, A_2, originates from a series expansion of the osmotic pressure. It is a measure of the thermodynamic interactions between two molecules, causing systematic deviations from the ideal gas law.

$$\mathrm{A}_2 = \frac{\mathrm{b} - \mathrm{a}/(\mathrm{RT})}{\mathrm{M}^2} \tag{6.9}$$

A_2 can be described with the eigen volume b of the dissolved molecules and the specific interaction parameter a. R is the gas constant.

The form factor in equation (6.3) can be approximated with a truncated series expansion. Terminated after the second term it is:

$$P(q) = \frac{\Delta R_\theta}{\Delta R_{\theta=0}} \cong 1 - \frac{R_g^2}{3} \cdot q^2 \tag{6.10}$$

$R_g^{\ 2}$ is denoted as averaged squared radius of gyration. It is the averaged quadratic distance of all N scattering segments of one molecule from the center of mass of the molecule r_i^2.

$$R_g^2 = \frac{1}{N} \cdot \sum_{i=1}^{N} r_i^2 \qquad (6.11)$$

Combining equation (6.6) and equation (6.10) gives the ZIMM equation for monodisperse systems (with $q \cdot Rg < 1$ and $1/(1-x) \approx 1+x$).

$$\frac{Kc}{\Delta R_\theta} = \frac{1}{M} + \frac{R_g^2 \cdot q^2}{3M} + 2A_2 c \qquad (6.12)$$

Usually polymer or colloid samples are not perfectly monodisperse. From light scattering experiments one obtains then the following averaged values for the molar mass M and the squared radius of gyration.

$$\frac{\Delta R_{\theta=0}}{Kc} = \frac{\frac{1}{K}\sum_{i=1}^{n} \Delta R_i}{\sum_{i=1}^{n} c_i} = \frac{\sum_{i=1}^{n} c_i \cdot M_i}{\sum_{i=1}^{n} c_i}$$

$$= \frac{\sum_{i=1}^{n} m_i \cdot M_i}{\sum_{i=1}^{n} m_i} = \frac{\sum_{i=1}^{n} N_i \cdot M_i^2}{\sum_{i=1}^{n} N_i \cdot M_i} = M_w \qquad (6.13)$$

$$P_z(q) = \frac{\sum_{i=1}^{n} N_i \cdot M_i^2 \cdot P_i(q)}{\sum_{i=1}^{n} N_i \cdot M_i^2} \qquad (6.14)$$

$$\left\langle R_g^2 \right\rangle_z = \frac{\sum_{i=1}^{n} N_i \cdot M_i^2 \cdot \left\langle R_g^2 \right\rangle_i}{\sum_{i=1}^{n} N_i \cdot M_i^2} \qquad (6.15)$$

M_w is the weight averaged molar mass, $P_z(q)$ is the z-averaged form factor and $\langle R_g^2 \rangle_z$ is the z-averaged squared radius of gyration. The square root of the z-averaged squared radius of gyration is typically given as radius of gyration R_g. With the previously made assumption in equation (6.12) one gets:

$$\frac{Kc}{\Delta R_\theta} = \frac{1}{M_w} + \frac{R_g^2 \cdot q^2}{3M_w} + 2A_2 c \qquad . \qquad (6.16)$$

6.2.2 Data evaluation in static light scattering

The scattering signal for static light scattering is averaged over a certain time and measured in dependence of the momentum transfer and the concentration of the sample. With equation (6.16)

- the radius of gyration R_g
- the weight averaged molar mass M_w
- and the second osmotic virial coefficient A_2

can be evaluated by simultaneous extrapolation of the scattering data to $q \rightarrow 0$ and $c \rightarrow 0$ if $\frac{Kc}{\Delta R_\theta}$ is plotted as a function of q^2.

For colloidal particles the use of the GUINIER equation [94] turned out to be most suitable. At very small q values, the dependence of the particle scattering factor $P(q)$ on q can be approximated by:

$$\Delta R_q = \Delta R_{q=0} \cdot e^{-\frac{1}{3}q^2 R_g^2} \qquad (6.17)$$

Regardless of particle shape, a plot of $\ln(\Delta R_q)$ versus q^2 should thus deliver a straight line with the slope of $-\frac{R_g^2}{3}$. The intercept at the y-axis delivers the net scattering intensity ΔR_θ which is directly correlated to the apparent particle mass. The GUINIER evaluation delivers reliable data for the range of $q \cdot R_g < 2$.

6.2.3 Dynamic light scattering

In the previous chapter it was postulated that the frequency of the waves scattered has the same frequency as the primary beam. If a closer look would be possible a frequency broadening instead of a sharp frequency peak would be observed. This broadening is due to the Brownian motion of the particles with respect to the detector and with respect to the primary beam. This effect is in analogy to the DOPPLER shift [95] of acoustic waves.

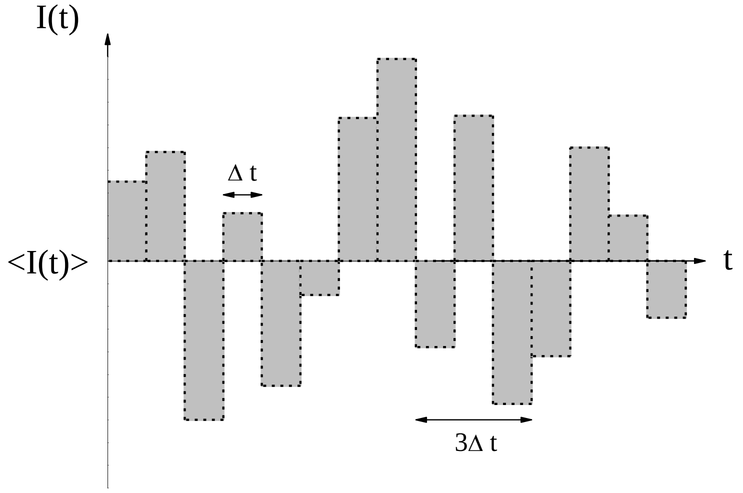

Figure 6.5: Fluctuations in the scattering intensity *I(t)* as function of the time *t*. The width of the interval determines the resolution of the dynamic light scattering experiment.

The velocity of the scattering colloids in solution affects the magnitude of the frequency broadening. Within a certain time range this causes an intensity fluctuation of the scattered light (Figure 6.5).

The dynamic information on particles can be described mathematically by an autocorrelation of the intensity trace recorded during the experiment. A second order intensity-time correlation curve is obtained as follows.

$$g_2(\tau,q)=\frac{\langle I(t)\cdot I(t+\tau)\rangle}{\langle I(t)^2\rangle} \tag{6.18}$$

with an average over *t*.

Here $g_2(\tau,q)$ is the auto correlated intensity at a certain momentum transfer, q. The delay time is defined as $\tau = N \cdot \Delta t$. $I(t)$ is the intensity. At short delay times, the correlation is high. The particles did not have the chance to move to a great extent from their respective initial state. Hence the two signals are essentially unchanged when compared after a very short time interval. When the time delays become longer, the correlation decays. After a long enough time there is no correlation any more between the scattered intensity of the initial and final states. This decay is related to the motion of the colloids and thus the diffusion coefficient of the colloids. The so called SIEGERT equation relates the second order autocorrelation function to the first order autocorrelation function $g_1(\tau, q)$ of the electric field of the scattered light.

$$g_2(\tau, q) = 1 + [g_1(\tau, q)]^2 \tag{6.19}$$

If the sample is purely monodisperse the decay is given by a single exponential.

$$g_1(\tau, q) = e^{-\Gamma \cdot \tau} \tag{6.20}$$

where Γ is the decay rate and derived as follows:

$$\Gamma = D \cdot q^2. \tag{6.21}$$

The decay rate is the inverse averaged time a colloid needs to cover a squared displacement of the order of $1/q^2$. D is the translational diffusion coefficient. It is accessible by fitting the initial slope of the plot $ln(g_1(\tau, q))\ vs.\ \tau$ (see Chapter 6.2.4).

In analogy to the molar mass in static light scattering the diffusion coefficient is apparent and has to be extrapolated to $q = 0$ and $c = 0$.

Usually polymer and colloid samples are not monodisperse. Thus one gets an overlay of a distribution of exponentials correlated to the particle size distribution.

$$\begin{aligned} g_1(\tau, q) &= \sum_i \gamma_i \cdot \exp(-\Gamma_i \cdot \tau) \\ &= \int_0^\infty G(\Gamma) \cdot \exp(-\Gamma \cdot \tau) d\Gamma \end{aligned} \tag{6.22}$$

In the discrete equation γ_i is the weighting factor of the particle size fraction I given by the respective scattering intensity. Within the integral this weighting is retrieved as the function G(Γ). In the case of analyzing polydisperse samples the z-averaged diffusion coefficient is measured.

6.2.4 Data evaluation in dynamic light scattering

The CONTIN analysis developed by PROVENCHER [96] yields the distribution of relaxation times. This is applied to scrutinize the size distribution of a colloid sample. The cumulant analysis introduced by KOPPEL [97] yields the z-averaged translational diffusion coefficient $D_z = \Gamma \cdot q^2$. Here a quadratic cumulant fit according to Eq. (6.23) has been applied.

$$ln(g_1(\tau)) = C + \Gamma \cdot \tau + \frac{\mu_2}{2\Gamma^2} \cdot \tau^2 \qquad (6.23)$$

As mentioned before Γ is the inverse decay time of the correlation function and μ_2 is the second cumulant of the series expansion of the logarithmic field correlation function *(ln* $g_1(\tau)$*)*. An additional measure for the width of the distribution for D_z in a colloid sample can be extracted by means of Eq. (6.24).

$$\frac{\mu_2}{\Gamma^2} = \frac{\langle (D_z - D)^2 \rangle}{D_z^2} \qquad (6.24)$$

$\langle (D_z - D)^2 \rangle$ is the z-averaged squared deviation of the diffusion coefficient D around D_z. The diffusion coefficient can successively be transformed into an effective hydrodynamic radius R_h via the STOKES-EINSTEIN-Equation [98].

$$R_h = \frac{kT}{6\pi\eta} \cdot \frac{1}{D_z} \qquad (6.25)$$

Here k is the Boltzmann constant, T is the absolute temperature and η is the solvent viscosity. The hydrodynamic radius of a certain sample of particles corresponds to a hard, perfect sphere, having the same diffusion characteristics as the sample particles with temperature T and solvent viscosity η given.

Parameters accessible from dynamic light scattering:

- the z-averaged diffusion coefficient D_z and with Eq. (6.25) the hydrodynamic radius
- the distribution of diffusion coefficient of a colloid sample

6.2.5 Combined static and dynamic light scattering

The combination of the radius of gyration scrutinized by static light scattering and the hydrodynamic radius gained by dynamic light scattering retrieves an interesting parameter. Even without knowledge of the complete form factor *P(q)* it is possible to make some predictions concerning the particle shape via the ρ-ratio:

$$\rho = \frac{R_g}{R_h} \tag{6.26}$$

This structure sensitive ratio adopts values of 1.3 - 1.8 [99-103] for polymer coils, depending on the solvent quality and the polydispersity. With an increasing stiffness of the chain segments the value of ρ increases [100,101]. An extreme example for this case is a thin rod. In the case of crosslinked spherical colloids a structure sensitive factor of 0.77 corresponding to the value of a compact sphere is expected.

6.2.6 Comparison of the colloid size distribution functions – Contin vs. Schulz-Zimm and Cumulant vs. var$_{SZ}$

Beside the CONTIN analysis based on the experimental data more information about the polydispersity of colloids in solution can be obtained by a least square fit of a polydisperse scattering curve $\Delta R(q, V_{\mathrm{w}}, k)$ to the SLS data. To this end, V_{w} denotes the weight-averaged volume of the dispersed particles and $\sigma^2 = 1/k$ is the normalized variance of the Schulz-Zimm distribution [104,105]

$$w_{\mathrm{SZ}}(V, V_{\mathrm{w}}, k) = \frac{k^k exp\left(-\frac{kV}{V_{\mathrm{w}}}\right)}{V_{\mathrm{w}}\Gamma(k)}\left(\frac{V}{V_{\mathrm{w}}}\right)^{k-1} \tag{6.27}$$

with the Gamma Function Γ. Equation (6.27) represents a volume fraction weighted distribution of the particle volume V. For SLS data modeling, colloids are considered as compact spheres with radius R and a form factor given by Rayleigh [76] as

$$P_{\mathrm{sphere}}(q,R) = 9\left(\frac{\sin(qR)-qR\cos(qR)}{(qR)^3}\right)^2 \qquad (6.28)$$

If the particle volume is assumed to be proportional to the particle mass, the z-averaged scattering curve can be calculated to be proportional to the particle mass, the z-averaged scattering curve can thus be calculated as

$$\Delta R(q,V_{\mathrm{w}},k) = K\int_0^\infty P_{\mathrm{sphere}}(q,R)w_{\mathrm{SZ}}(V,V_{\mathrm{w}},k)VdV. \qquad (6.29)$$

where the constant K considers the scattering contrast of the particles. The sphere radius is related to the sphere volume according to $R = (3V/(4\pi))^{1/3}$. Modeling of PMS-Triazin-IV scattering data by means of the sphere form factor was not successful. Therefore, the form factor of a dumbbell

$$P_{\mathrm{dumbbell}}(q,R) = \left(\frac{3(\sin(qR)-qR\cos(qR))}{(qR)^3}\right)^2\left(\frac{1}{2}+\frac{\sin(2qR)}{4qR}\right) \qquad (6.30)$$

consisting of two attached spheres with radii R was used instead of P_{sphere} in Eq. (6.29) to model PMS-Triazin-IV scattering data.

A quantity var_{sz} which is comparable to μ_2/Γ^2 (see Eq. (6.24)) can be calculated with the Schulz-Zimm distribution obtained from Eq. (6.29) from SLS as

$$var_{\mathrm{SZ}} = \frac{\langle\frac{1}{R^2}\rangle_{\mathrm{z}}-\langle\frac{1}{R}\rangle_{\mathrm{z}}^2}{\langle\frac{1}{R}\rangle_{\mathrm{z}}^2} \qquad (6.31)$$

whereupon the z-averages $\langle 1/R\rangle_{\mathrm{z}}$ and $\langle 1/R^2\rangle_{\mathrm{z}}$ are calculated analogously to $\Delta R(q,V_{\mathrm{w}},k)$ in Eq. (6.29) by replacing $\Delta R(q=0)\cdot P_{\mathrm{sphere}}(q,R)$ with $1/R$ and $1/R^2$, respectively.

6.2.7 Transferring the CONTIN distribution from the logarithmic space into a linear scale

The ALV-5000 correlator program enables analysis of a correlation function with a cumulant fit and/or a CONTIN analysis. As mentioned before the latter one is based on a Laplace inversion of the correlation function. Since the CONTIN routine works with a distribution of grid points on the logarithmic scale care has to be taken in transferring it to a linear scale.

While the grid points for the evaluation of the decay rate distribution $H^*(\Gamma)$ have an equidistant separation in the logarithmic space their spacing in the linear space diverges exponentially. Large values for Γ correspond to fast decay times τ. The primary result of a fit procedure is represented with $ln(\Gamma_{i+1}) - ln(\Gamma_i) = const.$

The correlation function from the ALV routine is given as distribution of $H^*(\tau_i)$. For every grid point i it is

$$H^*(\Gamma_i) = H^*(\tau_i) \tag{6.32}$$

with

$$\Gamma_i = 1 / \tau_i \tag{6.33}$$

The plot of $H^*(\Gamma_i)$ compared to $H^*(\tau_i)$ in the logarithmic space doesn't change the function values or the distances of the grid pointes but reverses the order of H^* values with

$$\ln(\Gamma_i) = - \ln(\tau_i) \tag{6.34}$$

To plot the distribution $H^*(\Gamma_i)$ in the linear space, $H^*(\Gamma_i)$ has to be "compressed" with increasing Γ_I as follows

$$H(\Gamma_i) = H^*(\Gamma_i) / \Gamma_i \tag{6.35}$$

The abbreviation $H_i^* = H^*(\Gamma_i) = H^*(\tau_i)$ is used in the following. The ALV software is calculating a mean peak position from the plot of $H^*(\tau_i)$ versus τ_i. It is an averaging of $ln(\tau_i)$ and a successive transformation in a decay time according to

$$\bar{\tau} = \exp\left(\frac{\sum H_i^* \cdot \ln(\tau_i)}{\sum H_i *}\right). \qquad (6.36)$$

With Eq. 6.34 it is

$$\bar{\tau} = \exp\left(\frac{\sum H_i * \ln(\tau_i)}{\sum H_i *}\right) \quad = \quad \frac{1}{\bar{\bar{\Gamma}}} = \exp\left(-\frac{\sum H_i * \ln(\Gamma_i)}{\sum H_i *}\right) \qquad (6.37)$$

An alternative and general averaging procedure is used for this work, which reads:

$$<\Gamma> = \frac{\sum H_i \Gamma_i}{\sum H_i} \qquad (6.38)$$

The Eq. 6.38 is based on equidistant increments Γ_{i+1} - Γ_i. Here it is $<\Gamma> \neq <1/\tau>$ and $<\Gamma> \neq \bar{\Gamma}$. The correct averaging for the ALV-5000 correlator with its increasing spacing is given by:

$$<\Gamma> = \frac{\sum H *_i \Gamma_i}{\sum H *_i} = \frac{\sum (H_i \Gamma_i)\Gamma_i}{\sum (H_i \Gamma_i)} \qquad (6.39)$$

with

$$\Gamma_{i+1} - \Gamma_i \propto \Gamma_i$$

The product $H_i \cdot \Gamma_i$ is the weighting factor accounting for the increasing increment width. With Eq. 6.39 the CONTIN distribution is transferred to the linear space and used for the analyses shown in Figure 3.2 of Chapter 3.

6.2.8 Details on light scattering experiments of the colloids bearing the tridentate 2,4-diaminotriazine functionalizations

The 2,4-diaminotriazine functionalized colloids were characterized in water via **combined static** (SLS) and **dynamic light scattering** (DLS) in highly dilute aqueous solutions. Characterization was performed with a model 5000e compact goniometer system (ALV-Laser Vertriebsgesellschaft, Germany), which allows the simultaneous recording of SLS and DLS. A Nd:YAG laser (Soliton, Germany) with 100 mW, operating at a wavelength of 532 nm was used as the light source. Cylindrical quartz glass cuvettes with an outer diameter of 20 mm (Hellma, Germany) served as scattering cells. The instrument scheme is shown in Figure 6.6. A C25 Haake thermostat was used to set the temperature to 25 °C with a precision of 0.01 °C. The scattering intensity was observed under 28 different scattering angles θ in a range of $15° \leq \theta \leq 150°$. This corresponds to a q-regime of $0.0045\ \text{nm}^{-1} \leq q \leq 0.03294\ \text{nm}^{-1}$.

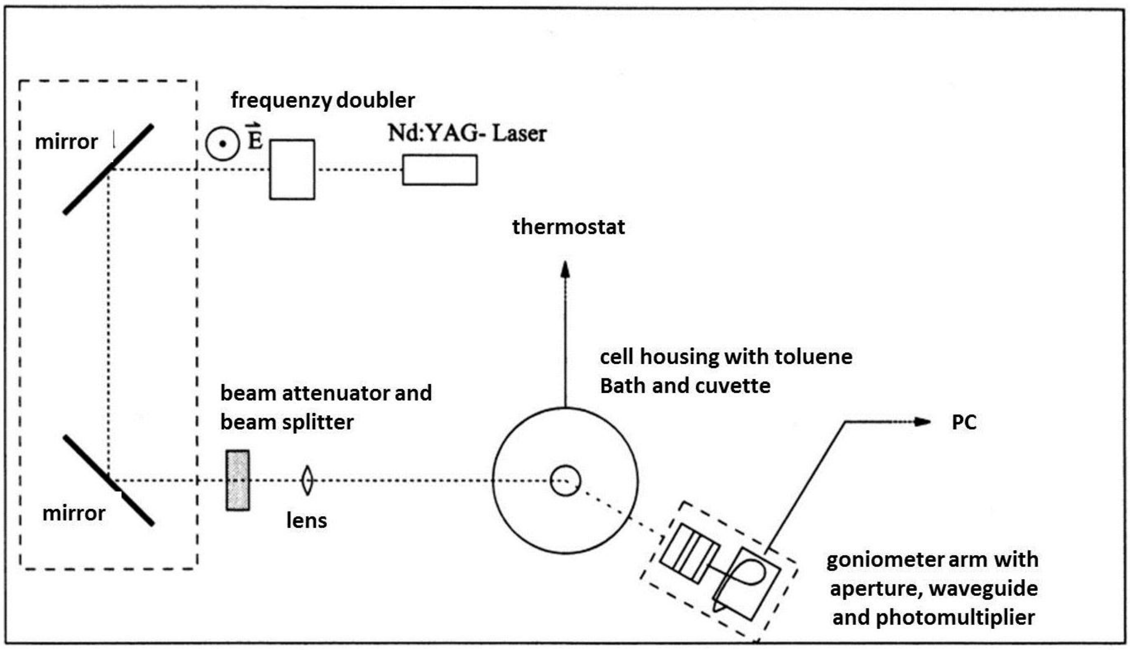

Figure 6.6: Schematic drawing of the used compact goniometer system

The dilute 2,4-diaminotriazine colloid solutions in H_2O were analyzed in steps of 5°. To analyze the static scattering of the colloids in terms of the radius of gyration a Guinier-fit [94] has been applied to the scattering angles of $30° \leq \theta \leq 70°$ ($0.0081\ \text{nm}^{-1} \leq q \leq 0.0181\ \text{nm}^{-1}$). DLS measurements were also evaluated by a linear fit of the apparent diffusion coefficients in a regime of $30° \leq \theta \leq 70°$ to give the D_z at $q = 0$. All samples were filtered with a 1.2 µm PET syringe filter (Macherey-Nagel, Germany) prior to the experiment.

Analysis of the aggregation kinetics of 2,4-diaminotriazine colloids in THF was performed with **time-resolved static light scattering** (TR-SLS). Cylindrical quartz glass cuvettes with an outer diameter of 25 mm (Hellma, Germany) were used as scattering cells. The scattering instrument was a homebuilt goniometer [106] equipped with a He-Ne laser (Coherent, USA) as the light source, operating at a wavelength of 633 nm with 35 mW. It allowed simultaneous recording of static scattering at 2 times 19 fixed angles along both sides of the primary beam covering an angular range of $25.84° \leq \theta \leq 143.13°$ ($0.0064\ \mathrm{nm}^{-1} \leq q \leq 0.02720\ \mathrm{nm}^{-1}$). The minimum time resolution was 2 sec. A C25 Haake thermostat was used to set the temperature to 25 °C.

TR-SLS measurements on aggregation kinetics were performed with triazine colloids in THF and uracil saturated THF respectively. To this end 8 ml THF in the first case and 8 ml THF saturated with uracil (1.33 g/L, 12mM) in the second case were added to the scattering cell by filtering with a 0.2 μm PET syringe filter (Macherey-Nagel, Germany) prior to the experiment. In both cases 50 μl of stock solution with 0.5 g/L colloid content treated with ultrasound was added to the THF or THF/uracil with Eppendorf micropipettes under ultrasonic treatment successively. This leads to a final colloid concentration of 3.2 mg/l. After sonification for 5 min the scattering cell was directly placed into the goniometer and the TR-SLS experiment was started. The removal of the cell from the ultrasonic bath fixed time $t = 0$. One scattering curve was recorded every 30 sec. The duration of a single measurement was 4 sec.

The colloid scattering intensities $\Delta R_{\theta=0}$ at $q = 0$ and the radius of gyration R_g for the aggregation experiments and for the reference experiments were calculated by Guinier fits to the angles $25{,}84° \leq \theta \leq 72.5°$ ($0.0064\ \mathrm{nm}^{-1} \leq q \leq 0.0165\ \mathrm{nm}^{-1}$) for each scattering curve respectively.

6.2.9 *Light scattering experiments with the 4VP- / 4OH-functionalized colloids*

The single colloid components were analyzed by combined SLS and DLS with the ALV 5000e compact goniometer. To establish the radius of gyration a Gunier-fit [94] has been applied to the first four scattering angles of $15° \leq \theta \leq 30°$ ($0.0045\ \mathrm{nm}^{-1} \leq q \leq 0.0088\ \mathrm{nm}^{-1}$). It can easily be verified with model curves that a Gunier analysis in this q-regime gives reliable values for R_g. A monodisperse sphere with $R_g = 250$ nm in this linear fitted q-regime generates an error of 8 % in R_g. DLS measurements were evaluated by a linear fit of the z-averaged diffusion coefficients of all angles ($15° \leq \theta \leq 150°$, $0.0045\ \text{nm}^{-1} \leq q \leq 0.03294\ \text{nm}^{-1}$) to give the D_z at q = 0.

All TR-SLS measurements on aggregation kinetics of mixed 4VP- and 4OH-colloids were performed in highly dilute solutions of 4VP-1 (small colloid) and of 4OH-3 (large colloid) in $CHCl_3$. Addition of both colloid solutions into the scattering cuvettes was performed via filtration with a 1.2 μm PET syringe filter (Macherey-Nagel, Germany) while stirring in the cuvette. Combination of both component solutions fixed time $t = 0$. After careful removal of the stirring bar, the cuvette was inserted in the goniometer and the time dependent measurement was started. If not indicated otherwise, a scattering curve was recorded every 180 sec. The duration of a single measurement was 4 sec.

Aggregation was performed at three volume ratios of the large 4OH-3 colloids to the small 4VP-1 colloids corresponding to 8 : 1, 5 : 1 and 2 : 1 with a fixed concentration of 4OH-3. The combination 5 : 1 under these conditions has had an overall concentration of 50 mg/L. An experiment at the volume ratio 4OH-3 to 4VP-1 of 5 : 1 was performed additionally at a second overall colloid concentration of 25 mg/L. The concentrations of stock solutions were determined gravimetrically by drying a defined solution volume immediately before use. Solutions with well-defined colloid concentrations were then prepared successively from these stock solutions with Eppendorf micropipettes. Number ratios in the final solution were estimated with the known weight concentration of the colloids in the single component solutions and the particle volumes of the respective colloids. Particle volumes became available from their hydrodynamic radii. But to give an example for similar concentrated stock solutions, if a certain colloid has a 10 times larger volume than the small colloid it has to be 10 times in excess to set a number ration of 1 : 1 in the analyzed sample. For each aggregation measurement reference experiments were performed with the two single component solutions. The single component solutions were made from the same stock solutions to have the same final concentrations as they occur in the respective solution of the colloid mixture. The scattering curves of the single components were combined to one scattering curve by simple addition. This linear combination of two scattering curves is expected to be equal only to the curve of the respective mixture prior to aggregation if all interparticular interferences are negligible.

The colloid scattering intensities $\Delta R_{\theta=0}$ at $q = 0$ and the radius of gyration R_g for the reference experiments and for the aggregation experiments were calculated by Guinier fits to the first four angles 25,84 ° ≤ θ ≤ 45.6 ° (0.0064 nm^{-1} ≤ q ≤ 0.0111 nm^{-1}) for each scattering curve respectively. The data from the reference experiments are given in the TR-SLS diagrams as green lines and serve as lower limit to illustrate the initial value at $t = 0$ for each aggregation experiment.

Two additional reference experiments were performed. One experiment analyzed a binary mixture of equally functionalized colloids. To this end small 4OH-colloids (4OH-1) were combined with large 4OH-colloids (4OH-3) in $CHCl_3$ solution at an overall colloid concentration of 50 mg/L. Choice of these two 4OH-colloids was based on their size ratio $R_S/R_L = 0.38$ which was close to the value of $R_S/R_L = 0.52$ belonging to the combination 4VP-1 + 4OH-3 used for the aggregation experiments. The other experiment investigated the hetero-aggregation behavior of mixed 4OH-3 and 4VP-1 colloids in $CHCl_3$ saturated with NaCl in order to compare it with the respective results in salt free $CHCl_3$. The colloid volume ratio was 5 : 1 and the NaCl concentration was 1.2 g/L corresponding to 20 mM.

6.3 IR - Measurements

6.3.1 IR - measurements on the PMS-Triazin-IV colloids

Proof of the successful functionalization of the PMS-Triazin-IV with 2,4-diaminotriazine moieties and of the binding of molecular uracil on the colloids (discussed in Chapter 2) was achieved by FTIR-spectroscopy. We used a Hyperion 2000 IR / NIR microscope coupled with an Equinox 55 IR / NIR device (Bruker, USA). For the analysis of PMS-Triazin-IV colloids a few droplets of a 1 g/l colloid solution in pure THF were placed on a blank metal substrate. After gentle evaporation of the THF and 1 h storage under high vacuum at room temperature the dried colloids were analyzed in reflectance. The occurrence of hydrogen bonds between the 2,4-diaminotriazine functionalized colloids and the antagonist uracil were proven indirectly with samples of PMS-Triazin-IV in THF saturated with uracil (1.33 g/L, 12 mM). To this end a solution of 1 g/l 2,4-diaminotriazine functionalized colloids in the uracil containing THF was sonificated for 10 minutes before storing for 1 h. After repeated centrifugation with pure THF (20 min at 4000 rpm, 2 times) the colloids were redispersed in pure THF via ultrasonic treatment and stored for 1 h. A few drops of the colloid suspension were successively placed on a neat metal substrate. After gentle evaporation of the THF and 1 h storage under high vacuum at room temperature the dry mixture was analyzed in reflectance mode. Due to differences between the thicknesses of the applied colloid films the revealed IR reflection spectra were rescaled to the same height and shifted to better illustrate the corresponding differences. The wavenumber is denoted as λ^{-1} [cm^{-1}].

6.3.2 IR - measurements on the single 4VP- / 4OH-functionalized colloids and their mixtures

Proof of the successful functionalization of colloids with comonomers and of the existence of H-bonds was achieved by FTIR-spectroscopy. We used a Hyperion 2000 IR / NIR microscope coupled with an Equinox 55 IR / NIR device (Bruker, USA). For the analysis of single colloids a droplet of a 2 wt% colloid solution in $CHCl_3$ was placed on a blank metal substrate. After gentle evaporation of the $CHCl_3$ and 1 h storage under high vacuum at room temperature the dry colloids were analyzed in reflectance mode. Existence of hydrogen bonds between complementary functionalized colloids were proven in mixtures of colloid solutions with a number ratio of the colloids of 1 : 1. After washing the formed aggregates 3 times with pure $CHCl_3$ a droplet of aggregate suspension was posed onto a blank metal substrate. The aggregate was measured in reflectance mode after drying the liquids in high vacuum at room temperature for 1 h. Due to differences in the thickness of the applied colloid or aggregate films respectively the revealed IR reflection spectra were shifted to the same height to better illustrate the differences. The wavenumber is denoted as λ^{-1} [cm^{-1}].

6.4 Scanning electron microscopy (SEM)

SEM is one of the most frequently used techniques in characterization of nanomaterials and nanostructures. The resolution of the SEM approaches a few nanometers, and the instruments can operate at magnifications that are easily adjusted from ~ 10 to over

300000. Not only does the SEM produce topographical information as optical microscopes do, it also provides informations of the chemical composition near the surface.

A source of electrons is focused into a beam, with a very fine spot size of ~ 5 nm. Those electrons have an energy ranging from a few hundred eV to 50 KeV that is scanned over the surface of the specimen by deflection coils. As the electrons strike and penetrate the surface, a number of interactions occur that result in the emission of electrons and photons from the sample. SEM images are produced by collecting the emitted electrons on a cathode tube. Various SEM techniques are classified on the basis of what is subsequently detected and imaged. The principle images produced in the SEM are of three types: (i) secondary electron images, (ii) backscattered electron images and (iii) elemental X-ray maps.

(i) When a high-energy primary electron interacts with an atom, it undergoes either inelastic scattering with atomic electrons or elastic scattering with the atomic nuclei. In an inelastic collision with an electron, the primary electron transfers part of its energy to the other electron. When the transferred energy is large enough, the other electron will be emitted from the sample. If the emitted electron has an energy smaller than 50 eV, it is referred to be a secondary electron.

(ii) Backscattered electrons are the high energy electrons that are elastically scattered by nuclei and essentially possess the same energy as the incident or primary electrons. The probability of backscattering increases with the atomic number of' the sample material. Although backscattering images cannot be used for elemental identification, a useful contrast may evolve between regions of the specimen that differ widely in atomic number *Z*.

(iii) An additional electron interaction in the SEM is that the primary electron collides with and ejects a core electron from an atom in the sample. The excited atom will decay to its ground state by emitting either a characteristic X-ray photon or an Auger electron.

All recorded images in the present work are stemming from secondary electrons (i).

SEM not only provides the image of colloids and nanostructured materials, but can also provide detailed information of chemical composition and distribution. The theoretical limit to an instrument's resolution power is determined by the wavelengths of the electron beam used and the numerical aperture of the system. The resolving power, R, of an instrument is defined as:

$$R = \frac{\lambda}{2NA} \quad (6.40)$$

where λ is the wavelength of electrons used and, NA is the numerical aperture, which is engraved on each objective and condenser lens system, and a measure of the electron gathering ability of the objective, or the electron providing ability of the condenser.

6.4.1 The microscope

All SEM pictures for this work were taken with a focused ion beam scanning electron microscope NEON 40 equipped with an EDX (Zeiss, Germany). Each sample was coated with a 3 nm-thick gold film (Bal-Tec SCD 500, UK) to avoid charging effects. The accelerating voltage for the SEM imaging was 2 kV.

6.4.2 SEM experiments on the PMS-Triazin-IV colloids

Microscopy image on the colloids were performed directly on a cleaned aluminum stub as substrate. Sample preparation was performed by placing a few drops of the colloids PMS-M-I and PMS-Triazin-IV, respectively, in THF on a cleaned aluminium stub and by gently evaporating the solvent under ambient (room temperature and -pressure) conditions.

6.4.3 SEM experiments on the 4VP- / 4OH- colloids and their mixtures

Microscopy studies on the single colloid components and hetero-aggregates were performed directly on a cleaned aluminum stub. Sample preparation was performed by placing a drop of $CHCl_3$ solution on the microscope stub and by gently evaporating the solvent. Controlled hetero-aggregation experiments with mixtures of 4VP-colloids and 4OH-colloids in the presence of phenol were done on cleaned glass cover slips as substrates. Here a solution of ~ 0.4 wt% of 4VP-1 and 150 μL of a 5 M phenol solution was combined with a solution of 4OH-3 in $CHCl_3$. The component volumes were designed to generate a number ratio of the two colloids of 1 : 1 in the final mixture. The amount of phenol was just sufficient to keep the binary mixture stable. The solvent was then gently evaporated at room temperature at a reduced pressure of 400 mbar with the substrate being tilted at an angle of ~ 60°. In order to further promote H-bond formation as the one represented in Figure 3.14 phenol was removed at 60 °C and a reduced pressure of 40 mbar for 20 h.

6.4.4 SEM experiments discussed in Chapter 5

The defined conditions are part of the controlled crystallization experiments. Hence, all details on this topic are given in Chapter 4.1 – 4.3.

6.5 Solid State NMR measurements

The entire synthesis of the 2,4-diaminotriazine functionalized colloids (PMS-Triazin-IV) was successfully tracked by solid state ^{13}C-CP/MAS NMR. The spectra are shown in Figure 2.2.

Magic angle spinning (MAS) ^{13}C NMR spectra were recorded at room temperature with a Tecmag Apollo NMR spectrometer at the ^{13}C resonance frequency of 75.47 MHz. The samples were placed in 4 mm zirconia rotors with Kel F caps. A cross polarization (CP) sequence with a 90° pulse of 3.5 ms, a cross-polarization contact time of 2.0 ms and a relaxation delay of 5 s was used. The spectral width was set to 20000 Hz and 8192 scans were accumulated. Spectra at spinning rates of 5 and 8 kHz were recorded in order to identify spinning side bands (SSB). No overlap between center peaks and spinning side bands was observed when the samples were spun at 5 kHz. Therefore, the spectra obtained at 5 kHz are reported and analyzed in this paper. The resonance of the secondary carbon atom in adamantane at 38 ppm was used as a reference for chemical shifts.

6.6 Estimation of the zeta potential

A Zetasizer Nano-ZS (Malvern, USA) was used to determine the zeta potential of our complementary functionalized colloids 4VP-2 and 4OH-3. To this end dilute solutions (100 mg/l) of both types of colloids have been prepared in $CHCl_3$. The zeta potential is related to the electrophoretic mobility of a particle by the Henry equation:

$$U_E = \frac{2\varepsilon z \cdot f(\kappa R)}{3\eta} \tag{6.41}$$

where U_E is the electrophoretic mobility, z is the zeta potential, ε is the dielectric constant of $CHCl_3$, η is the viscosity and $f(\kappa R)$ is Henry's function. κ^{-1} indicates the Debye screening length. R is the outer radius of the particle. For particles in low dielectric constant media like $CHCl_3$ a simplified calculation with the Hückel approximation can be used and $f(\kappa R)$ approaches 1.0. The values of $\varepsilon(CHCl_3) = 4.73$ and $\eta(CHCl_3) = 0.537$ cP have been used as constants in Eq. (6.41).

7. Appendix

Further examples for the variation of the overall concentration, the colloid size ratio and the colloid number ratio.

7.1 Overall concentration

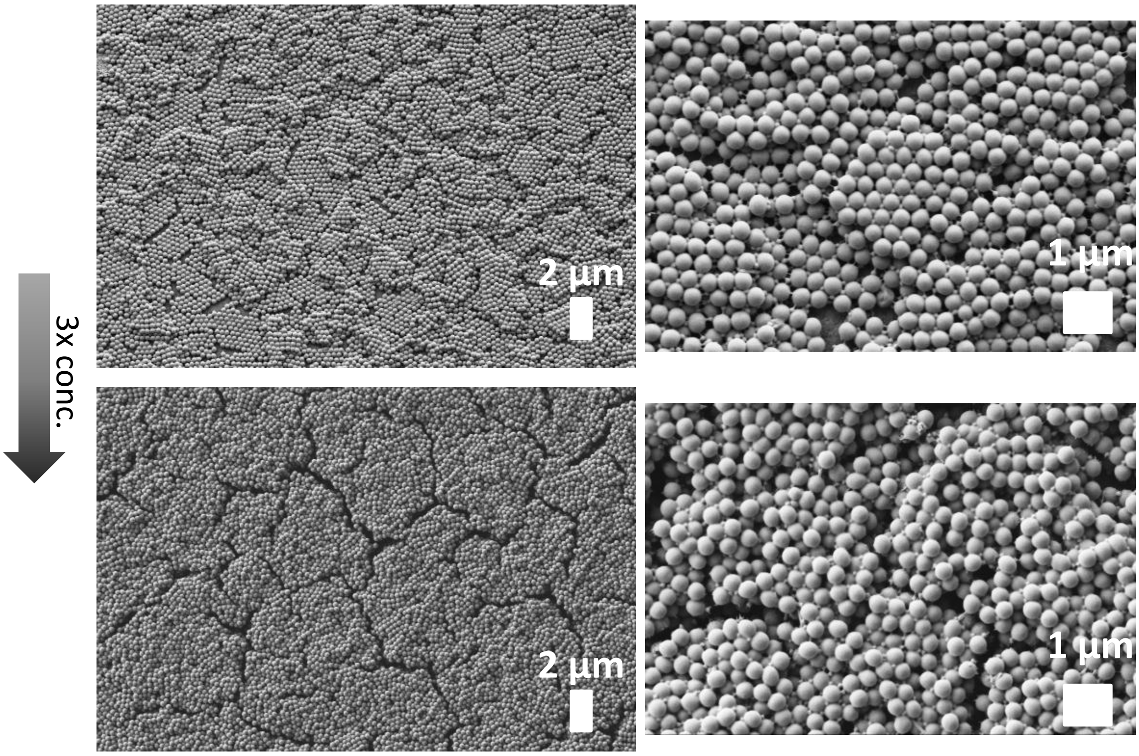

Figure 7.1: Effect of increasing concentration on the crystal formation of the same colloid system. On top (left) a 1 : 1 mixture of 4VP-1 (R_h = 102 nm) and 4OH-4 (R_h = 260 nm) on a polished aluminum stub shows ordered patterns over a broad area. At the bottom the same mixture in a three times larger concentration (1 wt%). On the right side the respective magnifications are presented.

7.2 Colloid size ratio

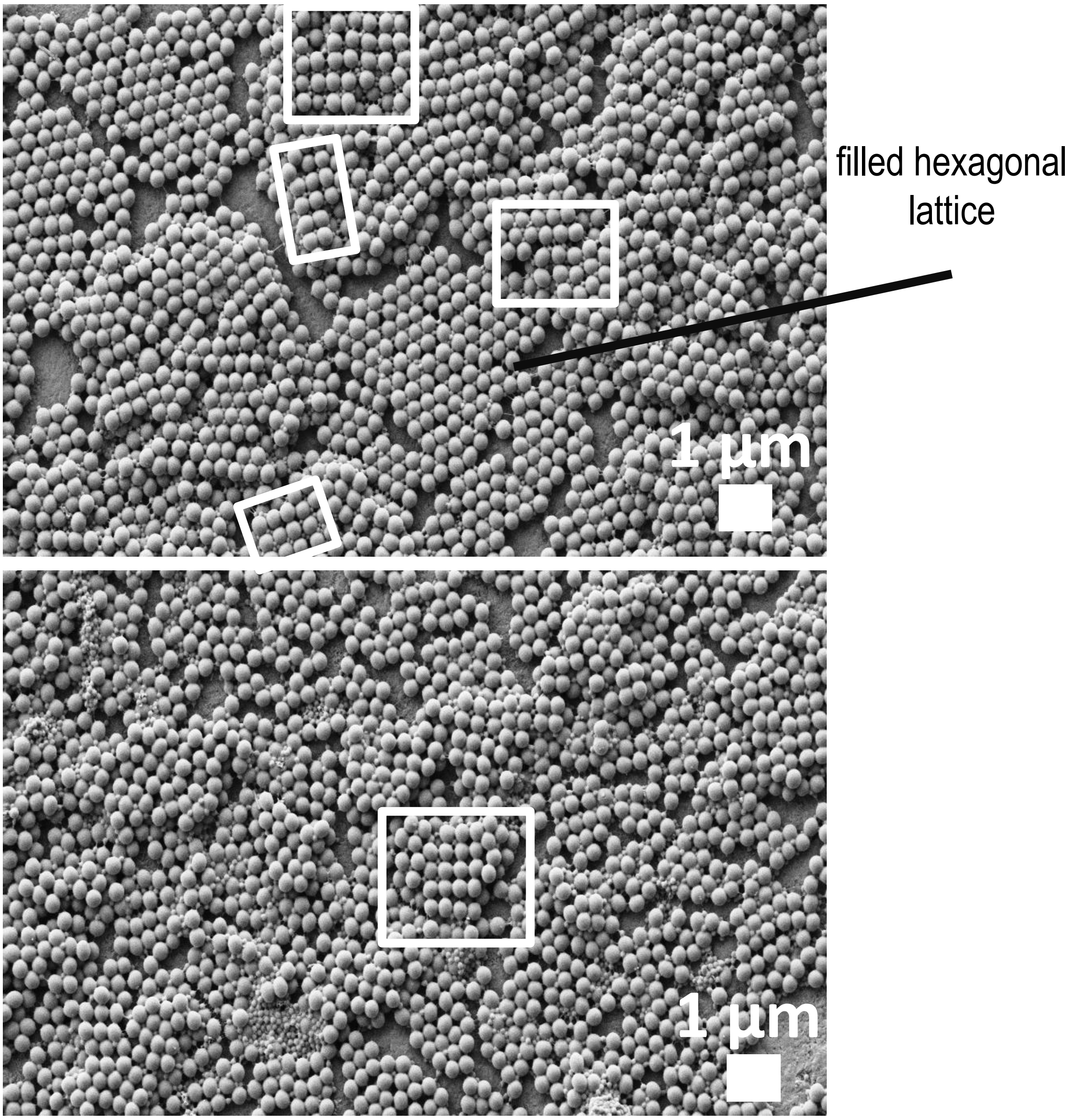

Figure 7.2: Effect of colloid size ratio on the crystal formation. Upper SEM image shows a 1 : 1 mixture of 4VP-1 (R_h = 102 nm) and 4OH-4 (R_h = 260 nm) (→ hexagonal AlB_2 system) and the bottom image shows the binary mixture of 4OH-4 (R_h = 260 nm) with 4VP-2 (R_h = 125 nm) (→ cubic AB system). The cubic systems are highlighted with boxes. Again no filled hexagonal lattice in the bottom image can be found whereas the upper image shows both, filled hexagonal and filled cubic arrangements.

7.3 Colloid number ratio

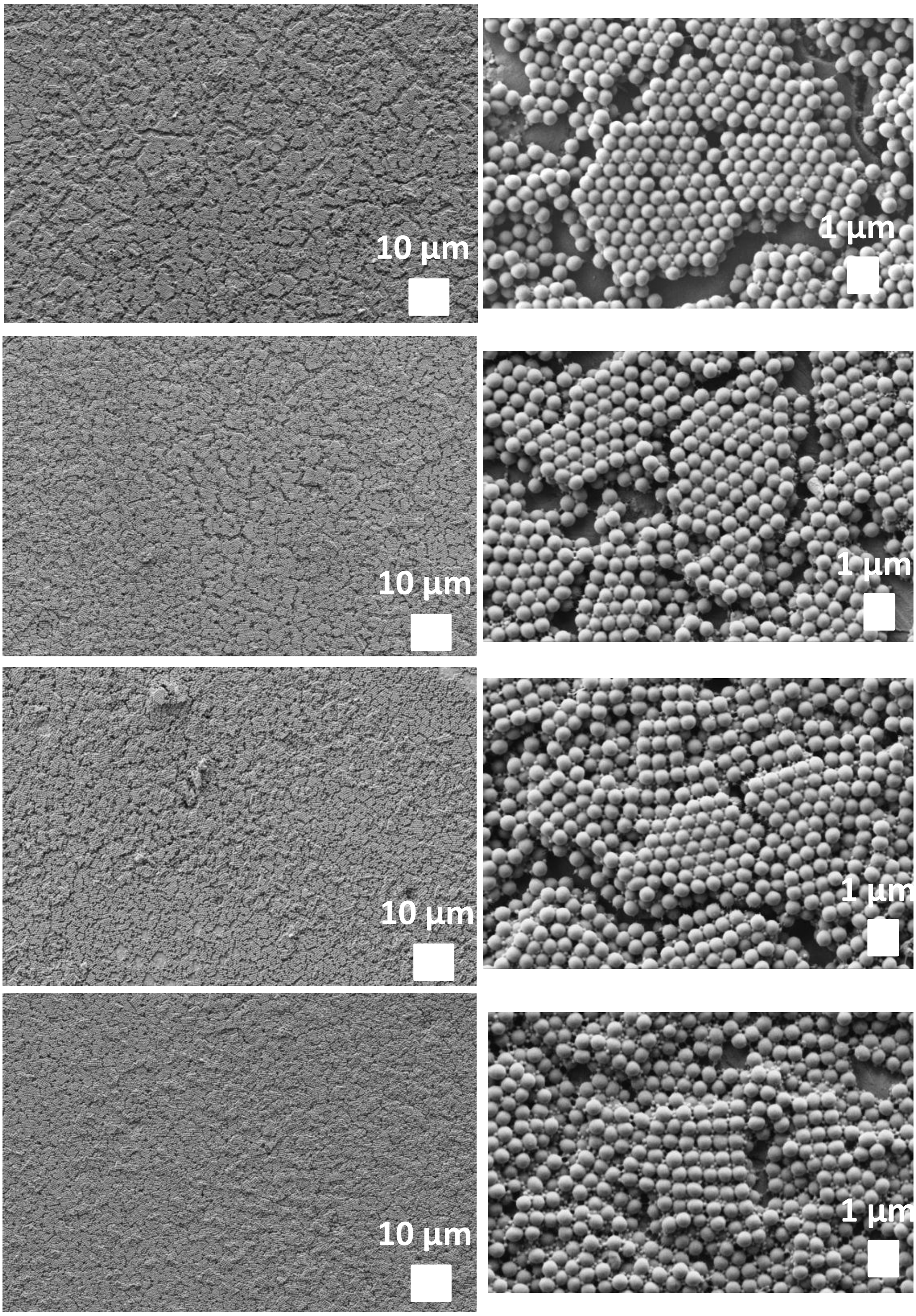

Figure 7.3: Effect of colloid number ratio on the crystal formation of the colloids 4VP-1 (R_h = 102 nm) and 4OH-4 (R_h = 260 nm) → hexagonal AlB_2 system. a) SEM images show a **1 : 1** mixture. b) SEM images show a **2 : 1** mixture. c) SEM images shows a **3 : 1** mixture. d) SEM images show a **4 : 1** mixture The right side images present the corresponding magnifications.

References

1. Mason, C.W. *Structural colors in insects I*, J. Phys. Chem. **1926**, 30, 383
2. Mason, C.W. *Structural colors in insects II*, J. Phys. Chem. **1927**, 31, 321
3. Mason, C.W. *Structural colors in insects III*, " J. Phys. Chem. **1927**, 31, 1856
4. Srinivasarao, M. *Chem. Rev.* **1999**, 99, 1935
5. Prum, R.O. ; Torres, R.H. ; Williamson, S. and Dyck, J. *Nature* **1998**, 396, 28
6. Kaplan, D.L. *Curr. Opin. Solid State Mater. Sci.* **1998**, 3, 232
7. Ghiradella, H. *Appl. Opt.* **1991**, 30, 3492
8. Yablonovitch, E. *Phys. Rev. Lett.* **1987**, 58, 2059
9. John, S. *Phys. Rev. Lett.* **1987**, 58, 2486
10. Lopez, C. *Adv. Mater.* **2003**, 15, 1679
11. Arsenault, A. ; Fournier-Bidoz, S. ; Hatton, B. ; Miguez, H. ; N. Tetreault, Vekris, E. ; Wong, S. ; Yang, S.M. ; Kitaev V. and Ozin, G.A. *J. Mater. Chem.* **2004**, 14,781
12. John S. and Busch K. *J. Lightwave Technol.*, **1999**,17 , 1931
13. Dragoman D. and Dragoman M. *Prog. Quant. Electron.* **1999**, 23,131
14. Sözüer, H.S.; Haus, J.W. and Inguva, R. *Physical Review B* **1992**, 45, 13962
15. Wijnhoven, J. and Vos, W.L. *Science* **1998**, 281, 802
16. Yablonovitch, E.; Gmitter, T.J. and Leung, K.M. *Phys. Rev. Let.* **1991**, 67, 2295
17. Maldovan, M.; Ullal, C.K.; Carter, W.C. and Thomas, E.L. *Nature Materials* **2003**, 2, 664
18. Maldovan, M. and Thomas, E.L. Nature Materials **2004**, 3, 593
19. Thijssen, J.H.J. *PhD Thesis*, Utrecht University, **2007**
20. Joannopoulos, J.D. ; Villeneuve, P.R. and Fan, S.H. *Nature* **1997**, 386, 143
21. Cademartiri, L. *Concepts of Nanochemistry* Wiley-VCH, Weinheim **2009**
22. Temperley, H.N.V. *Proc. Cambridge Phil. Soc.* **1952**, 48, 683
23. Burton, W.K. and Cabrera, N. *Disc. Faraday Soc.* **1949**, 5, 33
24. Lin, S. Y.; Fleming, J. G.; Kurtz, S. R.; Bur, J. *Nature* **1998**, 394, 251

25. Blanco, A.; Chomski, E.; Mondia, S. J. P.; Ozin, G. A.; van Driel, H. M. *Nature* **2000,** 405, 437

26. Stöber, W. ; Fink, A. and Bohn, E. J. *Colloid Interface Sci.* **1968**, 26, 62

27. Guiot, P. and Couvreur P. *Polymeric Nanoparticles and Microspheres* CRC Press, Boca Raton **1986**

28. Kawaguchi, H. *Prog. Polym. Sci.* **2000**, 25, 1171

29. Caruso, F. *Adv. Mater.,* **2001**, 13, 11

30. Ishizu, K. *Prog. Polym. Sci.* **1998**, 23, 1383

31. Hiemenez, P.C. and Rajagopalan *Principles of Colloid and Surface Chemistry* Marcel Dekker, New York **1997**

32. Parfitt, G.D. *Dispersion of Powders in Liquids with special Reference to Pigments* Applied Science, London **1981**

33. Hamaker, H.C. *Physica* **1937**, 4, 1058

34. Overbeek, J.T.G. *J. Colloid Interf. Sci.* **1977**, 58, 408

35. Velasco, E. ; Navascues, G. and Mederos, L. *Phys. Rev. E* **1999**, 60, 3158

36. Urakami, N. and Imai, M. *J. Chem. Phys.* **2003**, 119, 2463

37. Tuinier, R. ; Rieger, J. and de Kruif, C.G. *Adv. Colloid Interf. Sci.***2003**, 103, 1

38. Shah, S.A. et al. *J. Chem. Phys.* **2003**, 118, 3350

39. Roth, R ; Evans, R. and Dietrich, S. *Phys. Rev. E* **2000**, 62, 5360

40. Pusey, P.N. and van Megen, W. *Nature* **1986**, 320, 340

41. Poon, W. *Science* **2004**, 304, 830

42. Kittel, C. and Kroemer, H. *Thermal Physics*, Freeman and Company, New York, **1998**

43. Denkov, N. D.; Velev, O. D.; Kralchevsky, P. A.; Ivanov, I. B.; Yoshimura, H.; Nagayama, K. *Nature* **1993**, *361*, 26

44. Jiang, P.; Bertone, J. F.; Hwang, K. S.; Colvin, V. L. *Chem. Mater.* **1999**, *11*, 2132

45. Braun, P. V.; Zehner, R. W. ; White, C. A. ; Weldon, M. K. ; Kloc, C. ; Patel, S. S.; Wiltzius, P. *Adv. Mater.* **2001**, *13*, 721

46. Prevo, B. G.; Kuncicky, D. M.; Velev, O. D. *Colloid Surf. A* **2007**, *311*, 2

47. Vlasov, Y.A. ; Bo, X.Z. ; Sturm, J.C. and Norris, D.J. *Nature* **2001**, 414, 289

48. Wong, S. ; Kitaev, V. and Ozin, G.A. *J. Am. Chem. Soc.* **2003**, 125, 15589

49. Kitaev, V. and Ozin, GA. *Adv. Mater.* **2003**, 15, 75

50. Cottin, X. ; Monson, P. A. *J. Chem. Phys.* **1995**, *102*, 3355

51. Murray, M. J.; Sanders, J. V. *Philos. Mag. A.* **1980**, *42*, 721

52. Shevchenko, E. V.; Talapin, D. V.; Murray, C. B.; O'Brien, S. *J. Am. Chem. Soc.* **2006**, 128, 3620

53. Hunt, N. ; Jardine, R. ; Bartlett, P. *Phys. Rev. E* **2000**, *62*, 900

54. Saunders, A. E. ; Korgel, B. A. *ChemPhysChem* **2005**, *6*, 61

55. Leunissen, M. E.; Christova, C. G.; Hynninen, A. P.; Royall, C. P.; Campbell, A. I.; Imhof, A.; Dijkstra, M.; van Roij, R.; van Blaaderen, A. *Nature* **2005**, *437*, 235

56. Tam, K. W. ; Li, G. ; Koh, Y. K. ; Yan, Q. ; Wong, C. C. *Langmuir* **2008**, *24*, 9273

57. Mohraz, A., Weeks E. R. and Lewis, *J. A. Phys. Rev. E* **2008**, 77, 060403

58. Elmsley, J. *Chem. Soc. Rev.* **1980**, 9, 91

59. Watson, J.D. and Crick, F.H.C. *Nature* **1953**, 171, 737

60. Mirkin, C. A. ; Letsinger, R. L. ; Mucic, R. C. ; Strorhoff, J. J. *Nature* **1996**, *382*, 607.

61. Alivisatos, A. P. ; Johnsson, K. P. ; Peng, X. ; Wilson, T. E. ; Loweth, C. ; Bruchez, M. ; Schultz, P. *Nature* **1996**, *382*, 609.

62. Geerts, N. ; Eiser, E. *Soft Matter* **2010**, *6*, 4647.

63. Milam, V. T.; Hiddessen, A. L.; Crocker, J. C.; Graves, D. J.; Hammer, D. A. *Langmuir* **2003**, *19*, 10317.

64. Soto, C. M.; Srinivasan, A.; Ratna, B. R. *J. Am. Chem. Soc.* **2002**, *124*, 8508.

65. Rogers P. H. ; Michel E. ; Bauer C. A. ; Vanderet S. ; Hansen D. ; Roberts B. K. ; Calvez A. ; Crews J. B. ; Lau K. O. ; Wood A. ; Pine D. J. ; Schwartz P. V. *Langmuir* **2005**, *21*, 5562.

66. Kim A. J. ; Manoharan V. N. ; Crocker J. C. ; *J. Am. Chem. Soc.* **2005**, *127*, 1592.

67. Jeffrey, G. A. *An Introduction to Hydrogen Bonding*, Oxford University Press, New York, **1997**

68. Thibault, R. J.; Hotchkiss, P. J.; Gray, M. and Rotello V. M. *J. Am. Chem. Soc.* **2003**, 125, 11249

69. Zimmermann, S. C. and Corbin, P. S. *Struct. Bonding* **2000**, 96, 63

70. Whitesides, G. M.; Simanek, E. E.; Mathias, J. P.; Seto, C. T.; Chin, D. N.; Mammen, M. Gordon, D. M. *Acc. Chem. Res.* **1995**, 28, 37

71. MacDonald, C. Whitesides, G. M. *Chem. Rev.* **1994**, 94, 2383

72. Beijer, F. H. Sijbesma, R. P. Vekemans, J. A. J. M. Meijer, E. W. Kooijman, H. Spek, A. L. *J. Org. Chem.* **1996**, 61, 6371
73. Galletto, P. ; Lin, W. ; Mishchenko, M. I. ; Borkovec, M. *J. Chem. Phys.* **2005**, 123, 064709
74. Anderson, D. M. W. ; Duncan, L ; Rosotti, F. J. C. *J. Chem. Soc.* **1961**, 140, 2165
75. Deng, T. S.; Zhang, Q. F.; Zhang, J. Y.; Shen, X.; Zhu, K. T.; Wu, J. L. *J. Colloid Interface Sci.* **2009**, *329*, 292
76. Rayleigh, L. *Proc. R. Soc.* **1914**, A90, 219
77. Mie, G. *Ann. Physik* **1908**, 25, 377
78. Lange, B.; Fleischhaker, F.; Zentel, R. *Macromol. Rapid Commun.* **2007**, *28*, 1291
79. Reese, C. E. ; Guerrero, C. D.; Weissman, J. M.; Lee, K.; Asher, S. A. *J. Colloid Interface Sci.* **2000**, *232*, 76
80. Allard, M.; Sargent, E. H. *Appl. Phys. Lett.* **2004**, *85*, 5887
81. Guiot, P. and Couvreur, P. *Polymeric Nanoparticles and Microspheres* CRC Press, Boca Raton, **1986**
82. Kawaguchi, H. *Prog. Polym. Sci.* **2000**, 25, 1171
83. Deans, R.; Ilhan, F.; Rotello, V.M. *Macromol.* **1999**, 32, 4956
84. Wen, F. ; Zhang, W. *J. Polym. Sci. A: Polym. Chem.*, **2008**, 46, 1192
85. Xiang, M. ; Jiang, M. *Macromol. Rapid. Commun.* **1995**, 16, 477
86. Goodwin, J.W.; Hearn, J.; Ottewill, R.H. *Colloid Polym. Sci.* **1974**, 252, 464
87. Goodwin, J.W.; Ottewill, R.H.; Pelton, R.; Vianello, G.; Yates, D.E. *Brit. Polym. J.* **1978**, 10, 173
88. Chu, B. *Laser Light Scattering Basic Principles and Practice* Academic Press, London **1994**
89. Brown, W. (Hrsg.), *Light Scattering: Principles and Development* Clarendon Press, Oxford **1996**
90. Berne, B. J. ; Pecora, R. *Dynamic Light Scattering with Applications to Chemistry, Biology and Physics* Dover Publications Inc., New York, Reprint **2000**
91. Schärtl, W. *Light Scattering from Polymer Solutions and Nanoparticle Dispersions* Springer-Verlag, Heidelberg **2007**
92. Zimm, B. *J. Chem. Phys.* **1948**, *16*, 1099
93. *ALV 5000 Reference Manual Addition for Static Light Scattering*, Version 1.3 (1994)

94. Guinier, A. ; Fournet, G. *Small Angle Scattering of X-Rays*, Wiley-VCH, New York **1955**

95. Gerthsen, C.; Vogel, H. *Physik*. Springer, Berlin **1999**

96. Provencher, S. W. *Comput. Phys.* **1982**, 27, 213

97. Koppel, D. E. *J. Chem. Phys.* **1972**, 57, 4818

98. Einstein, A. *Ann. Physik Leipzig* **1905**, *17*, 549

99. Burchard, W. ; Schmidt, M. ; Stockmayer, W. H. *Macromolecules* **1980**, *13*, 580 and *Macromolecules* **1980**, *13*, 1265

100. Huber, K. ; Bantle, S. ; Lutz, P. ; Burchard, W. *Macromolecules* **1985**, *18*, 1461

101. Burchard, W.; Frank, M.; Michel, E. *Ber. Bunsenges. Phys. Chem.* **1996**,100, 807

102. Schmidt, M. *Simultaneuos static and dynamic light scattering: application to polymer structure analysis* in *Dynamic Light Scattering: The method and some applications* W. Brown (Hrsg.), Clarendon Press, Oxford **1993**

103. Wu, C. *Colloid Polym. Sci.* **1993**, *271*, 947

104. Aragon, S. R. and Pecora, R. *J. Chem. Phys.* **1976**, 64, 2395

105. Schulz G. V., *Phys. Chem.* **1939**, 43, 25

106. Becker, A.; Schmidt, M. *Macromol. Chem. Macromol. Symp.* **1991,** 50, 249

Scientific Record

- ***Publications***

  - F. M. Bayer, K. Hiltrop and K. Huber: "Hydrogen–Bond–Induced Heteroassembly in Binary Colloidal Systems", *Langmuir* **2010**, 26, 13815.

  - F. M. Bayer, M. Tang, C. Schmidt and K. Huber: "Molecular Recognition with 2,4-Diaminotriazin Functionalized Colloids", *Langmuir, submitted*

- ***Oral Presentations***

  - 1st Convention of the Research Training Group, Schloß Gerden, **2009**
  - 2nd Convention of the Research Training Group, Bad Karlshafen, **2009**
  - 6th Zsigmondy Colloquium, Chemnitz, **2010**

- ***Poster Presentations***

  - Makromolekulares Kolloquium, Freiburg i. Br., **2009**
  - 3rd Convention of the Research Training Group, Paderborn, **2010**

Notes